Nonlinear Frequency Response Analysis of Lithium-Ion Batteries

Von der Fakultät für Maschinenbau
der Technischen Universität Carolo-Wilhelmina zu Braunschweig

zur Erlangung der Würde

einer Doktor-Ingenieurin (Dr.-Ing.)

genehmigte Dissertation

von: Nina Harting
aus (Geburtsort): Peine

eingereicht am: 26.03.2019
mündliche Prüfung am: 18.06.2019

Gutachter: Prof. Dr.-Ing. Ulrike Krewer
Prof. Dr. Uwe Schröder

2019

Acknowledgements

This thesis was conducted in three years and seven months at the Institute of Energy and Process Systems Engineering at the Technische Universität Braunschweig. There are many people I'd like to thank at this point, as they all highly contributed to the completion of this thesis.

First, I want to express my heartfelt thanks to Prof. Dr.-Ing. Ulrike Krewer for giving me the unique opportunity to work in her group along with a great team, for her continuous guidance and support, whether scientific or personal. Further, my gratitude to the doctorate examination committee, the second examiner Prof. Dr. Uwe Schröder and the chairman Prof. Dr. Georg Garnweitner.

My sincere thanks, as well, to my dear InES colleagues, especially Vincent Laue, Oke Schmidt, Marco Heinrich, Lars Bläubaum, Fridolin Röder, Patrick Schön and Theresa Haisch. Furthermore, of course, my heartfelt thanks to Ina Schunke, Elke Drömer and Wilfried Janßen for the administrative and technical support and for brighten up my everyday InES life.

As well, I want to express my gratitude to my parents and my grandma for their unconditional love, lifelong support and for always believing in me. Last but not least my thanks and love to my boyfriend Nicolas Wolff who always pushes me forward and who supported me at every stage of this work.

Many heartfelt thanks to all of you, you made this possible!

Abstract[1]

In this work, an advanced dynamic analysis method, the Nonlinear Frequency Response Analysis (NFRA), is used on Lithium-ion Batteries for the first time. It is demonstrated that NFRA reveals highly relevant nonlinear dynamic information of Lithium-ion Batteries for state diagnosis. The nonlinear information is usually neglected using established electrochemical methods, such as Electrochemical Impedance Spectroscopy, as it is a linear system analysis method.

In the first part, the fundamental applicability of NFRA on Lithium-ion Batteries is established which includes the analysis of the impact of various cell types and designs as well as the impact of measurement conditions and parameters on characteristic nonlinearities. Thereby, NFRA is revealed as highly useful for investigating and distinguishing processes in batteries. It is shown that characteristic frequencies for processes are identified with NFRA, such as solid diffusion, reaction and ionic transport contributions at and in the Solid Electrolyte Interface, even if it is not possible with Impedance Spectroscopy. In the second part of this work, the focus is laid on the impact of aging phenomena on NFRA. Thereby, specific nonlinear characteristics are identified and correlated to aging effects, such as lithium plating. These nonlinear characteristics are differentiated from nonlinear characteristics of cyclic aging at 25°C. Dynamic analysis with Impedance Spectroscopy, however, was not sufficient for this purpose. Finally, different approaches for the evaluation of highly informative data-sets of NFRA in the course of aging are used to estimate the State-of-Health. In the first case study, a degradation model is calculated from the nonlinear frequency responses using Support Vector Regression. Validation data demonstrate the usefulness of NFRA for the data-driven estimation of the State-of-Health. The second case study is based on the correlation of nonlinear frequency responses to the decrease of

[1]Parts of the abstract have been published in [1–4].

cell capacity. Simulations confirm the experimentally identified correlation of NFR data to the assumed capacity fade. Both approaches reveal the applicability of NFRA as an effective, fast and reproducible State-of-Health identification method and as a versatile tool in the aging diagnosis of Lithium-ion Batteries.

Kurzfassung

In dieser Arbeit wird eine fortgeschrittene dynamische Analysemethode, die sogenannte Nichtlineare Frequenzganganalyse (NFRA), zum ersten Mal an Lithium-Ionen-Batterien angewandt. Es wird gezeigt, dass NFRA wichtige, nichtlineare Dynamikinformationen über Lithium-Ionen Batterien beinhaltet. Diese werden bei der Analyse mit etablierten elektrochemischen Messmethoden, wie bei der Elektrochemischen Impedanzspektroskopie, aufgrund der linearen Systemauslenkung nicht analysiert und damit vernachlässigt. Im ersten Teil der Arbeit wird die grundlegende Anwendung von NFRA an Lithium-Ionen Batterien evaluiert und etabliert. Dabei wird der Einfluss von verschiedenen Zelltypen- und designs sowie der Einfluss von Messbedingungen und -parametern auf nichtlineare Charakteristika betrachtet. Es wird gezeigt, dass NFRA zur Identifikation und Trennung von Batterieprozessen geeignet ist. Charakteristische Prozesse in Lithium-Ionen Batterien können mit NFRA auch dann identifiziert und differenziert werden, wie zum Beispiel Festkörperdiffusion, elektrochemische Reaktionen sowie Transportprozesse an und in der Solid Electrolyte Interface, wenn diese Trennung mit Impedanzspektroskopie nicht möglich ist. Im zweiten Teil der Arbeit liegt der Fokus auf der Analyse des Einflusses von Alterungsphänomenen auf NFRA. Dabei werden spezifische, nichtlineare Charakteristika herausgearbeitet und auf typische Alterungsprozesse, wie zum Beispiel Lithium Plating, zurückgeführt. Diese können von den nichtlinearen Charakteristika, die durch die Alterung durch Zyklisierung bei 25°C hervorgerufen werden, getrennt werden. Für diese Degradationsdifferenzierung ist die dynamische Analyse mittels Impedanzspektroskopie nicht ausreichend. Im letzten Teil der Arbeit werden verschiedene Ansätze für die Auswertung und Beurteilung der nichtlinearen Datensätze zur Bestimmung des Gesundheitszustandes von Lithium-Ionen Batterien gezeigt. In der ersten Fallstudie wird ein Degradationsmodell mittels Support Vector Regression berechnet.

Dieses wird mit weiteren Datensätzen validiert, wodurch die Nutzbarkeit von NFRA für die datengetriebene Bestimmung des Gesundheitszustandes gezeigt wird. In der zweiten Fallstudie werden nichtlineare Antwortsignale mit dem Kapazitätsverlust korreliert. Simulationen an einem elektrochemischen Reaktionsmodell bestätigen die Korrelation von NFRA mit dem Kapazitätsabfall. Beide Ansätze demonstrieren den Nutzen von NFRA als effiziente, schnelle und reproduzierbare Methode zur Bestimmung des Gesundheitszustandes und zur Alterungsdiagnose von Lithium-Ionen Batterien.

Publications Within this Thesis

Journal Publications

- N. Harting, N. Wolff, F. Röder, and U. Krewer. Nonlinear Frequency Response Analysis (NFRA) of Lithium-Ion Batteries. Electrochimica Acta, 248:133–139, 2017.
- N. Harting, N. Wolff, and U. Krewer. Identification of Lithium Plating in Lithium-Ion Batteries using Nonlinear Frequency Response Analysis (NFRA). *Electrochimica Acta*, 281:378–385, 2018
- N. Harting, N. Wolff, F. Röder, and U. Krewer. State-of-Health Diagnosis of Lithium-Ion Batteries Using Nonlinear Frequency Response Analysis. Journal of The Electrochemical Society, 166(2):A277–A285, 2019.
- N. Harting, R. Schenkendorf, N. Wolff, and U. Krewer. State-of-Health Identification of Lithium-Ion Batteries Based on Nonlinear Frequency Response Analysis: First Steps with Machine Learning. *Applied Sciences*, 8(5):821, 2018.
- N. Wolff, N. Harting, M. Heinrich, F. Röder, and U. Krewer, Nonlinear Frequency Response Analysis on Lithium-Ion Batteries: A Model-Based Assessment, *Electrochimica Acta*, 260:614–622, 2017.
- N. Wolff, N. Harting, M. Heinrich, and U. Krewer. Nonlinear Frequency Response Analysis on Lithium-Ion Batteries: Process Identification and Differences Between Transient and Steady-State Behavior. *Electrochimica Acta*, 298:788–798, 2019.
- N. Wolff, N. Harting, F. Röder, M. Heinrich, U. Krewer, Understanding Nonlinearity in Electrochemical Systems, *European Physical Journal*, 2019, accepted.

- M. Heinrich, N. Wolff, N. Harting, V. Laue, F. Röder, S. Seitz, U. Krewer, Physico-chemical modeling of a Lithium-ion battery: An ageing study with Electrochemical Impedance Spectroscopy, *Batteries&Supercaps*, 2019, accepted.

Conference Contributions

- N. Harting, N. Wolff, F. Röder, U. Krewer, Nonlinear Frequency Response Analysis on Lithium-Ion-Batteries, Electrochemistry 2016, Goslar, 27.09.2016 (Talk).
- N. Harting, N. Wolff, U. Krewer, Identification and Differentiation of Ageing Processes in Lithium-Ion Batterie using Nonlinear Battery Dynamics, Advanced Battery Power 2018, Münster, 10.-11.04.2018 (Talk).
- N. Harting, U. Krewer, Combination of Dynamic Diagnosis Criteria for a New Estimation of the State of Health (SOH) of Lithium-Ion-Batteries, International Summer School on Metrology 2015 der Physikalisch-Technischen Bundesanstalt, Kloster Drübeck, 24. – 28.08.2015 (Poster).
- N. Harting, N. Wolff, F. Röder, U. Krewer: A Nonlinear Dynamic Approach to Process and Ageing Identification of Lithium-Ion-Batteries, Batterieforum 2017, Berlin, 25. – 27.01.17 (Poster).
- N. Harting, N. Wolff, F. Röder, U. Krewer: Comparisons of Ageing and Temperature Impacts on Nonlinear and Linear Dynamic Responses of Lithium-Ion-Batteries, ECS Meeting 2017, Washington D.C., 4.10.2017 (Poster).
- N. Harting, N. Wolff, R. Schenkendorf, U. Krewer, A Data-Model Approach on Nonlinear Frequency Response Analysis (NFRA) for the Estimation of the State-of-Health of Lithium-Ion Batteries, Batterieforum 2018, Berlin, 24. – 26.01.18 (Poster).

Contents

List of Figures

List of Tables

List of Symbols

Latin Symbols

A	pre-exponential Arrhenius factor, -
A_{geo}	geometric surface area, cm^2
$A_{geo,a}$	geometric surface area anode, cm^2
$A_{geo,c}$	geometric surface area cathode, cm^2
a_l	regression model coefficient
a_s	specific surface area, m^{-1}
$a_{s,a}$	specific anode surface area, m^{-1}
$a_{s,c}$	specific cathode surface area, m^{-1}
b	regression model coefficient, -
C	capacity, Ah
C_0	initial capacity, Ah
C_{DL}	electric double layer capacitance, C m^{-2}
C_i	capacity after i-th cycles
c_e	concentration of the electrolyte, mol l^{-1}
c_{Li}	lithium concentration, mol l^{-1}
c_{Li^+}	lithium-ion concentration, mol l^{-1}
c_{max}	maximal concentration of lithium in the solid phase, mol l^{-1}
$D_{e,eff}$	effective electrolyte diffusion coefficient, m^{-2} s
D_{Li}	diffusion coefficient of lithium, m^{-2} s
d_j	difference between the ranks of two variables, -
E_0	standard potential, V
E_a	activation energy, kJ mol^{-1}
F	Faraday constant, C mol^{-1}

F	support vector regression model, -
f	frequency, Hz
f_1	fundamental frequency, Hz
I	current, A
$\hat{I}$	complex excitation current, A
I_0	current amplitude, A
I_{AC}	sinusoidal excitation current, A
I_{AC1}	sinusoidal excitation current with a higher amplitude, A
I_{AC2}	sinusoidal excitation current with a lower amplitude, A
$I_{AC,EIS}$	sinusoidal excitation current for EIS, A
$I_{AC,NFRA}$	sinusoidal excitation current for NFRA, A
$Im(Z)$	imaginary part of the impedance, Ω
$Im(\hat{Z})$	complex imaginary part of the impedance, Ω
j	complex number, -
j_0	exchange current density, A s
j_{DL}	volumetric current density of the electrochemical double layer, A m^{-3}
j_{Li}	volume rate of lithium-ion generation, A m^{-3}
j_{tot}	total lithium current density, A m^{-3}
K	number of observations, -
k	reaction rate, $m^4 mol^{-1} s^{-1}$
M	number of regression terms, -
n	multiples, -
n_p	data points per decade, -
n_ν	number of oscillations, -
R	gas constant, J mol^{-1} K^{-1}
R	internal resistance , Ω
R_0	initial internal resistance , Ω
$Re(Z)$	real part of the impedance, Ω
$Re(\hat{Z})$	complex real part of the impedance, Ω
R_p	particle radius, m
r	spatial coordinate, m
T	temperature, °C
T_{cell}	cell temperature, °C
$T_{cycling}$	temperature during cycling, °C

$T_{dynamic}$	temperature during dynamc analysis, °C
T_{het}	heterogeneous temperature distribution, °C
T_{homo}	homogeneous temperature distribution, °C
t	time, s
t_p	transference number , -
$\mathcal{T}$	training data set, -
U	voltage, V
$\hat{U}$	complex current amplitude, A
U_0	voltage amplitude, V
U_{AC}	sinusoidal voltage output, V
$U_{cut-off}$	cut-off potential, V
U_{OCV}	open-circuit-voltage, V
$\vec{X}$	input set, -
$\vec{Y}$	output set, -
Y_{2n}	even harmonics, V
Y_{2n+1}	odd harmonics, V
Y_n	n-th harmonic response, V
$Y_{n,min,0}$	initial harmonic response at the intercept with y-axis, V
$Y_{n,min,i}$	initial harmonic response at the intercept with y-axis after i-th cycle, V
Y_{rms}	root mean square of nonlinear frequency responses, V
Z	impedance, Ω
$\hat{Z}$	complex impedance, Ω
$\lvert Z \rvert$	absolute impedance, Ω
$\lvert \hat{Z} \rvert$	absolute complex impedance, Ω
z	number of electrons involved in the electrode reaction, -

Greek Symbols

α	transfer coefficient, -
ΔOCV	difference of open-circuit-voltage, V
$\Delta\phi$	electric potential difference, V
δ_a	anode thickness , μm
δ_c	cathode thickness , μm
ε_a	solid volume fraction anode, -
ε_c	solid volume fraction cathode, -

ε_e	electrolyte volume fraction, -
ε_s	solid volume fraction, -
$\varepsilon_{s,0}$	initial solid volume fraction, -
$\varepsilon_{s,i}$	solid volume fraction after i-th cycles, -
ζ_a	mass fraction active compounds anode, wt%
$\zeta_{add,a}$	mass fraction inactive compounds anode, wt%
$\zeta_{add,c}$	mass fraction inactive compounds anode, wt%
ζ_c	mass fraction active compounds cathode, wt%
η	overpotential , V
Θ	performance efficiency, -
λ	quotient of NFR measured at two excitation currents I_{AC}, -
λ_i	quotient of NFR measured at two excitation amplitudes after i-th cycle, -
$\lambda_{initial}$	initial quotient of NFR measured at two excitation currents I_{AC}, -
ν_i	oscillation i, -
Π_a	calendering degree anode, %
Π_c	calendering degree cathode, %
ρ_s	Spearman rank correlation coefficient, -
σ_{NFR}	standard deviation of NFR, -
τ	time constant, s
Φ	phase shift, °
Π_a	calendering degree anode, %
Π_c	calendering degree cathode, %
ω	angular frequency, Hz
ω_{exp}	experimental frequency range, Hz
ω_{max}	maximum frequency, Hz
ω_{min}	minimum frequency, Hz
ω_{sim}	simulated frequency range , Hz

List of Abbreviations

AC	alternating current
BLB	BatteryLab Factory Braunschweig
CB	carbon black
CC	constant current
CDA	Capacity Differential Analysis
CHB	cyclohexylbenzene
CO_2	carbon dioxide
CV	constant voltage
DC	direct current
DEC	diethyl carbonate
DMC	dimethyl carbonate
DMFCs	Direct Methanol Fuel Cells
DoD	Depth-of-Discharge
DRT	Distribution of Relaxation Times
DVA	Differential Voltage Analysis
EC	ethylene carbonate
EIS	Electrochemical Impedance Spectroscopy
EMC	ethyl methyl carbonate
FFT	Fast Fourier Transformation
ICA	Incremental Capacity Analysis
LCO	lithium cobalt oxide
Li	lithium
$Li_{1-x}MO_2$	lithiated transition metal oxide
Li_2O	lithium oxide
Li_2CO_3	lithium carbonate

LiOH	lithium hydroxide
$LiMO_2$	lithium transition metal oxide
$LiPF_6$	lithium hexafluorophosphate
Li_xC_6	lithium intercalated graphite
LFP	lithium iron phosphate oxide
LIBs	Lithium-ion Batteries
LCO	lithium cobalt oxide
LMO	lithium manganese oxide
LTO	lithium titanium oxide
NCA	nickel cobalt aluminum oxide
NFR	nonlinear frequency responses
NFRA	Nonlinear Frequency Response Analysis
NMC	nickel manganese cobalt oxide
NMR	Nuclear Magnetic Resonance
OCV	Open-Circuit-Voltage
PVDF	polyvinylidene fluoride
SEI	Solid Electrolyte Interface
SEM	Scanning Electron Microscopy
SoC	State-of-Charge
SoH	State-of-Health
SoH_i	State-of-Health after i-th cycle
$SoH_{NFRA,i}$	State-of-Health after i-th cycle calculated with NFRA
SVR	Support Vector Regression
SWOT	strengths, weaknesses, opportunities, threats
TEM	Transmission Electron Microscopy
THD	Total Harmonic Distortion
VC	vinyl chloride

Chapter 1

Introduction

1.1. Motivation[1]

Society, economy as well as politics are facing one of the greatest global challenges of the 21^{st} century, namely, the transition from fossil fuel based mobility to electrified, respectively hybrid-electrified mobility. Currently, Lithium-ion Batteries (LIBs) with their comparably high energy and power density are the state-of-the-art technology to fulfill this goal. However, the high demands on the LIB technology regarding performance and energy density for a broad and increasing application for electric vehicles have to be satisfied and maintained. Strategies to fulfill this goal are the identification of new, superior battery technologies, the so called next generation batteries as well as the optimization of the current lithium-ion based technology. In Figure 1.1, the progression of the specific energy and the energy density on cell level with the advancement of the battery technology from the outdated lead-acid cells over the state-of-the-art LIBs to the highly promising, future solid-state cells is shown. Independent of the battery technology and its chemistry, reliable, accurate and in-depth diagnosis as well characterization of battery cell processes and degradation in the entire cycle life are mandatory.

Within this thesis, Nonlinear Frequency Response Analysis (NFRA) is applied on LIBs to get an advanced and more detailed insight in the dynamic behaviour of LIBs. With NFRA, dynamic analysis is extended to consider nonlinearities, as well. This may offer the opportunity of enhanced process characterization and separation, compared to state-of-the-art linear system analysis techniques, e.g. Electrochemical Impedance Spectroscopy (EIS). In EIS, nonlinearities are not wanted as they distort the reliability of EIS. Due to the mentioned reasons, the application of NFRA regarding aging diag-

[1] Parts of this section have been published in [1].

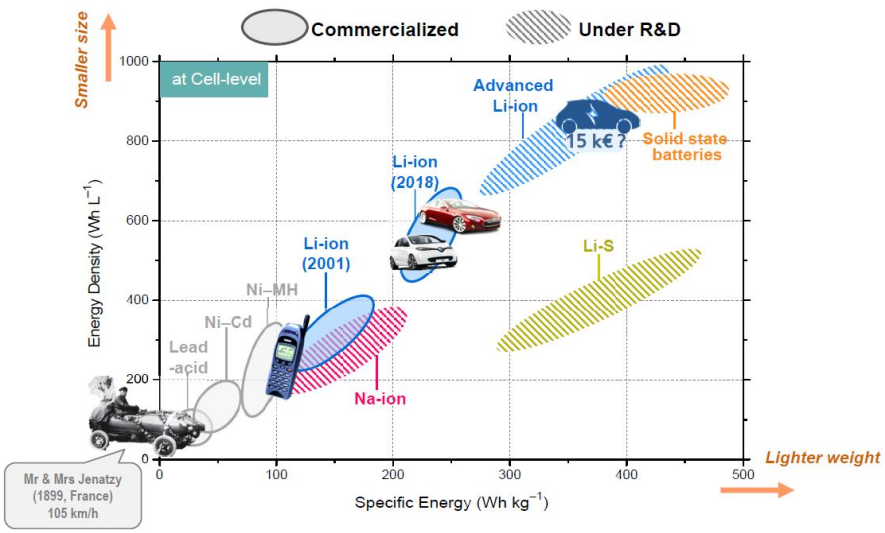

Figure 1.1.: The progression of the specific energy and the energy density on cell level with the advancement of the battery technology towards solid-state batteries [5].

nosis and State-of-Health (SoH) estimation may be promising and is analysed within this work, as well. Thereby, this thesis may be of high interest for the improvement of the current LIB technology as well as for the development of future battery technologies, as the methodology of NFRA is easily applicable on every electrochemical system.

1.2. Fundamentals of Lithium-Ion Batteries

Currently, LIBs are the state-of-the-art battery technology for hybrid electric vehicles and electric vehicles. LIBs contain two spatially separated electrodes which consist of the electrochemically active material and electrochemically inactive components, such as conducting additives and binder, respectively attached to a current collector. Typically, the positive electrode is referred to as the cathode and the negative electrode is referred to as the anode. This terminology results from the field of primary cells and therefore has a historical background. The electrolyte of LIBs consists of a conducting salt and a solvent, respectively solvent mixture which influence the cell performance. As electrolyte, carbonate-based solvents usually are used [8]. To prevent short-circuiting, a lithium-ion permeable separator is placed between the electrodes. The electric current is generated due to ionic transport through the separator which itself is electrically insulating. In Figure 1.2, the working principle of the discharge and the charge process of a LIB is illustrated. The operation is based on the inter-/deintercalation of lithium-ions in the anode, respectively cathode which function as insertion hosts [9]. During the charging process, lithium-ions deintercalate from the cathode; the cathode is thereby oxidized. Lithium-ions are transported via diffusion and migration through the electrolyte to the anode. At the anode, lithium-ions intercalate in the host structure of the anode; the anode is thereby reduced. In dependence of the lithium-ion concentration, a potential difference in the LIB is generated. For the discharge process, these processes are vice versa. In this case, the driving force is the potential difference, generated in the cell during the charging process. The chemical equations of the charging, respectively discharging process are given in the following equations for the negative electrode and the positive electrode in which M corresponds to the transition metal, respectively transition metal mix, used in the oxide.

$$\mathrm{Li_xC_6} \rightleftharpoons \mathrm{xLi^+ + xe^- + C_6} \tag{1.1}$$

$$\mathrm{Li_{1-x}MO_2 + xLi^+ + xe^- \rightleftharpoons LiMO_2} \tag{1.2}$$

LIBs with different electrode materials in dependence of the application are commercially applied, each with characteristic advantages and disadvantages [11, 12]. Generally, the higher the energy density of the battery cell, the higher is the electric range of electric and hybrid electric vehicles. Therefore, the energy density of

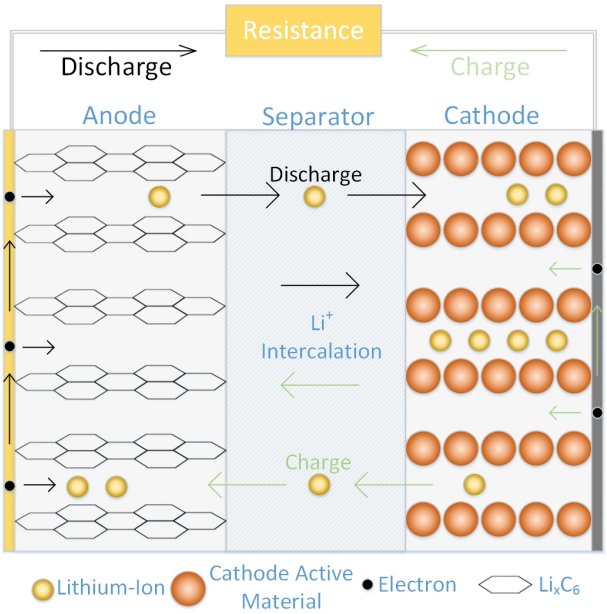

Figure 1.2.: Working principle of the discharge and charge process of LIBs [10].

batteries has to be increased to extend the electric range. In the following, the most prominent electrode materials and its theoretical specific capacities are given [12, 13]. The practical specific capacity is lower in dependence of the used cell potential range and the operation current.

The first commercially used cathode materials in LIBs were lithium manganese oxide spinel (LMO; 148 mAh/g) and lithium cobalt oxide (LCO; 274 mAh/g). In recent years, cathodes consisting of a transition metal oxide mix, namely lithium nickel manganese cobalt oxide (NMC; 280 mAh/g) in different ratios (1:1:1, 6:2:2, 8:1:1) gained popularity due to higher cycle life times and its high energy density. Battery cell development is moving to NMC cathodes with a higher nickel proportion as this increases the practical energy densitiy even more. A great disadvantage of NMC, however, are the high costs due to limited cobalt resources. Further, LIBs with cathodes consisting of lithium nickel cobalt aluminum oxide (NCA; 279 mAh/g) are used for some applications, as NCA has a comparably high practical specific capacity of 199 mAh/g [12]. However, it is not as thermally stable as other cathode materials. A detailed overview of cathode material properties is given in [11, 12]. The state-of-the-art used anode material in LIBs are carbon-based [14]. Graphite (372 mAh/g) has been commercialized as state-of-the-art anode material twenty years ago and is the most common used material due to its noticeable advantages, such as low costs, good electrochemical and mechanical stability as well as availability. The anode material lithium titanium oxide (LTO; 175 mAh/g) is commercialized, as well, especially for high power applications

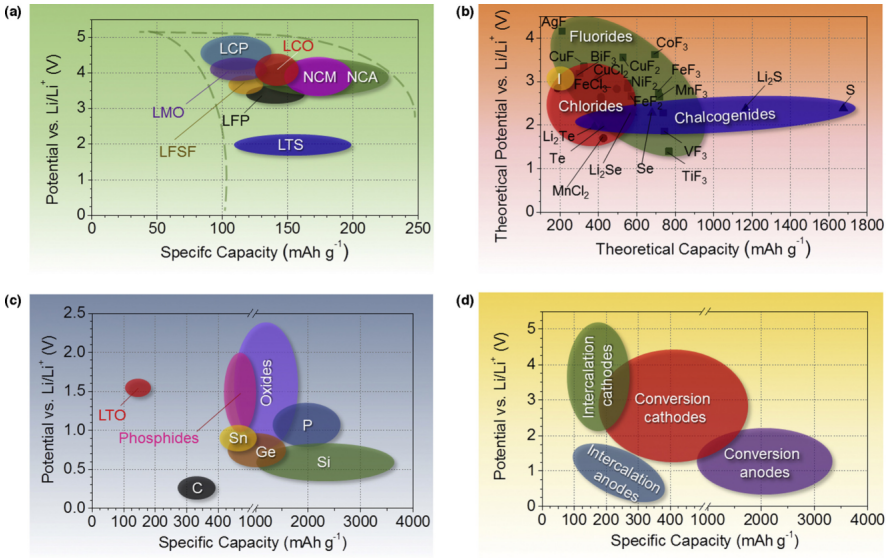

Figure 1.3.: Comparison of potential and theoretical capacity for intercalation cathodes (a), conversion cathodes (b), anodes (c) as well as an overview of material properties of all types of electrodes (d) [12].

[15] and used in combination with lithium iron phosphate (LFP; 165 mAh/g) as high power cathode material [16]. In the overview of specific anode and cathode materials in Figure 1.3, promising future battery technologies are illustrated which are still under research and not yet commercialized. Silicon-alloys as anode and nickel rich NMC as cathode are suggested to be state-of-the-art in 2030 [11].

1.3. Aging Processes of Lithium-Ion Batteries

In this section, characteristic aging processes of LIBs are described. Parts of this section have already been published in [1–3]. Manifold effects impact the degradation and cycle-life of LIBs. Following a cause-and-effect principle, the main factors influencing battery degradation and their interactions are summarized in an Ishikawa diagram shown in Figure 1.4. The cell design, operating as well as environmental conditions affect the cell aging and therefore the lifespan of LIBs [17]. Various degradation processes can be distinguished which may lead to a decrease of the maximal usable capacity and to an increase of the internal resistance of the cell [14, 17, 18]. Aging processes occurring at the negative and the positive electrode differ and are therefore usually differentiated in the literature [17]. Aging processes of the electrolyte, as well as the separator, mostly result from reactions with the electrodes, respectively reactions at the electrode-electrolyte interface [17]. Further, calendar and cyclic ag-

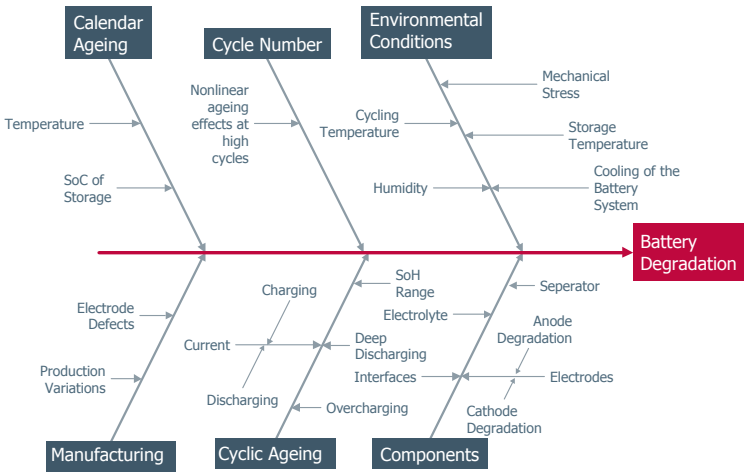

Figure 1.4.: Ishikawa diagram of the various aging impacts that are leading to battery degradation [3].

ing can be distinguished which both depend on environmental conditions [18, 19]. Additionally, the State-of-Charge (SoC) at which the battery is stored influences the calendar aging [20]. Regarding cyclic aging, the Depth-of-Discharge impacts battery degradation processes, as well [21]. Moreover, manufacturing aspects, i.e. the electrode materials and the production process, complete the picture of relevant aging factors.

In Figure 1.5, the main aging effects occurring at a graphene anode are illustrated [17]. The most prominent aging process at the anode is the formation of the Solid

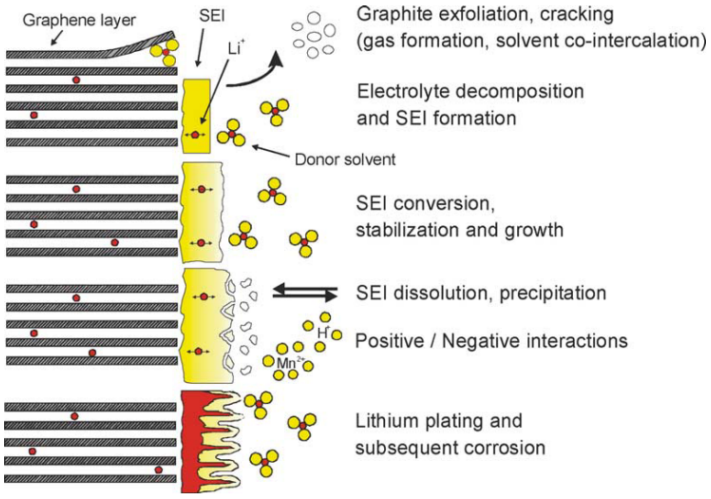

Figure 1.5.: Overview of the main aging factors at graphene anodes according to Vetter et al. [17].

Electrolyte Interface (SEI) due to the reduction of the electrolyte at the electrode-electrolyte interface during initial cycling and its growth, respectively conversion of

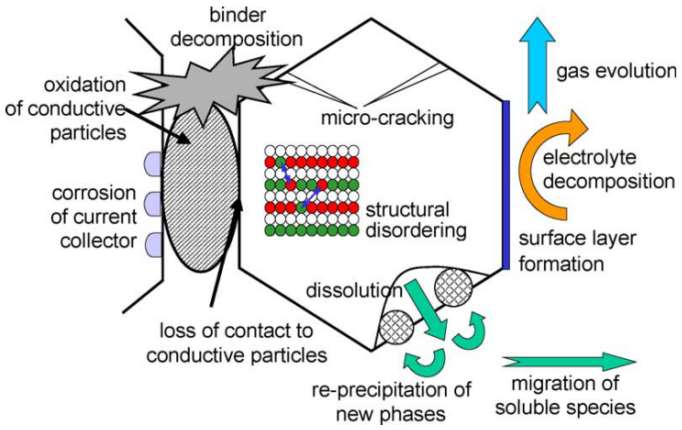

Figure 1.6.: Overview of the main aging factors at lithiated transition metal oxides as cathode according to Vetter et al. [17].

the SEI during cycle-life [17, 22, 23]. Stability, structure and conversion of the SEI as well as the impact on the cycling performance of LIBs depend on the electrolyte, in particular the solvent and the conducting salt [8, 24]. The aging effect lithium plating accelerates aging and may be hazardous for the cell life [25, 26].[2] In Figure 1.6, an overview of the main aging effects at the cathode is given. Cathode aging highly depends on the chemistry as well as on the electrochemical, thermal and mechanical stress. In example, structural changes and dissolution, respectively re-precipitation of cathode compounds may occur [17, 27].

Generally, degradation processes and their interactions are highly complex. It is mandatory that degradation of LIBs needs to be understood and reduced to extend cycle-life and to manufacture durable, safe and performant cells.

1.4. Diagnosis of Lithium-Ion Batteries: State-of-the-Art[3]

For a non-destructive determination of the SoH, in-situ electrochemical measurement methods are necessary. Generally, a battery management system would benefit from a non-destructive as well as fast, cheap and accurate SoH estimation of LIBs. Suggested methods for an implementation in a battery management system mostly are based on monitoring the current, the voltage and the temperature. Suitable methods are for example measuring the Open-Circuit-Voltage (OCV) [28] and determining the

[2] A detailed description of the origin of lithium plating as well as plating characteristics is given in Chapter 3.

[3] Parts of this section have been published in [1–3].

internal resistance via constant and pulsed current-voltage measurements [29, 30]. Other in-situ techniques that are proposed in the literature are Incremental Capacity Analysis (ICA) [31], Differential Voltage Analysis (DVA) [32] as well as combined techniques, the IC-DV analysis [33]. The most common non-destructive dynamic diagnosis method for LIBs is EIS [34, 35]. All of the previously mentioned methods, ICA, DVA and EIS, are suitable for SoH diagnosis as well as for the identification and differentiation of aging mechanisms [33, 36]. A detailed overview of the advantages as well as the drawbacks of the mentioned methods in regard to aging diagnosis as well as SoH and Remaining Useful Life estimation is given in Chapter 4.

1.4.1. Dynamic Processes: Nonlinear vs. Linear

Electrochemical and physical processes in batteries have specific current-voltage relations. Charge transfer reactions at the electrodes, namely the oxidation and reduction reaction, are nonlinear Faradaic processes with a nonlinear relationship between current and voltage, often described by Butler-Volmer kinetics:

$$j_{\mathrm{Li}} = a_s j_0 \left(\exp\left(\alpha \frac{z\eta \mathrm{F}}{\mathrm{R}T} \right) - \exp\left(-(1-\alpha) \frac{z\eta \mathrm{F}}{\mathrm{R}T} \right) \right), \tag{1.3}$$

where j_{Li} is the volume rate of lithium-ion generation, a_s is the specific surface area, j_0 is the exchange current density, F is the Faraday constant, R is the ideal gas constant, T the temperature and η the overpotential.

As well, charge and discharge processes of double-layers at heterogeneous interfaces, such as the electrode-electrolyte interfaces, can show nonlinear behaviour [37, 38]. The charge and discharge of the electrochemical double layers at interfaces is described in Equation 1.4:

$$j_{\mathrm{DL}} = a_s \cdot C_{\mathrm{DL}} \frac{\partial \Delta\phi}{\partial t}, \tag{1.4}$$

where C_{DL} is the electric double layer capacitance, t is the time, $\Delta\phi$ is the electrical potential difference, j_{DL} is the current density of the electrochemical double layer.

Further, ionic transport processes in the spherical particles of the electrodes as well as in the electrolyte occur in LIBs. Lithium diffusion in particles is expressed by Fick's law:

$$\frac{\partial c_{Li}}{\partial t} = \frac{1}{r^2} \frac{\partial}{\partial r} \left(D_{Li} r^2 \frac{\partial c_{Li}}{\partial r} \right), \tag{1.5}$$

with the lithium concentration c_{Li}, the time t, the diffusion coefficient of lithium D_{Li}

and the spatial coordinate r. The concentration profile of lithium in spherical particles is nonlinear due to the relation to current-voltage nonlinearity via Butler-Volmer kinetics. Further, the OCV depends on the lithium concentration. The translation of the lithium-ion concentration c_{Li^+} into an OCV can be given by the Nernst-equation as shown in Equation 1.6.

$$U_{OCV} = E_0 + \frac{RT}{F} \ln \frac{c_{Li^+}}{c_{Li}}, \tag{1.6}$$

with the standard potential E_0, the lithium-ion concentration c_{Li^+} and the lithium concentration c_{Li}.[4] Concerning battery modeling, an often used alternative is to implement measured OCV curves. Due to the mentioned reasons, solid diffusion processes are expected to contribute to nonlinear responses, as well. The ionic transport process in the electrolyte is expressed with a Nernst-Planck-Flux given in Equation 1.7 [39] and its impact on nonlinearities is expected to be only minor, as demonstrated in [40]. Equation 1.7, however, is only valid for binary electrolytes.

$$\varepsilon_e \frac{\partial c_e}{\partial t} = D_{e,eff} \frac{\partial^2 c_e}{\partial x^2} + (1 - t_p) \frac{j_{Li}}{F}, \tag{1.7}$$

with Li^+-concentration in the electrolyte c_e, the volume fraction ε_e of the electrolyte the time t, the effective diffusion coefficient in the electrolyte $D_{e,eff}$, the transference number t_p, the volume rate of lithium-ion generation j_{Li} and the Faraday constant F. Therefore, electrochemical reactions and solid diffusion processes in spherical particles are the main processes to contribute to NFRA on LIBs. Capacitive nonlinearities due to charging and discharging of double layers at interfaces may only be minor in comparison to Faradaic ones. Further, electrochemical aging processes, such as lithium plating, follow a Butler-Volmer relation and may cause nonlinear responses, as well.

As the measuring principle of NFRA is related to EIS which is the state-of-the-art non-destructive diagnosis method for LIBs [35, 36, 41], the next section is focused on the description of EIS.

[4] Please note that using c_{Li} in the denominator is a simplified formulation of the Nernst equation, as the lithium-ions are not reduced to elementary lithium during charging, respectively discharging process. In fact, the graphite on the anode side, respectively the lithium transition metal oxide on the cathode side are reduced.

1.4.2. Electrochemical Impedance Spectroscopy

The working principle of EIS is illustrated in Figure 1.7. Further, the theory behind this method is described in the following according MacDonald et al. [42]. With EIS,

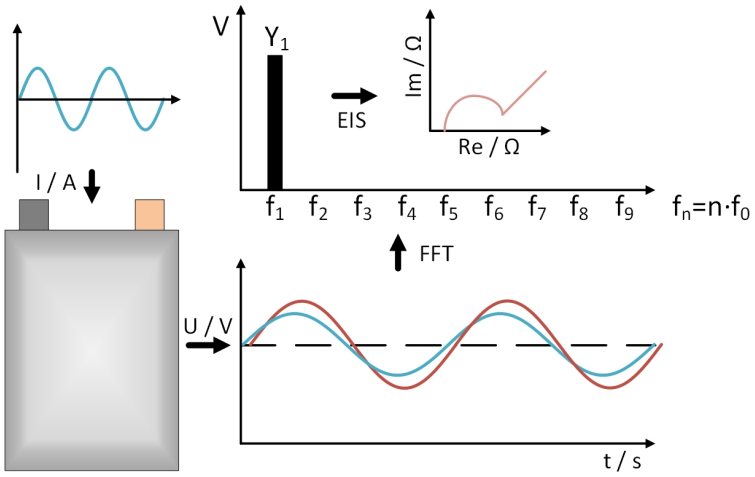

Figure 1.7.: Working principle of EIS.

the linear response of a system to a sinusoidal excitation signal, in the present thesis an alternating current, in a broad frequency range from mHz to MHz is analysed. Hereby, the alternating voltage response of the system is measured. This measurement modus is called galvanostatic modus. Alternatively, it is possible to apply a sinusoidal voltage excitation on the system and to measure the sinusoidal response. In this case, EIS is performed potentiostatically. For both measurement modi, the response signal in the time domain is transferred to frequency domain using a Fast Fourier Transformation (FFT). EIS is only valid if the following four preconditions are fulfilled, a) causality, b) time-invariance, c) stability and d) linearity [43]. A system is considered as linear, if the principle of superposition is applicable. In the case of LIBs, this principle is not valid, as the current-voltage curve shows a nonlinear relation according Butler-Volmer kinetics, given in Equation 1.3. Thus, the battery cell is linearized for impedance analysis by investigating the system at a specific, steady-state operation point using an input signal with a small amplitude to guarantee linearity of current and voltage. Thus, the cell can be analysed under the assumption of pseudo-linearity (Figure 1.8) and the principle of superposition is valid. For the galvanostatic modus, an excitation current with a small amplitude of I_{AC} of approximately C/10 is considered as sufficiently small for fulfilling the validity criteria [35]. Validity of EIS can be analysed using the Kramers-Kronig-relation.

In the present thesis, EIS is applied in the galvanostatic modus. In the following

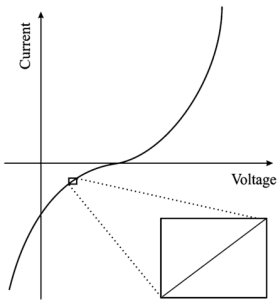

Figure 1.8.: Current and voltage relation for a pseudo-linearized LIB [44].

mathematical explanations, thus, a sinusoidal current is given as input signal and a sinusoidal voltage as output signal. The initial sinusoidal excitation with a small amplitude can be given as following:

$$I(\omega, t) = I_0 \cdot sin(\omega \cdot t), \tag{1.8}$$

with the current amplitude I_0, the angular frequency ω and the time t. The angular frequency ω is defined as:

$$\omega = 2 \cdot \pi \cdot f \tag{1.9}$$

The sinusoidal response voltage $U(\omega, t)$ of the system with the phase shift Φ and the time t is given as:

$$U(\omega, t) = U_0(\omega) \cdot sin(\omega \cdot t + \Phi(\omega)) \tag{1.10}$$

As the impedance describes the complex AC resistance and often is considered as the equivalent to the direct current (DC) resistance, the complex impedance $\hat{Z}(\omega)$ can be written in analogy to Ohm's law, given in Equation 1.11.

$$\hat{Z}(\omega) = \frac{\hat{U}(\omega)}{\hat{I}(\omega)} \tag{1.11}$$

Hereby, the input current and the output voltage are formulated using complex notation, given in Equation 1.12 and 1.13.

$$\hat{I} = I_0 \cdot \exp(j \cdot \omega \cdot t) \tag{1.12}$$

$$\hat{U} = U_0(\omega) \cdot \exp(j(\cdot\omega \cdot t + \Phi(\omega))) \tag{1.13}$$

Hence, the impedance of the system can be given using the complex notation:

$$\hat{Z}(\omega) = \frac{U_0(\omega) \cdot \exp(j(\cdot\omega \cdot t + \Phi(\omega)))}{I_0 \cdot \exp(j \cdot \omega \cdot t)} = |\hat{Z}(\omega)| \cdot \exp(j \cdot \Phi(\omega)) \tag{1.14}$$

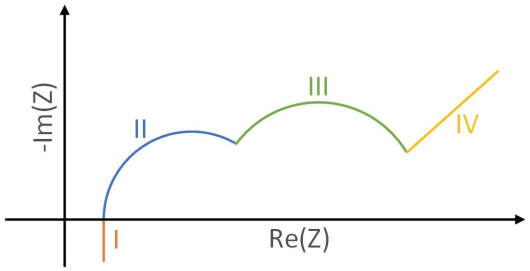

Figure 1.9.: Characteristic impedance features and the corresponding processes in LIBs.

with

$$|\hat{Z}(\omega)| = \frac{U_0(\omega)}{I_0} \tag{1.15}$$

Equation 1.14 describes the impedance in polar coordinates in dependence of the phase shift Φ as well as the absolute value of the impedance $|\hat{Z}|$. Using these frequency dependent parameters, the impedance can be analysed in the common Bode-plot. Using the Euler-relation, given in Equation 1.16, the impedance can be displayed in a Cartesian coordinate system, given in Equation 1.17.

$$\exp(j \cdot x) = cos(x) + j \cdot sin(x) \tag{1.16}$$

$$\hat{Z}(\omega) = |\hat{Z}| \cdot (cos(\Phi) + j \cdot sin(\Phi)) \tag{1.17}$$

Thus, it is possible to present the impedance in the commonly used Nyquist-Plot with the real $Re(\hat{Z})$ and the imaginary $Im(\hat{Z})$ part of the impedance, given in Equation 1.18 and 1.19.

$$Re(\hat{Z}) = |\hat{Z}| \cdot cos(\Phi) \tag{1.18}$$

$$Im(\hat{Z}) = |\hat{Z}| \cdot sin(\Phi) \tag{1.19}$$

In the present thesis, impedance results are given in the Nyquist plot. A typical impedance spectrum of a LIB in the Nyquist presentation is shown in Figure 5.10. Characteristic frequency ranges can be related to particular dynamic cell processes of LIBs [35]. In general, high frequency processes of LIBs are found on the left side of the Nyquist diagram and low frequency processes on the right side. In section I, the high frequency inductive reactance of the battery due to the cable connections and the current collectors is excited. The intersection with the x-axis of the diagram corresponds to the Ohmic resistance of the cell. The semi-circles in section II and III correspond to the charge-transfer process through double-layers at cell interfaces which typically shows capacitive and resistive behaviour. The high frequency semi-circle usually is

attributed to the ionic charge transport and accumulation at the interface between the SEI and electrolyte which depend e.g. on lithium migration and double-layer capacity. The low frequency semi-circle in section III can be attributed to the charge transfer resistance. Mostly, the charge transfer processes of anode and cathode have overlapping time constants which result in one stretched arc containing both processes. At the lowest frequencies, diffusion processes in the active material of the electrodes are excited, typically described with the Warburg element. In the literature, dynamic characterization with EIS is used for state and aging determination of LIBs [45–47]. Cell aging processes cause impedance changes and can therefore be observed using impedance techniques [17, 48]. Impedances of batteries, especially batteries with high energy densities, are typically in the lower Ohmic range «1Ω [49]. As well, complex physico-chemical processes occur in the cell and it is difficult to reliable distinguish between the electrode reactions and transport processes, as well as between the anodic and cathodic compounds [49, 50]. One possibility for the deconvolution of the overlapping cell processes is the application of the Distribution of Relaxation Times (DRT) methodology [49]. In 2002, Ivers-Tiffée et al. introduced DRT for the identification of the reaction mechanism of Solid Oxide Fuel Cells [51]. With DRT, the separation and identification of characteristic time constants of physico-chemical processes of electrochemical systems is enhanced [52]. Each process is represented by local maxima in a continuous distribution function [53]. Analysis of EIS using DRT has gained the interest of researchers in the field of LIBs and has been applied for aging characterization [52, 54] and process identification [49]. However, EIS limits analysis to the linear frequency responses and therefore a highly nonlinear electrochemical system as a LIB is analysed under the assumption of linearization. Cell processes with a nonlinear current-voltage relation, such as the electrochemical reactions at the anode and cathode according to Butler-Volmer kinetics, as given in the previous section in Equation 1.3, are only slightly excited due to the sinusoidal excitation with a small amplitude of I_{AC}, guaranteeing a linear current-voltage relation. As a result, using EIS denotes that dynamic information about the nonlinearities of cell processes is not accessed and neglected in regard to diagnosis and SoH estimation. These nonlinearities are accounted for using NFRA. In the next section, the fundamentals of NFRA are explained. Further, an overview of research fields in which nonlinear dynamic analysis methods, which are related to NFRA and already applied, is presented.

1.5. Nonlinear Analysis[5]

1.5.1. NFRA technique

Using NFRA, a novel and nonlinear insight into battery dynamics is gained. In general, nonlinear dynamic analysis methods are already applied in multiple research fields. A subclass of NFRA, namely the THD, is common in acoustics research for noise detection [55]. Further, distortions of sinusoidal current responses of lead-acid batteries to sinusoidal excitation voltages were identified by Okazaki et al. as SoC indicator [56]. In the last years, nonlinear analysis with THD has been used for electrochemical characterization of fuel cells [6, 7, 57–59]. It was shown that identification of methanol oxidation kinetics and methanol concentration monitoring for Direct Methanol Fuel Cells [6, 7] are two examples where THD was better performing than EIS. Besides, measuring THD is applicable as a quality criterion for linearity assessment and to detect nonlinearities which distort the reliability of impedance spectroscopy [60, 61]. Furthermore, NFRA has been applied to characterize electrode materials and electrochemical reactions of redox systems [62]. Extending analysis to nonlinear dimension gave a deeper insight into nonlinear physical processes governing the electrode reaction of Solid Oxide Fuel Cell cathode materials [63]. Higher harmonic analysis is further applied for characterization of corrosion processes [64, 65]. Concerning electric supply systems, higher harmonics have adverse effects, such as overheating of the electrical components. Therefore, generation of higher harmonics needs to be mitigated [66]. In general, due to their only weak nonlinear nature, capacitive nonlinearities usually have significantly smaller intensities than Faradaic nonlinearities [67]. Model-based studies that support the high potential of NFRA as dynamic method for process identification and separation have been published in the last years. NFRA studies on state-of-the-art Pseudo-Two-Dimensional [40, 68, 69] and Single-Particle [70] battery models are found in the literature that verify and strengthen the characteristic experimental findings of NFRA on LIBs. Recently, Wolff et al. published a study that identifies why and how electrochemical reactions as well as transport processes excite individual higher harmonics by using simple fundamental models [71].

With NFRA, a sinusoidal input signal with a high amplitude of I_{AC} is applied to the system in a defined frequency range from mHz to kHz. The working principle is

[5] Parts of this section have been published in [1, 2, 4]

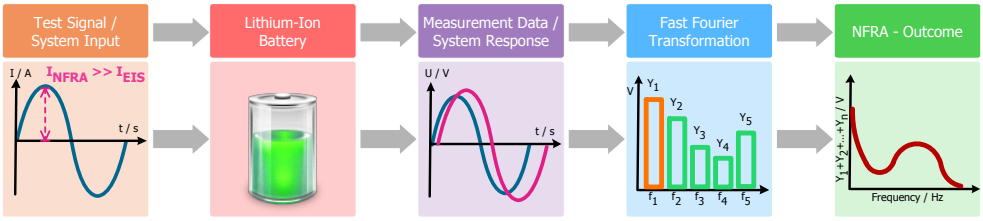

Figure 1.10.: Working principle of NFRA [3].

shown in Figure 1.10. The sinusoidal voltage output U_{AC} is measured in the time domain and transferred to the frequency domain via a FFT. However, not only the amplitude of the sinusoidal voltage signal corresponding to the input frequency Y_1, but also the amplitudes of the higher harmonic responses Y_n with $n \geq 2$ can be detected. Higher harmonic amplitudes Y_n are observed at multiples n of the fundamental frequency f_1 of the sinusoidal input signal:

$$f_n = n \cdot f_1 \tag{1.20}$$

Due to their different parities, even Y_{2n} and odd harmonics Y_{2n+1} each have a different characteristic dependency on the input amplitude and frequency. As nonlinear system analysis has no standardised unique theory based on control engineering, different measurement and interpretation approaches have been used in the literature to study the nonlinear voltages responses of electrochemical systems. Currently, it is not yet clear how to best trigger, analyse and interpret nonlinear responses. The amplitudes of the individual higher harmonic voltage responses Y_n as well as the overall amplitudes of nonlinear responses of LIBs can be analysed. Beside the root mean square of the first two harmonics Y_{rms} (Equation 1.21), the sum of higher harmonics $\sum_{n=2}^{5} Y_n$ and the square root of the sum of the squared amplitudes of higher harmonics $\sqrt{\sum_{n=2}^{5} {Y_n}^2}$ have been used in this thesis and the corresponding publications [1–3, 40].

$$Y_{rms} = \sqrt{\frac{\sum_{i=2}^{3} Y_n^2}{2}} \tag{1.21}$$

Primarly, the sum of the individual amplitudes of the higher harmonic responses of LIBs has been calculated and analysed. As the establishment of the methodology proceeded, the calculation for the overall nonlinearity was extended to the square root of the sum of the squared amplitudes, because it emerged that the second and third harmonic have the highest proportion of the overall nonlinear voltages responses. The

final evaluation form of NFRA is the root mean square as it is a well known measure in metrology and electrical engineering, also for THD [6], and it gives a sound mean value of the overall nonlinearity of a system. As the root mean square requires division by the number of higher harmonics, comparability of the root mean square will be only given if the same number of higher harmonics is used. Distinct nonlinearities are only visible for Y_2 and Y_3, and their comparison allows to distinguish between aging phenomena [2]. The excitation amplitudes are therefore chosen so that nonlinear responses for Y_2 and Y_3 are visible, but all further higher harmonics, i.e. i>3, are negligible. This also prevents interference of the signals [72]. The recommendation of the root mean square Y_{rms} as final evaluation form of NFRA is one of the key findings of this work regarding the establishment of the method. Within this work, the term "nonlinear frequency responses", abbreviated as NFR, is used as a synonym for the overall amplitudes of higher harmonics that are excited with NFRA, independent of the calculation formula.

1.6. Scope of the Work[6]

In the present study, NFRA is established as a dynamic analysis method of LIBs. Currently, state-of-the-art dynamic analysis measurement methods as the established EIS analyses LIBs in regard to linear system behaviour. Thereby, information about the nonlinear processes is only accessed under the assumption of a linear correlation between current and voltage. Nonlinear analysis of highly nonlinear dynamics has been neglected so far and the maximum potential of dynamic analysis of LIBs is not exploited. This is now taken into account using NFRA. The focus of this thesis is the experimental investigation of how to use NFRA for dynamic characterization of LIBs and the evaluation of highly informative NFRA data in regard to battery aging and SoH estimation. In Chapter 2, the fundamentals of using NFRA on LIBs are established. First, the amplitude dependency is investigated to evaluate the necessary excitation amplitude and frequencies at which higher harmonic responses with a sufficiently high intensity are excited. Hereby, the progression and amplitudes individual higher harmonics and the overall NFR are analysed in dependence of the frequency. Based on this, process characterization is performed by correlating nonlinear signals to the established EIS. This is supported by an excursus in which the temperature de-

[6] Parts of this section have been published in [1–4].

pendency of NFRA and the impact of aging on NFRA is investigated.[7] In Chapter 3, the sensitivity of NFRA to cell and measurement parameters is evaluated. The impact of measurement conditions and measurement parameters on NFRA is evaluated. Further, NFRA is applied on multiple cell types and designs to demonstrate the universal applicability of NFRA. Generally, Chapter 2 and 3 proof the applicability of NFRA and are a guideline in regard to reliable and reproducible dynamic analysis of LIBs using NFRA.

In Chapter 4, the focus is laid on provoking of different aging effects and the identification of the impact of these degradation effects on the highly sensitive nonlinearities. Cyclic aging effects at -10°C and 25°C are excited and studied dynamically with NFRA and EIS. Ex-situ analysis is done by characterizing the electrodes using digital microscopy. In Chapter 5, different approaches for the evaluation of highly informative NFR aging data-sets are used to estimate the SoH. In the first part of this chapter, a case study using a data-mining approach based on Support-Vector-Regression (SVR) is implemented. A degradation model is calculated and validated on NFR test-data sets of identical and not-identical LIBs. In the second part of the chapter, a different approach for the SoH estimation based on NFR data is presented. NFR in the characteristic frequency range for the electrochemical reactions is correlated to the capacity fade due to loss of active material. The results are verified by using a reaction model in which an electrode reaction based on Butler-Volmer kinetics is implemented. Overall, NFRA is identified in Chapter 5 as a reliable, easily measured and evaluated dynamic analysis method for the estimation of the SoH of LIBs.

[7] Aging analysis and SoH estimation of LIBs using NFRA are discussed in detail in Chapter 4 and 5.

Chapter 2

Basic Nonlinear Frequency Response Analysis[1]

2.1. Introduction

For optimization of the LIB technology and aging characterization, it is essential to understand electrochemical and physical processes in the cell. The most common non-destructive measurement technique is EIS [35, 36, 41]. As described in Chapter 1, EIS limits analysis to linear frequency responses. As processes with a strongly nonlinear current-voltage relation occur, using EIS denotes that essential dynamic information about the nonlinearities of processes is not accessible and therefore not accounted for. In contrast, this information is accessed by NFRA. Prior to this work, NFRA has not been applied yet to identify and analyse processes in LIBs.

Within the first part of this chapter, method establishment of NFRA is presented to get a novel and more detailed insight into the dynamic behaviour of LIBs by analysing the dependency of the nonlinear responses of the excitation amplitude and thereby determining the transition from linear to nonlinear analysis. Further, higher harmonic responses of NFRA are correlated with impedance results and temperature dependent measurements for process identification and characterization. In the second part of this chapter, an investigation of the general applicability of NFRA for diagnosis of battery aging is presented.

[1] Parts of this chapter have been published in [1].

2.2. Experimental

2.2.1. Cells

Multiple LIBs in the pouch format with NMC as cathode and graphite as anode material were measured. Electrode manufacturing and cell assembling was done by the BatteryLab Factory Braunschweig (BLB). A solvent mixture of ethylene carbonate (EC)/diethyl carbonate (DEC) with a ratio of 3:7 with 1 M lithium hexafluorophosphate ($LiPF_6$) as conducting salt and Celgard 2320 as separator were used. The inactive compounds are polyvinylidene fluoride (PVDF) as binder and carbon black (CB) as conducting additive. The performance parameters initial capacity C_0 and initial internal resistance R_0 as well as the characteristic cell parameters are listed in Table 2.1. The specific surface area a_s of anode and cathode can be calculated from the provided parameters with the equation $a_s = 3\frac{\varepsilon_{a/c}}{R_p}$ with the active material volume fraction $\varepsilon_{a/c}$ and the particle radius R_p [39]. Cell 1, 3 and 4 have identical characteristic cell parameters. The electrode composition of cell 2 slightly differs: it has larger mass fractions of active materials and smaller mass fractions of inactive compounds of anode and cathode than the other cells. This could result in an inferior electrical conductivity and lead to higher electrode resistances compared to cells 1, 3 and 4. Volume fraction of the anode ε_a and the cathode ε_c and electrode thicknesses δ_a and δ_c of cell 2 are comparable to the other cells. In general, parameter values are similar to literature. [39, 73]. Small deviations between performance parameters of all cells can result from the manual manufacturing process.

2.2.2. Measurements

NFRA and EIS were measured with a Zahner Electrochemical Workstation (Zennium) in galvanostatic mode. The frequency range was set between 20 mHz and 5 MHz, discretized with ten frequencies per decade above 66 Hz and five frequencies per decade for frequencies below 66 Hz. As recommended by the manufacturer, the sweep starts at a medium frequency of 1 kHz, runs upwards to higher frequencies and then turns to measure the lower limit of the frequency range [74]. If not further declared, all NFRA measurements within this work follow this sweep protocol. Higher harmonics in the excitation signal are measured and corrected by the device which allows

Parameters	Symbol	Cell 1	Cell 2	Cell 3	Cell 4
Initial capacity	C_0 / mAh	32.8	31.6	32.9	32.9
Initial resistance	R_0 / Ω	0.21	0.29	0.16	0.16
Anode thickness	δ_a µm	44	50	44	44
Cathode thickness	δ_c µm	52	51	52	52
Calendering degree anode	Π_a / %	10	10	10	10
Calendering degree cathode	Π_c / %	10	10	10	10
Mass fraction anode	ζ_a / wt%	0.90	0.93	0.90	0.90
Mass fraction cathode	ζ_c / wt%	0.90	0.92	0.90	0.90
Mass fraction inactive compounds anode	$\zeta_{add,a}$ / wt%	0.10	0.07	0.10	0.10
Mass fraction inactive compounds cathode	$\zeta_{add,c}$ / wt%	0.10	0.08	0.10	0.10
Volume fraction anode	ε_a / -	0.60	0.59	0.60	0.60
Volume fraction cathode	ε_c / -	0.57	0.55	0.57	0.57
Geometric surface area anode	$A_{geo,a}$ / cm^2	30.25	30.25	30.25	30.25
Geometric surface area cathode	$A_{geo,c}$ / cm^2	30.25	30.25	30.25	30.25

Table 2.1.: Performance and cell parameters of the investigated cells.

assigning of higher harmonic responses in the output signal to the measured cell.[2] Amplitudes of higher harmonics from the Y_2 to Y_{10} are measured and measurement noise is recorded. Table 2.2 gives an overview of the experiments. As explained in the introduction, multiple data evaluation types of NFRA have been investigated within this work. In this chapter, the sum of amplitudes of higher harmonics, $\sum_{n=2}^{5} Y_n$ and the amplitudes of individual higher harmonics Y_n are analysed. Y_1 is the linear response with $n = 1$ corresponding to $|Z|$ by the relation $|Z| \cdot I_{AC} = Y_1$ which is analysed in EIS.

Experiment	**Purpose**
Variation of I_{AC}	Defining nonlinear amplitude range
EIS vs. NFRA	Process identification
Temperature variation	Process identification
Aging by cycling	Identification of aging

Table 2.2.: Overview of the experiments that are performed for the establishment of NFRA on LIBs.

Measurements were performed in a temperature chamber at a constant environmental temperature of 25±1°C and at 50% SoC, if not further declared. The SoC is set by charging of the cell with 1 C CC/CV with CV until the current decreased to C/20. Afterwards, the cell is discharged with 0.5 C CC to 50% SoC. For dynamic analysis and for operation, a temperature increase in the cell may be possible due to cell polarization processes and entropy changes, especially for high excitation currents as used with NFRA [75]. With an infrared thermographic camera[3] a surface temperature increase of approximately 1 K with an amplitude of I_{AC} of ≥1.5 C for NFRA measurements was observed. As one-layered pouch cells with small capacities are used, the large surface area of the cells allows a fast removal of produced heat and as such shows quasi-thermal behaviour. Therefore, the impact of internal cell heating on the spectra is neglected in this study. Amplitude dependency is evaluated at cell 1 at 50% SoC. NFRA was measured with different excitation amplitudes of I_{AC} given in Table 2.3 in the overall frequency range. The DC bias is set to 0 A. In addition, individual higher harmonics Y_n for 2≥n≤10 and noise of NFRA measurement are exemplary

[2] A detailed description of this data correction is given in the Appendix.
[3] FLIR SC325 with a measurement accuracy of ±2°C or ±2% of reading.

I_{AC} / mA	C-rate / -
1	0.03
5	0.15
10	0.30
20	0.60
50	1.50
100	3.00

Table 2.3.: Evaluated amplitudes of I_{AC} and corresponding C-rates for NFRA at cell 1.

analysed on cell 2 for an amplitude of 1.5 C to identify the contribution of the single higher harmonics to the overall NFR. To provide information about process identification and reproducibility, NFRA and EIS are compared for cell 2 and 3 at 25°C. At cell 3, temperature dependency of NFRA and EIS is analysed as electrochemical and physical processes are temperature dependent. Parameters of these experiments are listed in Table 2.4. Aging experiments of LIBs via cycling at 25°C were conducted by

Experiment	Amplitude EIS;NFRA	Temperature /°C	Cell
EIS vs. NFRA	C/15;1.5C	25	2, 3
Temperature variation	C/15;1.5C	5, 10, 25	3

Table 2.4.: Measurement parameters for process identification experiments with NFRA.

charging with 1 C constant current (CC)/constant voltage (CV) and discharging with 1 C CC in a potential window between 2.9 V and 4.2 V at cell 4 using a MACCOR Battery Test System (Model 4200). Dynamic measurements were performed prior to aging and after each 50^{th} cycle at 50% SoC. Amplitude for EIS was set to 2 mA (C/15) and for NFRA to 50 mA (1.5 C).

2.3. Results and Discussion

2.3.1. Defining Nonlinear Amplitude Range[4]

For method establishment of NFRA, it is essential to evaluate amplitude dependency of higher order frequency responses to determine the transition from linear to nonlinear responses. In Figure 2.1, amplitude dependent NFR measurements are shown. The excitation amplitude of I_{AC} (left y-axis) and the overall NFR (right y-axis) are shown for frequencies ranging from 0.02 Hz to 10 kHz; for higher frequencies only inductive behaviour can be assumed. Two frequency ranges with characteristic response signals (I, II) are identified in Figure 5.11.

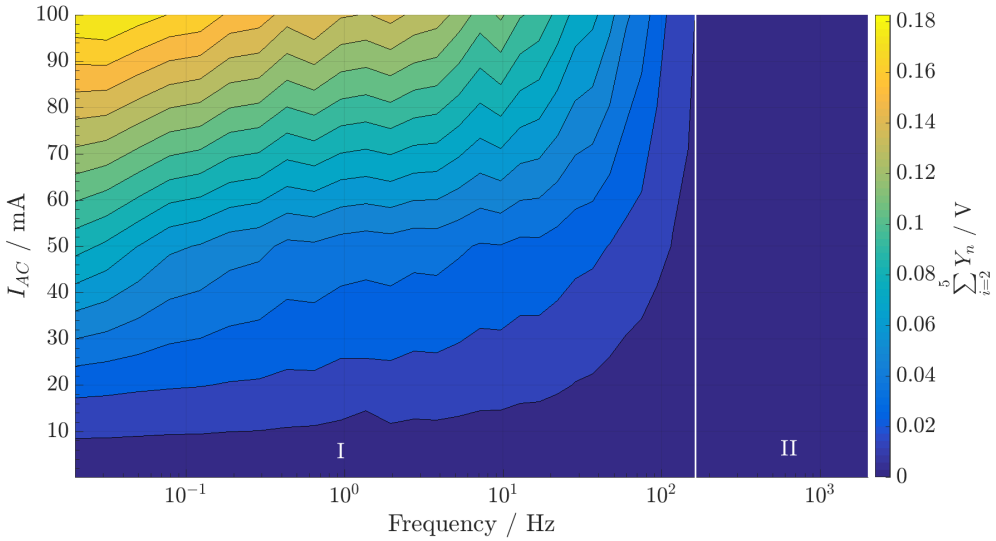

Figure 2.1.: NFR for different amplitudes of I_{AC} of cell 1 measured at 25°C.

In the frequency range I from 0 Hz to approximately 200 Hz a correlation between NFR, frequency and amplitude is detected: nonlinear responses and therefore distortions of the sinusoidal output increase with increasing amplitude, and the overall NFR decrease with increasing frequency for all amplitudes. Note that a nonlinear response of a given frequency denotes that nonlinear processes with time constants τ in this frequency range are excited. In frequency range II from approximately 200 Hz to 10 kHz, nonlinear responses are very low with a maximal magnitude of 10^{-3} V and depend only slightly on the excitation amplitude (not visible in Figure 1). Concluding, nonlinear processes and as such reaction processes are not excited at frequencies higher than approximately 200 Hz for the investigated cell. Responses in range II may correlate to faster processes such as charging of double-layers of heterogeneous

[4]Parts of this subsection have been published in [4].

interfaces and ionic transport processes between and in the SEI and electrolyte. For amplitudes of I_{AC} below 20 mA (smaller than 0.6 C), nonlinear responses are very low and almost constant in frequency range I. This denotes that for dynamic analysis with NFRA on the inspected cells a high sinusoidal current of at least 50 mA (1.5 C) should be used to detect nonlinearities. Generally, the application of I_{AC} with a high amplitude may damage the cell and enhance aging [76]. However, whether and in what extent cell aging may be caused by NFRA strongly depends on the measurement conditions. For example, lithium plating may be caused, if a low-frequency AC current with a high amplitude is applied to the cell at very high SOCs at low temperatures [14]. As well, a sinusoidal excitation may only enhance aging, if it is constantly superimposed on a direct current load during long time cycling studies due to additional heat generation [76, 77]. Therefore, additional aging induced by measurements of NFRA is considered negligible.

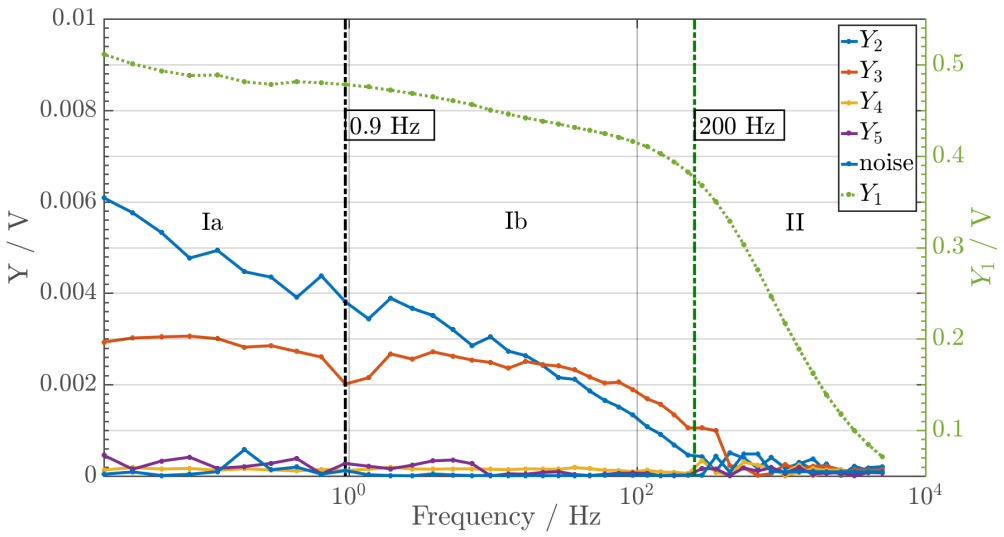

Figure 2.2.: Y_2 to Y_5 and noise (left y-axis) and Y_1 (right y-axis) of cell 2 measured with I_{AC}=1.5 C at 25°C.

In Figure 2.2, the amplitudes of Y_2 to Y_5 and noise (left y-axis) as well as the amplitude of Y_1 (right y-axis) measured with an amplitude of 50 mA (1.5 C) of cell 2 are exemplary shown and analysed. Y_6 to Y_{10} are not shown as they are significantly smaller than the noise signal. Similarly as for Figure 2.1, two frequency ranges (I and II) separated at approximately 200 Hz with different sensitivities to NFRA are visible. Y_2 and Y_3 have the highest values and therefore contribute most to nonlinear responses. Magnitudes of Y_n with n$\geq$4 have amplitudes in the same magnitude as noise measurements which is one order of magnitude lower than Y_2 and Y_3; they are

thus not further analysed. Probably due to different parities and therefore different zero-crossings in the time-domain, Y_2 and Y_3 have different characteristic progressions and characteristic features: Y_3 has a local minimum at approximately 1 Hz and Y_2 has a steeper slope in range I. Range I is divided at the frequency of the local minimum in Y_3 into two range Ia and Ib. The linear response Y_1 is two orders of magnitude higher than the amplitudes of higher harmonics. Y_1 increases monotonously from 10^{-4} V for 10 kHz to 0.35 V for approximately 200 Hz. In contrary to this, amplitudes of higher harmonics are very low in this range and have a constant value of approximately 10^{-3} V. As priorly stated, nonlinear processes only have a small impact on the higher harmonic responses in range II. For frequencies smaller than approximately 200 Hz, Y_1 increases only slightly from 0.35 V for approximately 200 Hz to 0.5 V for 0.02 Hz. Y_2 and Y_3, however, are excited within this range and show characteristic progressions. By only investigating Y_1, it cannot be distinguished between characteristic frequency ranges as for Y_2 and Y_3. Concluding, the focus is laid on the analysis of Y_2 and Y_3 as well as EIS with linear amplitude, displayed in a Nyquist-Plot.

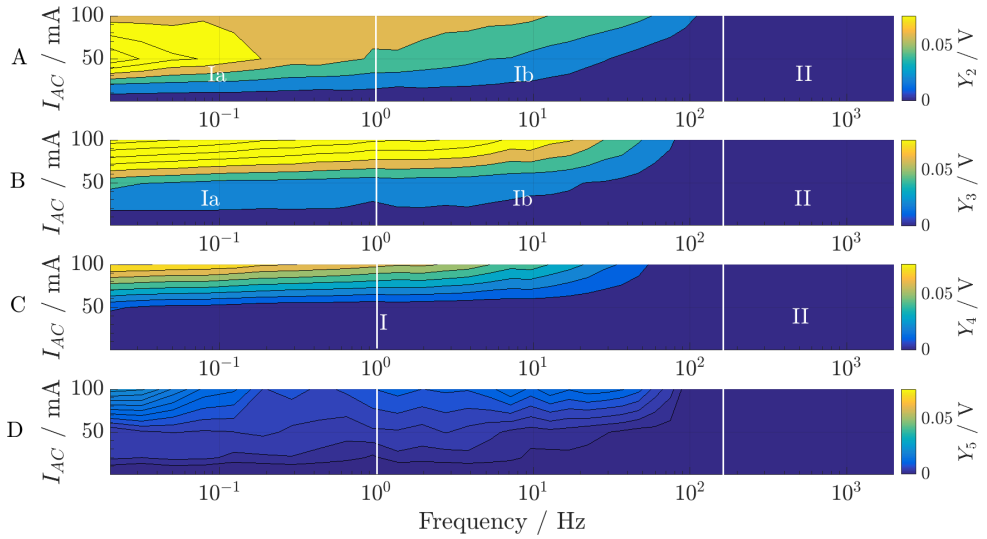

Figure 2.3.: Y_2 to Y_5 for different amplitudes of I_{AC} of cell 1 measured at 25°C. Evaluated excitation currents are 0.03 C, 0.15 C, 0.30 C, 0.60 C, 1.50 C, 3.00 C.

Due to the different progressions of Y_n, shown in Figure 2.2, it is consequential to not only analyse amplitude dependency of NFR as shown in 2.1 for cell 1, but to also investigate the amplitude dependency of the individual higher harmonics. In Figure 2.3, the relation between amplitude and Y_2 to Y_5 is shown as a function of frequency. In frequency range II, higher harmonic responses are significantly lower and only slightly amplitude dependent, suggesting weak nonlinearity of the processes. For fre-

quency range I, Y_5 increases only slightly with amplitude, whereas Y_4 has a stronger dependency. Besides, Y_3 shows larger voltage response values than Y_4 and Y_5. For amplitudes smaller than 50 mA (1.5 C), Y_2 has the largest voltage responses. Y_2 also shows a maximum around 50 mA. For an amplitude of approximately 100 mA (3 C), Y_3 surpasses Y_2. The observed different dependency of Y_2 and Y_3 for this amplitude may also be correlated to different parities of higher harmonics. However, physical interpretation requires additional, ideally model-based studies and is out of scope in this work. In-depth model based studies using various battery models are presented by Wolff et al. [40, 70] and Murbach et al. [68, 69].

2.3.2. Process Identification

In the following section, the focus is set on process identification and analysis of identified characteristic frequency ranges with NFRA. Therefore, amplitudes and progressions of higher harmonics are correlated with corresponding impedance spectra. For EIS, process identification is well established and characteristic frequency ranges are identified [35].

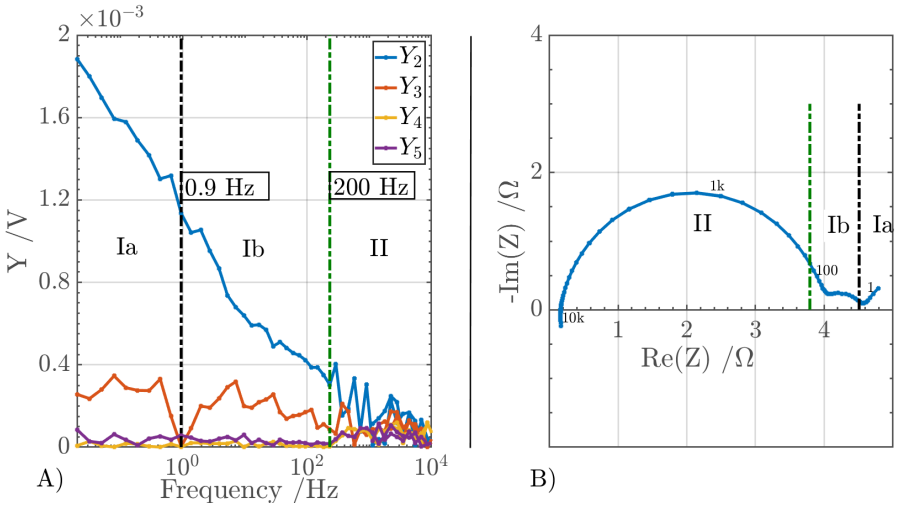

Figure 2.4.: (A) Higher harmonics spectrum and (B) impedance spectrum of cell 3 for $I_{AC,NFRA}$=1.5 C and $I_{AC,EIS}$=C/15 at 25°C.

In Figure 2.4, higher harmonics and impedances in the Nyquist-Plot of cell 3 are shown. Similar features as for cell 1 and 2 are found for NFRA of cell 3. Y_3 has again a minimum at 1 Hz, indicating that the dominating processes may have changed. At this frequency, impedances show a local minimum, too. Therefore, range I is divided again into two ranges Ia and Ib. Frequency range Ia is set from 0.02 to 1 Hz and range

Ib from 1 Hz to approximately 200 Hz. Above 200 Hz, Y_2 to Y_5 fluctuate at a constant voltage level of approximately $0.2 \cdot 10^{-3}$ V. This division into the frequency ranges Ia, Ib and II is consistent with the evaluation of amplitude dependent voltage responses shown in Figure 2.3. It is suggested that three frequency ranges are identifiable with NFRA.

The characteristic frequency ranges Ia, Ib and II iof NFRA correlate very well to the characteristic features of the impedance spectrum in Figure 2.4B. These are typical and in the literature well-known frequency ranges for processes in EIS [22, 35] where in each range specific impedance features, such as a Warburg impedance (range Ia) and semi-circles (range Ib and II) are visible. Therefore, range Ia is assigned to slow processes, e.g. solid diffusion in spherical particles which influence electrode potential due to concentration changes. Range Ib correlates to the low frequency semi-circle and is most probably assigned to electrode reactions of anode and cathode. As for the EIS, one cannot separate between the individual electrode reactions in range Ib.

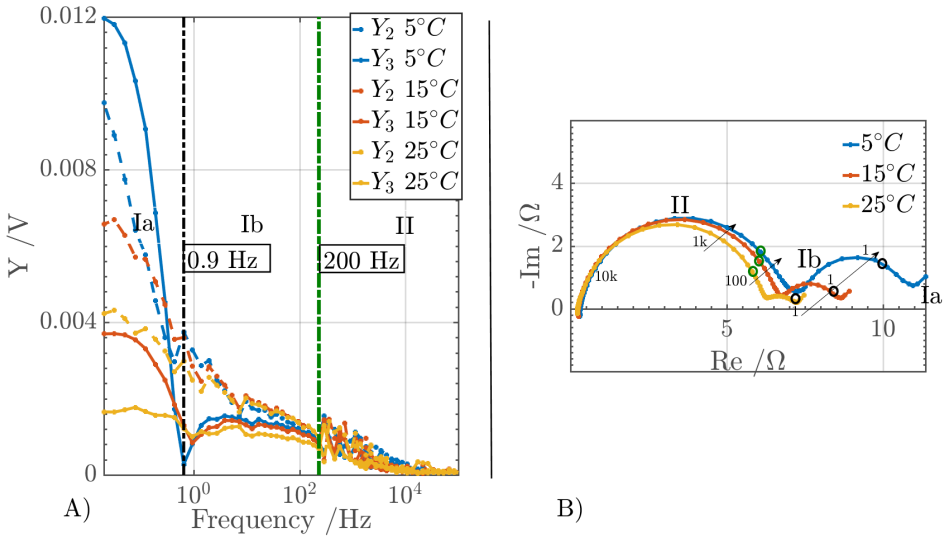

Figure 2.5.: (A) Higher harmonics spectra and (B) impedance spectra of cell 3 measured at 5°C, 15°C and 25°C for $I_{AC,NFRA}$=1.5 C and $I_{AC,EIS}$=C/15.

Those correlations of range Ia and Ib are supported by temperature dependent NFRA and EIS measurements of cell 3 shown in Figure 2.5. Y_2 and Y_3 are strongly temperature-dependent in range Ia, as seen in Figure 2.5A. At temperatures lower than standard measurement temperature 25°C, solid diffusion processes are slowed down and the impact of concentration profile in particles on the performance relevant surface concentration becomes more important. Therefore, higher harmonic responses may increase significantly for decreasing temperatures in range Ia. In EIS, shown in Figure 2.5B, time constants of diffusion and electrode reactions overlap with lower measure-

ment temperature: characteristic Warburg impedance starts at lower characteristic frequencies compared to impedance measurements at standard measurement temperature and has increased signals. With NFRA, however, slow processes in frequency range Ia can be separated at approximately 0.9 Hz from processes in frequency range Ib. The local minimum in Y_3 is even more distinct in the spectrum at 5°C than in the spectrum measured at 25°C.

Concerning correlation of range Ib to electrode reactions, the diameter of the semi-circle increases significantly with decreasing temperature as electrochemical reactions are strongly temperature-dependent according to the Arrhenius-equation:

$$k = A \cdot \exp(\frac{-E_a}{\mathrm{R}T}), \tag{2.1}$$

with the reaction rate constant k, the pre-exponential factor A, the activation energy E_a, the temperature T and the universal gas constant R. Additionally, Y_3 increases with decreasing temperature due to higher reaction resistances. However, temperature dependency of amplitudes of higher harmonics in Ib is not as distinct as in frequency range Ia and in EIS. A possible explanation is that electrochemical reactions are strongly dependent on diffusion and therefore slow mass transport of lithium-ions is a more limiting process at the high excitation amplitude of NFRA at low temperatures than the electrochemical reactions. Nonetheless, the observation that the non-linear responses in range Ib, assigned to electrochemical processes, are only slightly temperature dependent in comparison to slow processes in range Ia and the linear analysis with EIS, should be subject of further NFRA investigations. Frequency range II of NFRA correlates to the semi-circle at high frequencies, seen in Figure 2.4B, attributed usually to ionic transport processes, e.g. migration, at the boundary between and in the SEI and electrolyte. Such transport processes are usually faster and thus have higher characteristic frequencies than electrode reactions [22]. Here, it is important to note that NFRA, but not EIS, contains decisive additional information on the studied process: the ionic transport of lithium-ions between and in the SEI and electrolyte is not an electrochemical reaction and as such does not cause significant nonlinear responses, as seen in NFRA. Y_2 to Y_4 in range II are approximately constant with a value of $0.2 \cdot 10^{-3}$ V, adding to the hypothesis that this frequency range does not contain reactions. Temperature dependency of impedances and amplitudes of higher harmonics in this frequency range are significantly smaller. Concluding, characteristic frequency ranges with the particular dominating processes are: range

Ia ranging from 0.002 Hz to 1 Hz for solid diffusion processes, range Ib ranging from 1 Hz to approximately 200 Hz for electrode reactions and range II for faster processes such as ionic transport between and in the SEI and electrolyte ranging from approximately 200 Hz to 10 kHz. Consequently, frequency ranges for characteristic processes in LIBs are identifiable with NFRA. They are listed with the corresponding time constants τ in Table 2.5.

τ / s	ω-range / Hz	Process
50 to 1	0.02 to 1	Solid diffusion
1 to 0.005	1 to 200	Electrochemical reactions
0.005 to 0.0001	100 to 10k	Ionic transport processes between and in the SEI and electrolyte

Table 2.5.: Time constants and frequency ranges of nonlinearities identified with NFRA.

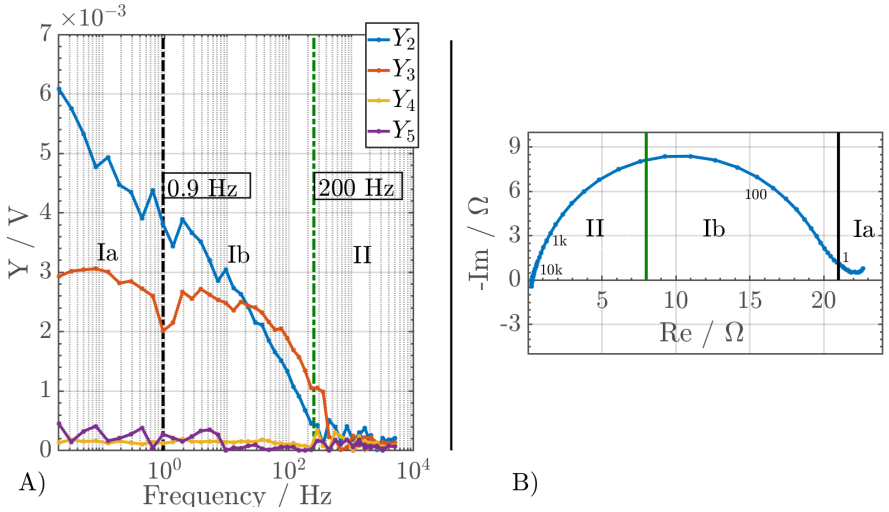

Figure 2.6.: (A) Higher harmonics spectrum and (B) impedance spectrum of cell 3 measured for $I_{AC,NFRA}$=1.5 C and $I_{AC,EIS}$=C/15 at 25°C.

Additionally to the investigation of cell 3 concerning process identification, cell 2 is analysed. Characteristic cell parameters of cell 2 differ from the other cells, as discussed in section 3. Again, amplitudes of higher harmonics are correlated to the impedance spectrum. With EIS, cell 2 performed significantly different than cell 3 due to a different electrode composition with less conducting additives: just one semicircle is visible in the Nyquist-Plot. Additionally, the cycle diameter is significantly larger than for cell 3, shown in Figure 2.6B. For NFRA shown in Figure 2.6A, the char-

acteristic frequency ranges I and II can be identified for Y_2 which are consistent with the characteristic frequency ranges for the first cell analysed in Figure 2.4. Y_3, again, shows a minimum at approximately 1 Hz, allowing again categorization in frequency ranges Ia and Ib. Therefore low frequency range Ia, again, is correlated to solid diffusion processes, mid-frequency range Ib from 1 Hz to approximately 200 Hz to the electrode reactions and frequency range II from approximately 200 Hz to 10 kHz to the only small nonlinearities of ionic transport processes between and in the SEI and electrolyte.

In the impedance spectrum in Figure 2.6B, however, the transition from electrode reactions as dominating processes to ionic transport between and in the SEI and electrolyte is not visible and as such the processes are not separable with EIS. Here, NFRA has an advantage: even if processes cannot be separated with EIS, they might be better separable with NFRA due to their different nonlinear behaviour. This distinct separation of frequency ranges between nonlinear responses of electrochemical reactions and ionic transport processes between and in the SEI and electrolyte makes NFRA highly attractive as dynamic method for analysis and state estimation of LIBs.

2.3.3. Aging

Finally, the effect of aging on NFRA and analysis with EIS is studies. Cell 4 is aged with cycling at constant temperature of 25°C. In Figure 2.7A, Y_2 and Y_3 and in Figure 2.7B the corresponding impedance measurements after 0, 200 and 400 cycles are shown. Aging cells by cycling at 25°C results particularly in electrolyte degradation and consequently in SEI layer growth [78]. This is confirmed by impedance results in Figure 2.7B. Diameters of semi-circles are largest for EIS after 400 cycles suggesting worse reaction and SEI performance. Capacity decreases from 32 to 29 to 9 mAh for 0, 200 and 400 cycles, respectively. Due to SEI layer growth, the internal resistance will increase which is slightly visible in the impedance spectra.

As in previous sections, higher harmonic amplitudes can be divided into ranges Ia, Ib and II with identical frequencies separating the zones for processes. Responses in region II are unaffected. However, Y_2 and Y_3 increase with cycling in region Ia and Ib, shown in Figure 2.7A. However, Y_2 and Y_3 do not change qualitatively. Characteristic features as the local minimum of Y_3 and the steep slope of Y_2 in the range Ia and Ib as well as the frequencies which separate the regions, remain for all investigated cycles. If the SEI layer grows, the capacity of the cell decreases. Additionally, the perfor-

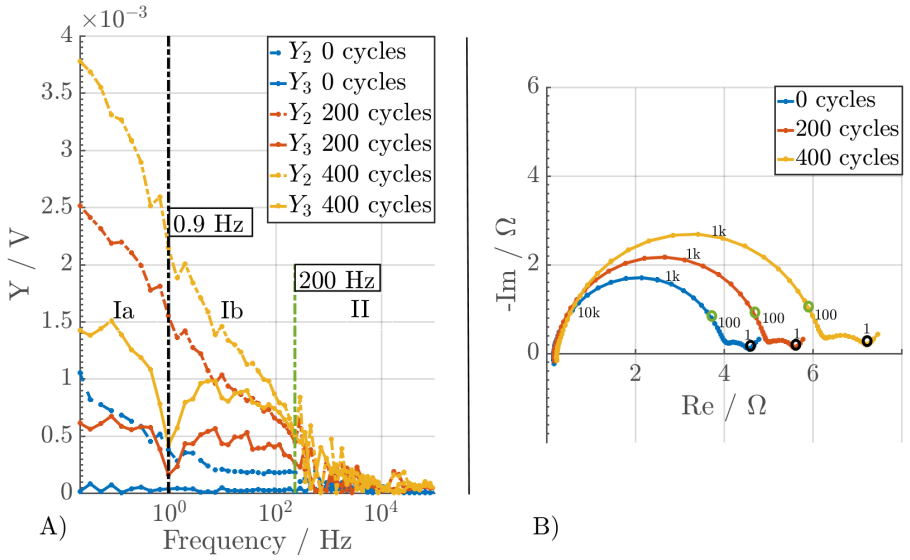

Figure 2.7.: (A) NFR spectra and (B) impedance spectra in the course of aging of cell 4 measured for $I_{AC,NFRA}$=1.5 C and $I_{AC,EIS}$=C/15 at 25°C.

mance of the cell decreases due to an increased internal resistance. Consequently, overpotentials increase for equal excitation currents of dynamic analysis, as measured in the presented aging study. Therefore, amplitudes of Y_n will increase in the overall frequency range sensible to nonlinearities, as seen in range Ia and Ib.
Concluding, it is suggested that increasing nonlinear voltage responses with aging may be related to increased overpotentials due to increasing SEI resistances and capacity loss during aging.

2.4. Conclusions

In this chapter, dynamics analysis with NFRA has been established on LIBs. It was demonstrated that NFRA extends linear dynamic analysis to nonlinear dimension by increasing the excitation amplitude of I_{AC}. Therefore, dynamic analysis of a strictly nonlinear system is no longer performed only in the linear region as with EIS. Distinct NFR are excited and visible in the spectra for the analysed cells. Characteristic nonlinearities that have been identified are Faradaic processes such as electrode reactions, solid diffusion in particles and ionic transport processes between and in the SEI and electrolyte which, however, show minor nonlinear behaviour than the others. Further, it was shown that typical frequency ranges for these dynamic processes may be distinguishable with NFRA, in cases where they cannot be distinguished with EIS. Additionally, the analysed cells have comparable nonlinear responses for Y_2 and

Y_3 as well as same characteristic features, such as the local minimum in Y_3 and the steep slope of Y_2. Thereby demonstrating the reproducibility and applicability of the method for analysis purposes. As such, NFRA is suggested as an advanced dynamic method for analysing LIBs. In Chapter 3, a sensitivity analysis of NFRA to cell specifications, measurement parameters and conditions is given.

Chapter 3

Sensitivity to Cell and Measurement Parameters [1]

3.1. Introduction

Electrochemical characterization of battery systems with dynamic measurement methods is strongly impacted by measurement conditions, i.e. SoC and temperature. Impedance characteristics drastically vary in size, and a shift of characteristic frequencies may be observed in dependence of the measurements conditions [35, 79]. Further, measurement parameters, such as the excitation amplitude of I_{AC} [35, 60], the number of oscillations n_v and the data points per frequency decade n_p, may have an impact on dynamic analysis. In case of EIS, the choice of measurement parameters has been extensively studied to guarantee validity of impedance analysis [35, 61, 80]. The amplitude of I_{AC} has to be set precisely to decrease impedance distortions caused by measurement noise and higher harmonic content [60]. Typically, multiple oscillations per frequency are measured to increase measurement accuracy. In case of EIS, the equilibrium state of the cell is not affected for a variation of n_v. Time and accuracy of impedance measurement changes with n_v.

For NFRA, the impact of measurement conditions and measurement parameters on the nonlinear spectra has not been analysed yet. This evaluation is highly important to guarantee reliable and precise nonlinear dynamic cell characterization and taken into account in this chapter. The study is complemented by a study of the effect of different cell types and designs on NFRA as well as a reproducibility analysis.

[1] Parts of section 3.3.2 have been published in [70].

3.2. Experimental

3.2.1. Cells

In Table 3.1, characteristics of the cell types and designs of LIBs evaluated in this chapter are listed. The LIBs investigated in the particular experiments are given in the corresponding measurement description.

Cell	Characteristic	Design	Type	Chemistry	Capacity	Manufacturer	Electrode Area
1	High Energy	Pouch cell	One layer	NMC/C	0.03 Ah	BLB[2]	25 cm^2
2	High Energy	Pouch cell	15 layers	NMC/C	9 Ah	BLB	5000 cm^2
3	High Energy	Cylindrical	14500	NMC/C	0.8 Ah	Emmerich	unknown
4	High Energy	Cylindrical	18650	LCO/C	2.6 Ah	Samsung	unknown
5	High Energy	Cylindrical	18650	unknown	3.5 Ah	Sanyo/ Panasonic	unknown
6	High Power	Prismatic	Industrial	unknown	5 Ah	Industry	unknown
7	High Energy	EL-Cell®	3-Electrode Set-Up	NMC/C	0.005 Ah	BLB	2.55 cm^2

Table 3.1.: Characteristics of the investigated LIBs.

[2] Battery LabFactory

3.2.2. Measurements

Dynamic measurements are performed in galvanostatic mode with a Zahner Electrochemical Workstation (Zennium) in a climate chamber at an environmental temperature of 25°C and 50% SoC, if not further declared. The SoC is set by charging the cell with 1 C CC/CV with CV until the current decreased to C/20. Afterwards, the cell is discharged with 0.5 C CC to 50% SoC. Cycling tests are conducted using a MACCOR Battery Test System (Model 4200). In Table 3.2, the measurement specifications and conditions of NFRA and EIS are listed. As explained in Section 1.5.1, multiple data evaluation types of NFRA have been investigated in the course of this work. In this chapter, the square root of the sum of squared amplitudes of higher harmonics and the amplitudes of individual higher harmonics Y_n with $n \geq 2$ are analysed with NFRA.

Measurement Conditions

State-of-Charge

NFRA is measured at various SoC on a cylindrical 18650 cell (type 5). For each NFRA

Parameters	NFRA	EIS
I_{AC}	1.5 to 2 C	0.05 C
ω-range	0.02 Hz to 10^4 Hz	0.02 Hz to 10^6 Hz
n_p for $\omega < 66$ Hz	5	10
n_p for $\omega > 66$ Hz	5	10
SoC	50%	50%

Table 3.2.: Measurement parameters of NFRA and EIS.

measurement, the SoC is set according to the protocol described at the beginning of this section. The cell is discharged with 0.5 C CC to the particular SoC. The SoC is varied in the range from 20% to 90% in 10% steps.

Temperature Distribution

The impact of a homogeneous and a heterogeneous temperature distribution, T_{homo} and T_{het} respectively, on NFRA is analysed on a one-layered pouch cell (type 1) with a surface of 25 cm^2. NFRA is measured at T_{homo}=25°C as well as at 30°C in a climate chamber. To guarantee a homogeneous temperature, the cell is conditioned in the climate chamber for 24 hours. Further, a defined part of the cell of 1.13 cm^2 is heated to 30°C using a cartridge heater. Thereby, a heterogeneous temperature distribution T_{het} is generated. The experimental set-up is positioned in the climate chamber which is set to a constant environmental temperature of 25°C. The temperature distribution is observed using the infrared thermographic camera FLIR SC325 with an measurement accuracy of $\pm 2°C$ or $\pm 2\%$ of reading. The position of the heater cartridge is set to the middle of the cell surface.

As explained in Chapter 2, the standard measurement protocol of EIS starts at a medium frequency, runs upwards to measure voltage responses at higher frequencies and then turns to measure the lower limit of the frequency range. For the impedance measurements discussed in this section, the sweep direction was changed accidentally. Thus, the impedances at lower frequencies were measured twice instead of the impedances at higher frequencies. In case of EIS at T_{homo}=25°C, therefore two impedance curves are visible. Impedances in the low freq range do not match at three measurement points (Figure 3.3). This mismatch is an indicator for a temporarily state drift away from the equilibrium. An irreversible state drift can be excluded, as the measurement data overlap at the other frequencies. Such a temporarily drift

may be caused, if the temperature in the climate chamber changed for a short time, i.e. by temporary opening of the climate chamber. A quantitative comparison of absolute impedances is therefore not possible for this study. However, the focus here is set to the analysis of the qualitative impact of different temperature distributions on NFRA. The significance of such an analysis is not affected by a temporarily state drift.

Measurement Parameters

Excitation Amplitude of I_{AC}

The excitation amplitude of I_{AC} is varied for measurements on a cylindrical 14500 cell (type 3) in the range from 0.2 A to 5 A. The excitation amplitudes and the corresponding C-rates are listed in Table 3.3. The OCV of the cell is is monitored prior to and after NFRA measurement. The waiting time between NFRA and OCV measurement was at least one hour to guarantee an equilibrium state of the cell.

I_{AC} / A	C-rate / -
0.2	0.40
0.5	0.63
1	1.25
2	2.5
5	6.25

Table 3.3.: Evaluated excitation amplitudes of I_{AC} and corresponding C-rates.

Number of Oscillations

Next, the oscillations ν_i and the number of oscillations n_ν are varied for NFRA on a cylindrical 14500 cell (type 3). The measurement parameters are given in Table 3.4. NFR are averaged by the potentiostat over n_ν.

ν_i	n_ν
1	1
1 to 2	2
1 to 5	5
1 to 10	10

Table 3.4.: Evaluated oscillations of NFRA.

Data Point Density

The impact of the data points per frequency decade n_p on NFRA is analysed for measurements on a cylindrical 14500 cell (type 3). NFRA is measured with five, ten and fifteen n_p.

Reproducibility Analysis

For reproducibility analysis, NFRA is measured three times with identical Zahner settings and measurement conditions on a cylindrical 14500 and 18650 cell (type 3 and type 4). The SoC of 50% is set again before each measurement by charging the cell with 1 C CC/CV with CV until the current is decreased to C/20. Then, the cell is discharged with 0.5 C CC to SoC 50%.

Cell Type and Design

In a last step, NFRA on different cell types is analysed. In Table 3.1, cell specifications are given. NFRA is measured with a high excitation amplitude of at least 1.5 C to 2 C, in dependence of the particular cell capacity, as it is only possible to chose discrete excitation amplitudes of I_{AC} due to the restricted AC settings of the Zahner-elektrik potentiostat.

3.3. Results and Discussion

3.3.1. Measurement Conditions

In this section, the impact of measurement conditions, namely SoC and temperature, is analysed. The impact of decreasing temperature on NFRA already was demonstrated in Chapter 2. In this chapter, the focus is on the impact of an increasing temperature and temperature distributions.

State-of-Charge

A variation of the SoC was performed on a cylindrical 18650 cell (type 5). In Figure 3.1, NFR spectra for a variation of the SoC are shown. The sensitive frequency

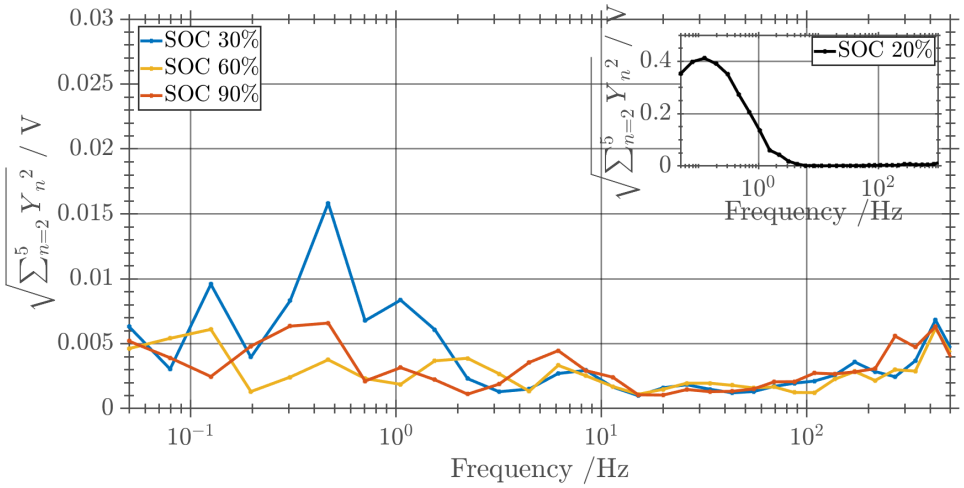

Figure 3.1.: NFR measured at 30%, 60%, 80% and 90% SoC and in the inlet at SoC 20% SoC.

range is 0.02 Hz to approximately 10 Hz. These frequencies correlate to diffusion and electrochemical reactions, as discussed in Chapter 2. At higher frequencies than 10 Hz, NFR are independent of the SoC. NFR are highest for low and high SoCs. NFR measured at SoC of 20% are one order of magnitude higher than at SoC 30%-90%, respectively. The corresponding spectrum is shown in the inlet in Figure 3.1. At a medium SoC of 60%, NFR have the lowest amplitudes. In Figure 3.2, NFR extracted at 1 Hz are shown in dependence of the SoC. It well illustrates that NFR are minimum at a medium SoC of 60% as well as maximum at 20% and 90% SoC. This can be physically explained by the exchange current density and the slope of the OCV curve. The exchange current density is thereby highly sensitive to the strong relative concentration changes at SoC limits (20%, 90%) as the electrodes are fully intercalated with lithium-ions, respectively fully deintercalated. Thus, NFR are higher at low and high

SoCs compared to medium SoCs. Further, the discharge curve of the cell is shown in the inlet in Figure 3.2 which is measured with a low current of 0.1 C to minimize cell polarization processes. Thereby, it is a measure for the OCV curve. The slope of the curve is greatest at low SoCs. Thus, a greater potential range is accessed for a given current and ΔSoC. As a result, NFR have the highest amplitudes at the lowest SoC.

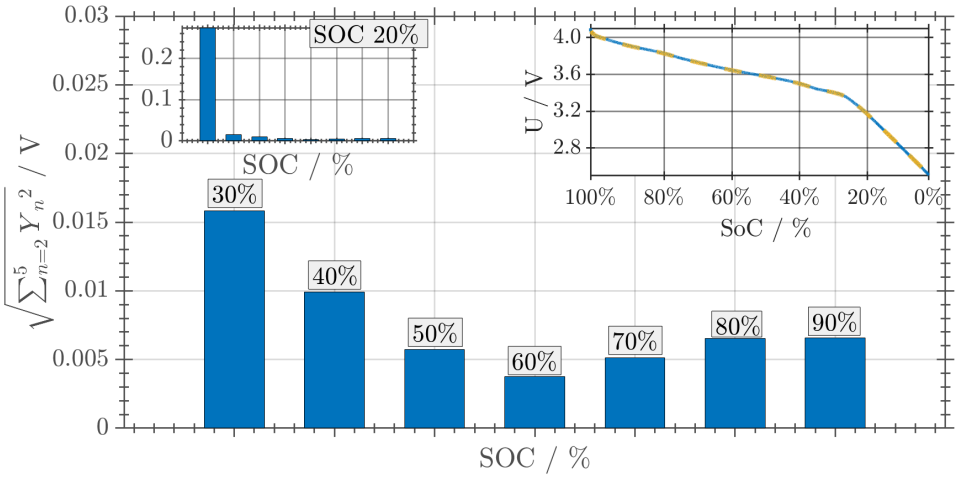

Figure 3.2.: NFR measured at different SoC extracted at 1 Hz, and in the inlet on the top right the discharge curves of two cells (blue curve and dashed yellow curve) from 2.5 to 4.1 V.

Generally, it can be stated that NFR depend on the SoC of the cell. For high and low SoCs, NFR have maximum values. For a precise and reliable application of NFRA, the SoC has to be set accurately and remain constant during analysis.

Temperature Distribution

In Chapter 2, the study for decreasing environmental temperature demonstrated that nonlinearities measured in the frequency range characteristic for diffusion and electrochemical reactions are temperature dependent. In the following, this study is extended by analysing the impact of homogeneous and heterogeneous temperature distributions, T_{homo} and T_{het}.

In Figure 3.3A, NFR spectra of a one-layered pouch cell (type 1) are shown over frequency at T_{homo}=25°C and at T_{homo}=30°C as well as with a heterogeneous distribution T_{het} induced at an ambient temperature of 25°C. This case is further referred to as T_{het}=25°C. Additionally, in Figure 3.3B, the corresponding impedance spectra are given. The frequency range that is sensitive to NFRA includes frequencies from 0.02 Hz to 25 Hz for all temperature variations and corresponds to electrochemical and diffusion processes of the cell, as presented in Chapter 2. At 1 Hz, NFR have a

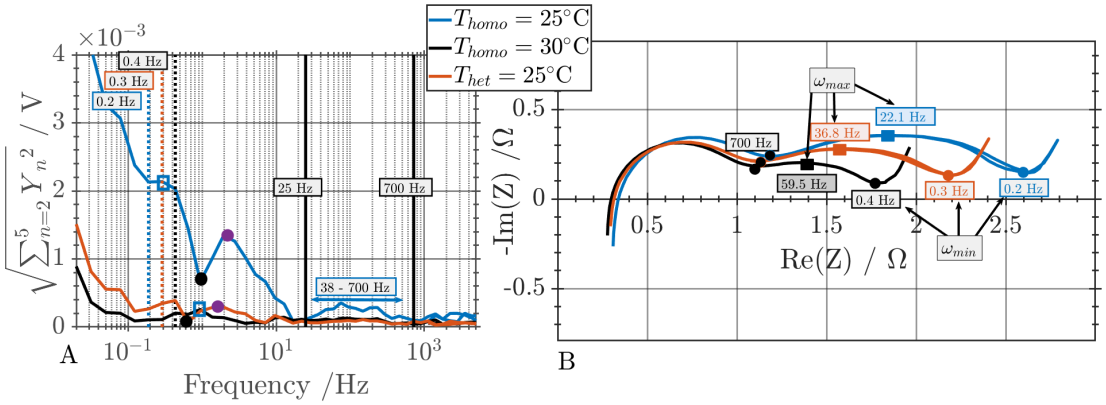

Figure 3.3.: (A) NFR spectra and (B) the corresponding impedance spectra measured at T_{homo}=25°C, T_{homo}=30°C and T_{het}=25°C. The colored dots mark characteristic frequencies that shift with the temperature.

local minimum at T_{homo}=25°C. As well, at T_{homo}=25°C, NFR are excited in a broad frequency range from 25 Hz to 700 Hz. Therefore, three characteristic frequency ranges are identified between 0.02 mHz and 700 Hz at T_{homo}=25°C. The lowest frequency range corresponds to the diffusion process. Two further ranges with distinct excitation of NFR may indicate electrochemical reactions of anode, respectively cathode. However, NFR are only minor with constant values in the magnitude of 10^{-4} V to 10^{-5} V between 25 Hz and 700 Hz at T_{homo}=30°C and at T_{het}=25°C. At the higher limit of the frequency range at approximately 700 Hz reaction processes are typically not excited. However, limitations of the ionic transport between the SEI and electrolyte are temperature dependent, as well, and may cause NFR with small amplitudes. At the lower limit of this range, a reaction process may be excited. Decreasing NFR with increasing temperature may indicate decreased limitations of the reaction kinetics. Impedance analysis supports the process identification with NFRA. The frequency range from 0.02 Hz to approximately 700 Hz in the impedance spectra shown in Figure 3.3 corresponds to the lower frequency semi-circle which is characteristic for electrochemical reactions and below 0.5 Hz to the Warburg impedance which is characteristic for diffusion processes. The impedances of the measurement at T_{het}=25°C are smaller than the impedances at T_{homo}=25°C and higher than the ones at T_{homo}=30°C. If a heterogeneous temperature increase is generated, the cell temperature T_{cell} is higher at the source of the temperature distribution and decreases towards the cell edges. As NFR and impedances of T_{het}=25°C are in between NFR and impedances that are excited at 25°C and 30°C, it can be deduced that the average cell temperature for the measurement at T_{het} is in between 25°C and 30°C. As elec-

trochemical kinetics decrease with the temperature, cell overpotentials increase for a given current. Therefore, NFR decrease for increasing temperatures, as observed in the presented study.

A slight shift of characteristic time constants in dependence of the temperature is observed for EIS and NFRA. The frequency ω_{min} between the semi-circle at lower frequency and the Warburg impedance shifts from 0.2 Hz to 0.4 Hz with increasing temperature. The frequency ω_{max} of the lower frequency semi-circle shifts slightly towards higher frequencies, namely from 22.1 Hz to 59.5 Hz. This correlates to the Arrhenius equation (Equation 2.1). The reaction rate constant increases with the temperature which results in an acceleration of the corresponding cell processes. Thereby, characteristic time constants will be at higher frequencies. The minimum of the impedance between the semi-circles is not affected by temperature and stays constant at 700 Hz. Concerning NFRA, shown in Figure 3.3B, maxima and minima of NFR which correlate to specific processes cannot be assigned for the analysed cell. A slight shift of the minimum at 1 Hz and the maximum at 2 Hz at T_{homo}=25°C towards lower frequencies is observed for a heterogeneous temperature distribution. Most likely, this peak shifting may occur as a consequence of the temperature gradient of the cell. Thereby, a reaction process is excited at different time constants in dependence of the local temperature. The ionic transport limitations are temperature dependent, as well. Thus, all cell processes will be excited in a broader frequency range as they may overlap stronger compared to a homogeneous temperature distribution. For T_{homo}=30°C, a slight maximum of NFR is observed at 0.9 Hz. This maximum may correspond to cell processes which are excited at approximately 0.3 Hz at T_{homo}=25°C as they show decreased reaction kinetics due to the higher temperature and are therefore at a higher time constant.

Concluding, the cell temperature has to be adjusted and monitored accurately for reliable studies with NFRA. A heterogeneous temperature distribution does not excite novel dynamic characteristics in NFRA, moreover it impacts the overall frequency range.

3.3.2. Measurement Parameters

Multiple measurement parameters can be set at the device that may have an impact on NFRA. The impact of a) the excitation amplitude of I_{AC}, b) the number of oscillations n_ν and c) the data points per decade n_p are analysed. A reproducibility analysis

of NFRA is investigated at the beginning of this section to demonstrate that it is possible to measure NFRA reproducibly.

Reproducibility Analysis

Reproducibility of NFRA is analysed with repeated measurements on a cylindrical 14500 and a 18650 cell (type 3 and 4). Equal measurement parameters and conditions are set for all NFRA measurements. NFR of three measurements are averaged at

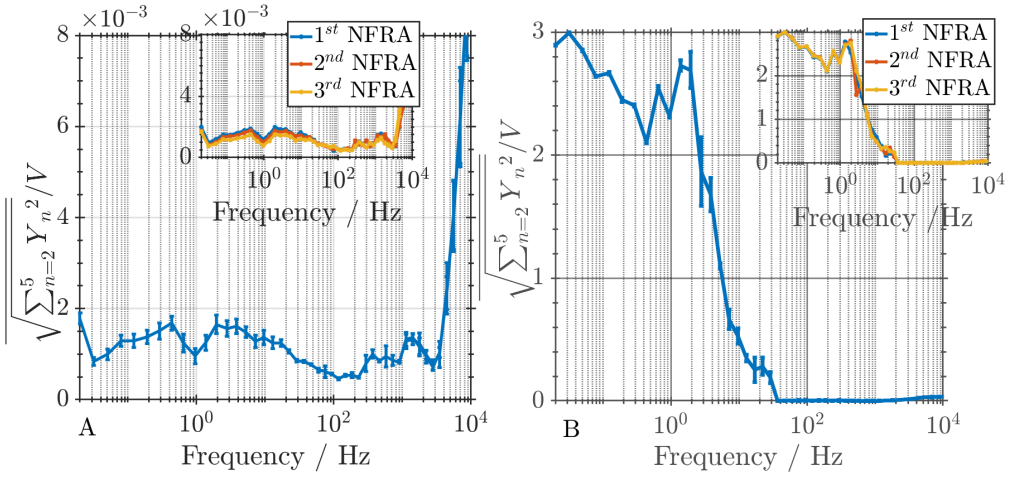

Figure 3.4.: The mean of NFR with the standard deviation and NFR of the repeated measurements in the inlet for A) cell type 3 and B) cell type 4 at 25°C and 50% SoC.

each measured frequency, and the corresponding standard deviation from the mean of NFR is calculated. In Figure 3.4A and B, those values are shown over frequency for the 14500 cell and the 18650 cell, respectively. In the inlet, the corresponding single NFR spectra are shown. Due to different cell chemistry, NFR of the cells have different progressions, magnitudes and slopes. Generally, the sensitivity of NFRA depends on the frequency and cell chemistry which might cause different errorbars, as well.[3] For example, the 18650 cell has a smaller standard deviation over a wide frequency range than the 14500 cell. However, for both cells, a good reproducibility is given. If cell processes are quantitatively analysed with NFRA, the standard deviation should be known and included in the analysis.

Excitation Amplitude of I_{AC}

A quasi steady-state of the cell during the measurement is needed for a qualitative and quantitative process identification and interpretation. For NFRA, an AC with a high excitation amplitude is needed, as in-depth described in Chapter 2. However, the

[3]The impact of the cell type and the cell design on NFRA is discussed in-depth in Section 3.3.3.

excitation with a high amplitude may have an impact on the equilibrium state of the cell, especially at measurement frequencies in the mHz range. This impact is analysed in the following. Therefore, the OCV before and after NFRA is measured and correlated to the excitation amplitude [81]. The study is performed on a cylindrical 14500 cell (type 3) in the frequency range from 0.02 Hz to 10 kHz. NFR spectra are shown in Figure 3.5A for different I_{AC} ranging from 0.3 C to 2.5 C and additionally in Figure 3.5B for I_{AC}=6.3 C.

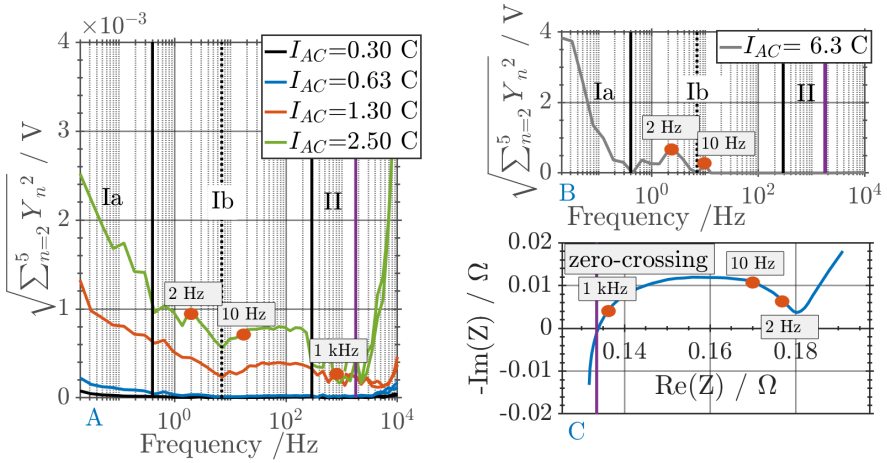

Figure 3.5.: (A) NFR spectra with a variation of the excitation amplitude of I_{AC} from 0.3 C to 2.5 C, (B) NFR with I_{AC}=6.3 C and (C) the corresponding impedance spectrum measured with C/15. The red dots mark the characteristic frequencies 2 Hz, 10 Hz and 1 kHz.

As discussed in Chapter 2, three characteristic frequency ranges for processes are typically identified in NFR spectra. Specifically for the cell analysed in this section, it may be possible to distinguish between the electrochemical reactions and to subdivide frequency range Ib in two further regions. Each range may correspond to one electrochemical reactions. However, it is not possible to state which frequency range belongs to the anode or the cathode. Characteristic frequency ranges and correlated processes are given in Table 3.5. In the corresponding impedance spectrum in Figure 3.5C, only one arc is visible which may contain several semi-circles. It can be postulated that time constants of the electrochemical reactions and the ionic transport processes between the SEI and electrolyte overlap.

By increasing I_{AC}, NFR increase in the frequency range characteristic for diffusion and electrochemical reactions (range I). In contrast to the cells priorly discussed, NFR that are excited in frequency range II depend on the amplitude of I_{AC}, as well, especially for an excitation amplitude greater than 1.3 C. However, electrochemical reactions are typically not excited at such high frequencies [35]. Most probably, those

Range	ω-range / Hz	Process	ω
Ia	0.02 to 0.4	Diffusion	-
Ib	0.4 to 7	Electrochemical reaction I	2 Hz
Ib	7 to 290	Electrochemical reaction II	10 Hz
II	290 to 1800	Ionic transport at interfaces	1 kHz

Table 3.5.: Characteristic frequencies and processes identified with NFRA.

responses are caused by the mutual inductance of wires and clamps of the potentiostat as well as metal parts of the electrodes. As explained in Chapter 2, the high frequency part of NFRA and EIS is measured by default twice by the potentiostat, and thus two curves are observed in this frequency range.

Next, NFR at specific frequencies of 2 Hz, 10 Hz and 1 kHz are evaluated in detail for the variation of I_{AC}. In Figure 3.6, NFR at these frequencies are shown in dependence of I_{AC}. With increasing I_{AC}, NFR increase. Up to 2.5 C, NFR increase uniformly at

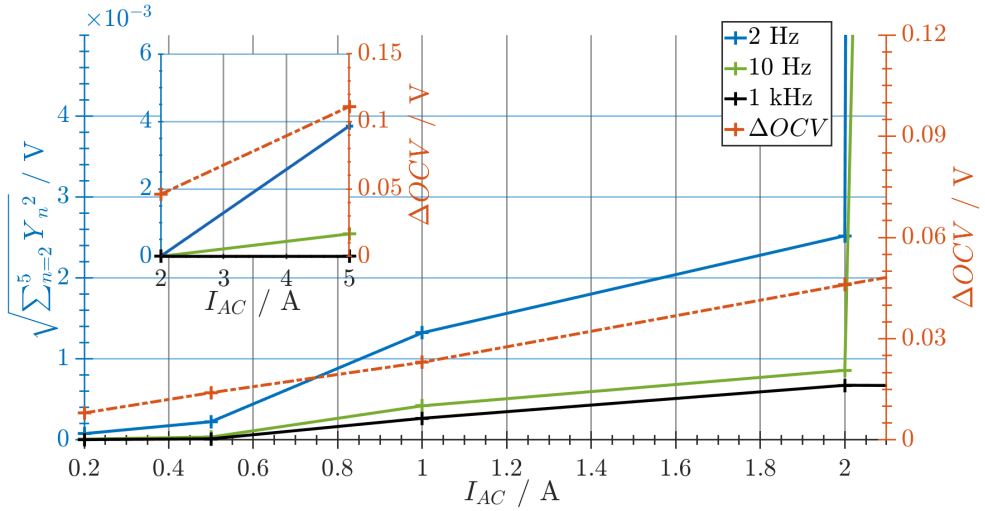

Figure 3.6.: NFR at characteristic frequencies and ΔOCV of the cell in dependence of I_{AC}.

the characteristic frequencies. If I_{AC} is increased to 6.3 C, NFR at 2 Hz and 10 Hz increase strongly to approximately 0.1 V, respectively 0.02 V. NFR at 1 kHz, however, almost stay constant. It can be assumed that in range Ib electrochemical reactions with a strongly nonlinear reaction kinetic are excited. Further, reaction processes at 2 Hz and 10 Hz may have different reaction kinetics due to the higher amplitude dependency of NFR at 2 Hz. Range II most probably does not contain processes following a Butler-Volmer relation even though an amplitude dependent NFR increase

is observed, as electrochemical reactions typically do not have time constants at frequencies in the kHz-range.

Further, the difference of the OCV before and after measurement (ΔOCV) of NFRA at each amplitude of I_{AC} is shown in Figure 3.6 to analyse if a change of the cell state was induced by the measurement. Increasing the amplitude of I_{AC} increases ΔOCV of the cell during NFRA, as illustrated in Figure 3.6. From 0.3 C to 6.3 C, ΔOCV increases from 8 mV to 120 mV for measurements until a minimum frequency of 0.02 Hz. If a cell is excited with an AC with a high amplitude, the internal cell temperature increases [82, 83]. Generally, heat generation is higher for higher excitation amplitudes and, as well, at lower minimum measurement frequencies due to the longer measurement time per oscillation, i.e. a higher overall amount of charge transferred per oscillation [83]. Thus, the OCV of the cell will change as cell polarization processes influencing the OCV are highly sensitive to the temperature [81]. However, an ΔOCV of 120 mV observed for an excitation current of 6.3 C is rather high and most probably not only caused by internal heating due to the high excitation amplitude. For example, temperature variations typically cause ΔOCV changes in the decimal mV range, in dependence of the chemistry, design and manufacturing quality of the cell as well as ΔT [84, 85]. Possibly, the cell may age due to the high current, e.g. lithium plating or accelerated electrode or electrolyte degradation may be induced.

Concluding, the amplitude of I_{AC} has to be as high as necessary to excite distinct NFR, and as low as possible to minimize temperature changes and thus changes of the quasi steady-state. If low frequencies are measured, ΔOCV during NFRA increases which may be harmful for the cell at high and low SoCs. Steady-state changes are negligible for NFRA measurements with a minimum frequency of 1 Hz due to short measurement times of only 1 s per oscillation.

Oscillation Analysis

If an electrochemical system is excited with a sinusoidal current, it reaches for a new steady-state [70]. A sinusoidal current with a small amplitude of I_{AC}, as used in EIS, does not change the steady-state. However, if a sinusoidal current with a high amplitude is used, the steady-state of the cell may be effected. Cell processes with a small time constant will reach a new steady-state faster than processes with a high time constant [70].

A variation of the number of evaluated oscillations n_ν of the sinusoidal excitation amplitude is performed on a cylindrical 14500 cell (type 3), and its impact on NFR spectra is analysed in this section. A higher n_ν is automatically coupled to an extension of the measurement time of NFRA and EIS. In Figure 3.7, NFR spectra excited with I_{AC}=2.5 C are shown for a variation of the oscillation number n_ν. NFR in the low-frequency region of Ib from approximately 0.2 Hz to 30 Hz are significantly influenced by the number of oscillations. If only the first oscillation is measured, the

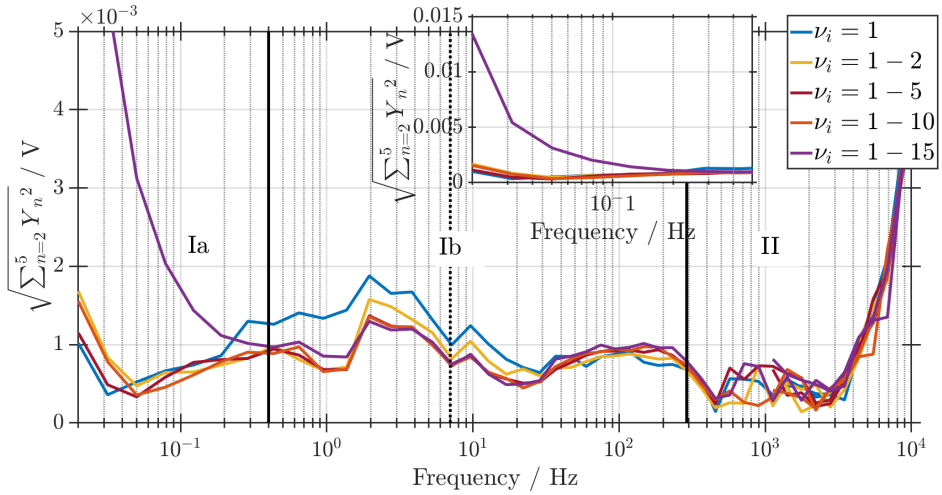

Figure 3.7.: NFR spectra averaged with different numbers of oscillations n_ν.

amplitudes of NFR have the highest intensity. NFR decrease, if it is averaged over two or three oscillations. Applying five and more oscillations, NFR do not decrease further. Thereby, it can be stated that at least five oscillations have to be applied to reach a steady-state in the lower frequent region of Ib. The electrochemical reaction at the higher frequency limit of Ib and ionic transport processes between the SEI and electrolyte in range II have smaller time constants and are therefore already in a steady-state and not influenced by the oscillation number. In frequency range Ia, NFR and n_ν do not correlate. Up to the the tenth oscillation, no distinct relation to NFRA is identified. However, if fifteen oscillations are applied, NFR increase strongly in range Ia, shown in the inlet in Figure 3.7. On the one hand, this increase may indicate that

the steady-state changes, possibly due to internal cell heating caused by the extended measurement time, as discussed in Section 3.3.2. On the other hand, possibly, the cell may age for n_v>10 as a consequence of internal heating due to the high current amplitude, as discussed in the previous section.

Concluding, averaging NFR over five oscillations is sufficient for steady-state analysis with NFRA in the overall frequency range. Further, cell processes with a small time constant are less impacted by the number of oscillations of the excitation signal than processes with a high time constant.

Data Point Density

Measurement time of dynamic analysis is significantly influenced by the data points measured per frequency decade n_p. For optimization of measurement time without a deterioration of the accuracy of the measurement signal, n_p of NFRA measurements are varied and the impact on NFRA of a cylindrical 14500 cell (type 3) is analysed.

In Figure 3.8A, NFR spectra with five, ten and fifteen n_p are shown over the frequency. The frequency ranges Ia and Ib are influenced by the variation of n_p. For higher fre-

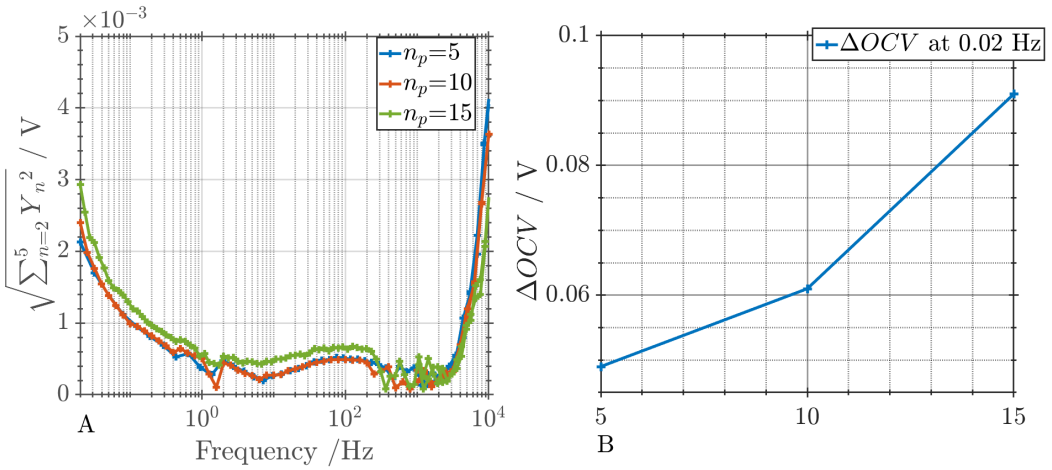

Figure 3.8.: (A) NFR spectra measured with different n_p and (B) ΔOCV of the cell in dependence of n_p.

quencies than 290 Hz, no correlation between NFR and n_p is noticed. NFR spectra that are measured with five and ten n_p are identical. The spectrum measured with fifteen data points per frequency decade shows higher NFR than the ones measured with five and ten data points per decade. In Figure 3.8B, ΔOCV of the cell during NFRA is shown in dependence of n_p. ΔOCV increases with the data points per decade. The higher n_p, the longer is the measurement time and therefore the overall amount of charge transferred during measurement. Thus, the presumed impact of internal

heating due to the accumulated measurement time may increase, as discussed in the previous sections. As a result, the cell may be driven away from its equilibrium state during the measurement. Temperature dependent changes of the OCV typically are in the decimal mV range. At 15 n_p, ΔOCV is almost 100 mV which possibly also could indicate that the cell ages under this test parameters, as explained previously. Thus, NFR measured with fifteen data points per frequency decade may have higher amplitudes, as well. Concluding, the number of data points has to be chosen as high as necessary, but as low as possible. Five or ten data points per frequency decade are recommended for NFRA measurements.

3.3.3. Cell Type and Design

In a last step, NFRA is conducted on different cell types and designs of LIBs and measured nonlinear frequency responses are compared. In Figure 3.9A to F, Y_2 and Y_3 of a one-layered pouch cell with a capacity of 0.03 Ah (type 1), a multi-layered pouch cell with 9 Ah (type 2), a cylindrical 14500 cell with 0.8 Ah (type 3), a cylindrical 18650 cell with 2.6 Ah (type 4), a prismatic cell with 5 Ah (type 6) and an EL-Cell®[4] with 0.005 Ah (type 7) are shown. For each cell, the second harmonic Y_2 and the third Y_3 harmonic are analysed as well as the corresponding impedance spectrum. Typically, impedances are normalized to the surface area of the electrodes for a surface-independent, quantitative impedance analysis. For the commercial cylindrical cells and for the industrial prismatic cell the electrode dimensions cannot be obtained. Further, the amount of electrode layers of the prismatic cell is unknown. Therefore, the surface area cannot be calculated for cell types 3, 4 and 6. Thus, absolute impedance values are shown in the corresponding spectra instead of normalized impedances. However, as the capacity of the cells differs over several magnitudes from mAh to Ah, and except cell F only high-energy cells are evaluated here, it is assumed that the surface area is higher for the cells with higher cell capacity. Due to the mentioned reasons, a surface-independent, quantitative impedance analysis cannot be done in this section.

Specific information about characteristics of the particular cell can be deduced with NFRA. To support interpretation of NFRA, the impedance spectra of the cells are shown in Figure 3.10A to F. The frequency of the characteristic maximum ω_{max} is

[4] With the electrochemical equipment of the company EL-Cell® the characterization of battery cells in the three-electrode format is possible. The test cell typically are referred to as "EL-Cell®".

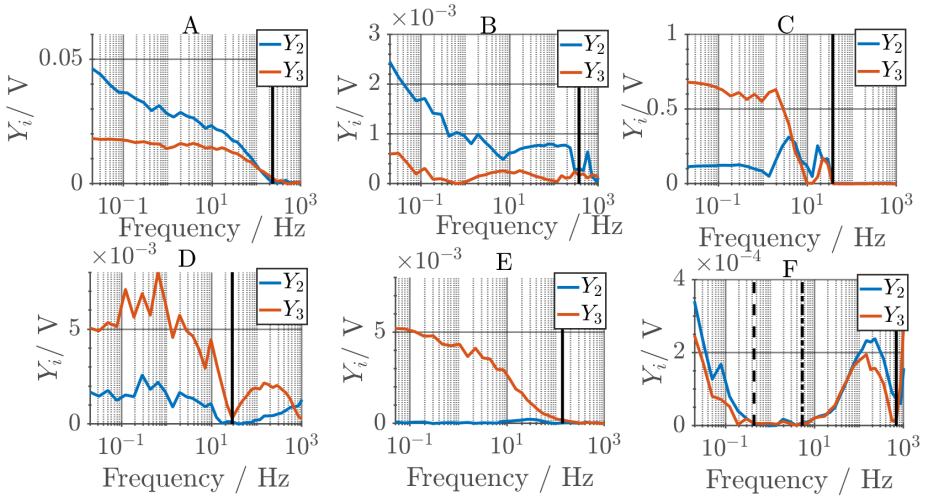

Figure 3.9.: Y_2 and Y_3 of different cell types and designs: (A) one-layered pouch cell, (B) cylindrical cell with 0.8 Ah, (C) cylindrical cell with 2.6 Ah, (D) multi-layered pouch cell with 9 Ah, (E) an EL-Cell® with 0.005 Ah, (F) prismatic cell with 5 Ah.

marked in each impedance spectrum. In the impedance spectra, mostly one semicircle is visible. Thus, the characteristic time constants of the electrochemical reactions and the ionic transport between SEI and electrolyte overlap. Therefore, processes cannot be separated analysing only EIS. With NFRA, however, these processes are separable as the electrochemical reactions show distinct higher harmonic voltages whereas the ionic transport between SEI and electrolyte does not, as in-depth analysed in Chapter 2.

Next, NFRA and EIS of the cells are analysed. First, it can be stated that depending on the cell, Y_2 and Y_3 have different intensities and progressions. Further, the magnitude of the higher harmonic voltages and the frequency range which is sensitive to NFRA, differs. For the cells shown in Figure 3.9A to E, the sensitive frequency range is in the low- to mid-frequency range. The black line in each spectrum marks the upper limit of the sensitive frequency range in which distinct higher harmonic voltages are excited. This mark is at the lowest frequency for cell type 4 and at the highest frequency for cell B. For the prismatic cell in Figure 3.9F, the sensitive frequency range is at low frequencies from 0.02 Hz to 0.4 Hz and as well from 17 Hz to 550 kHz. In between, from 0.4 Hz to 550 Hz, higher harmonic voltages are significantly lower and almost constant with a magnitude of 10^{-6} V. This indicates that in this frequency range only minor nonlinearities are excited on this LIB. For the other cells, a rather non-sensitive frequency range with only minor nonlinearities starts at higher frequencies between 10 and 300 Hz, depending on the cell. The sensitive frequency ranges of the cells with the corresponding cell processes are listed in Table 3.6. In Figure 3.9A and 3.10A

Figure 3.9	ω-range / Hz	Process
A	0.02 to 190	Diffusion and electrochemical reactions
B	0.02 to 230	Diffusion and electrochemical reactions
C	0.02 to 17	Diffusion and electrochemical reactions
D	0.02 to 30	Diffusion and electrochemical reactions
E	0.02 to 40	Diffusion and electrochemical reactions
F	0.02 to 0.4 / 17 to 550	Diffusion / Electrochemical reactions

Table 3.6.: Sensitive ω-range of the different cells and the corresponding processes.

as well as in 3.9E and 3.10E, higher harmonics voltages and impedances of the one-layered pouch cell and the cell in the EL-Cell® format are shown. Both cells have small capacities. Due to the thick separator in case of the EL-Cell® and the manual manufacturing in case of the pouch cell, these LIBs have higher impedances than the other cells. Higher harmonic voltage responses, however, are approximately in the same order of magnitude.

The electrodes used for the EL-Cell® were additionally used for the manufacturing of the 15-layered pouch cell, shown in Figure 3.9D and 3.10D. Due to the high cell capacity and the large cell surface, the impedances of the 15-layered pouch cell are significantly smaller. Higher harmonic voltages of both cells are excited at similar frequencies and have the same order of magnitude. Progressions and intensities of Y_2 and Y_3 are similar, as well. The third harmonic Y_3 has higher voltage responses than the second harmonic Y_2.

This study reveals that high energy and high power cells can be distinguished with NFRA. High energy cells have rather slow electrochemical cell processes in comparison to high power cells. Therefore, the sensitive frequency range for nonlinearities may be at lower frequencies for high energy cells than for high power cells, as demonstrated here. The cylindrical 14500 cell has the highest energy density, as the upper limit of the sensitive frequency range is already at 17 Hz, shown in Figure 3.9C and 3.10C. The lower the upper limit of the sensitive frequency range of the electrochem-

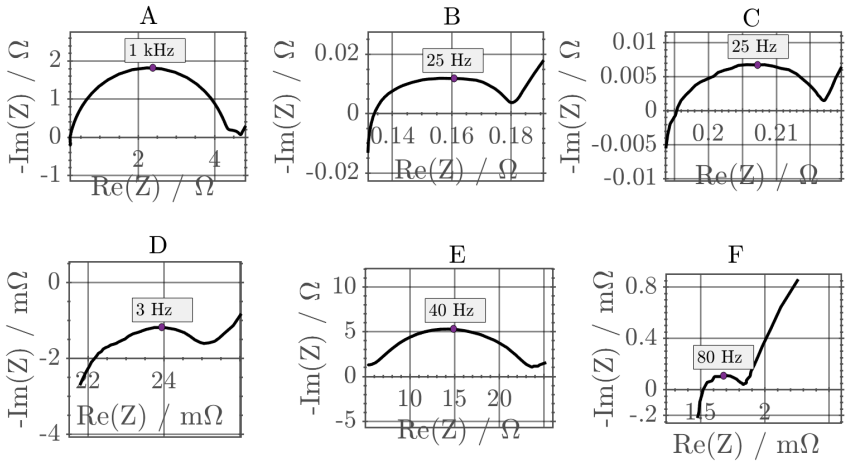

Figure 3.10.: Impedance spectra of different cell types and designs: (A) one-layered pouch cell, (B) cylindrical cell with 0.8 Ah, (C) cylindrical cell with 2.6 Ah, (D) 15-layered pouch cell with 9 Ah, (E) EL-Cell® with 0.005 Ah, (F) prismatic cell with 5 Ah.

ical reactions, the higher may be the energy density. However, this hypothesis has to be investigated, e.g. using model-based analysis in future studies.

In comparison to high power cells, high energy cells typically are not operated at high C-rates and therefore have a higher magnitude of higher harmonic voltage responses than high power cells, if excited with approximately the same C-rate. The high power cell has the lowest higher harmonic voltage responses with a maximum in the magnitude of 10^{-4} V for an excitation with I_{AC}=2 C. This is due to the optimization of higher power cells for operation at high C-rates with only minor performance deterioration. Higher harmonic voltage responses of the high energy cells are at least one order of magnitude higher for excitation with approximately the same amplitude of I_{AC}. The analysis of cell types and designs of LIBs shows that NFRA is sensitive to cell specifications. With NFRA, it is possible to distinguish between high energy and high power cells. The study shows that NFRA enhances process characterization as well as separation of electrochemical reactions and ionic transport processes between SEI and electrolyte, as deeply discussed in Chapter 2. These processes may be distinguishable with NFRA, even if they overlap in the EIS [1]. Further, individual higher harmonics Y_2 and Y_3 can have different progressions and intensities in dependence of the analysed cell. Recently, Wolff et al. published a model-based analysis of progressions and intensities of indiviual higher harmonics Y_2 and Y_3 [70].

3.4. Conclusions

Electrochemical reactions at anode and cathode as well as the ionic transport processes in the electrolyte and the electrodes analysed with NFRA are highly sensitive to the environmental temperature and the SoC. For an increasing measurement temperature, NFR decrease due to decreased kinetic and transport limitations. Heterogeneous and homogeneous temperature distributions affect NFR spectra equally. Novel NFR characteristics are not excited for a cell with a homogeneous temperature distribution. NFR are only affected quantitatively.

The cell potential depends of the lithium concentration in the electrodes [39]. In dependence of the electrode materials and the electrolyte, the slope of the OCV curve may be higher at high and low SoCs which, besides more sensitive reaction kinetics, results in higher NFR at low and high SoCs. If an excitation current of approximately 2 C is used for NFRA, the amount of charge transferred through a positive sine wave at 0.02 Hz correlates to a SoC change of approximately 8%. Therefore, it has to be ensured that the cell is neither significantly overcharged nor discharged by NFRA at high and low SoC to prevent additional aging.

Concerning measurement parameters, the setting of the amplitude of I_{AC}, the number of oscillations n_ν and the data points measured per frequency decade n_p have an impact on NFRA. The amplitude of I_{AC} has to be chosen as high as necessary to excite distinct NFR, but as low as possible to minimize changes of the steady-state during the measurement. ΔOCV increases at higher excitation amplitudes and at lower minimum measurement frequencies due to increased heat generation caused by a higher amount of charge transferred per oscillation. The number of measurement oscillations n_ν may affect NFRA measurements, because slower cell processes take more time and therefore oscillations to reach a steady state, especially at high excitation currents used for NFRA. If n_ν is set too high ($n_\nu > 10$ for the analysed cell), the cell may leave the steady-state at low frequencies. The same effect is observed, if the measurement points per decade of NFRA are too high (n_p >10) for the analysed cell). Thus, the quality of NFRA may be distorted. Generally, high ΔOCV changes >50 mV during measurement may indicate that cell aging is induced by NFRA for the given measurement parameters.

Finally, it was demonstrated that individual higher harmonics Y_2 and Y_3 are highly sensitive to cell type and design and thereby show characteristic progressions. In dependence of the frequency range which is sensitive to NFRA, it is possible to dis-

tinguish between high energy and high power LIB cells. However, this is not possible with EIS. Concluding, measurement parameters and conditions must be adapted precisely and kept constant for reliable and reproducible dynamic analysis with NFRA.

Chapter 4

Aging Identification and Differentiation [1]

4.1. Introduction

Deep understanding of aging processes in LIBs is a prerequisite to optimize operation, safety and cycle life in dependence of the particular cell design. Chapter 4 is focus on the identification and differentiation of aging effects using NFRA. One crucial aging effect at the anode is lithium plating, because it decreases the cells residual capacity drastically and impairs the performance of the cells [17, 86]. As well, plated lithium may be hazardous for the cell life [87], as it can cause internal short circuits due to dendrite growths or external short circuits due to exothermic reactions of detached plated lithium with the electrolyte [26]. The formation of lithium plating is triggered by fast charging rates, high SoC and operation at low environmental temperatures [78, 88, 89]. Lithium is plated at the surface of the anode particles during charging, if the anode potential drops below 0 V vs. Li/Li^{+}. Lithium plating is a self-accelerating aging effect correlated to charging time, as the anode potential decreases continuously with the amount of plated lithium. During plating, a part of the reduction current leads to the formation of metallic lithium at the anode instead of the intercalation of lithium-ions in the host structure of the anode, usually graphite [29]. Plated lithium can be considered as a further interphase between the anode and the electrolyte in addition to the SEI. It is differentiated between reversible and irreversible plated lithium [29]. Lithum plating can have different morphologies, as it can be a homogeneous as well as a local or a marginal deposition of lithium [26]. During the discharge process, deposited lithium may oxidise again, called lithium stripping.

[1] Parts of this chapter have been published in [2].

Plated lithium can also lose the electrical contact with the anode and detach into the electrolyte. This process is considered as irreversible plated lithium. Metallic lithium can react with the electrolyte to form SEI components, resulting in the growth of the SEI and as such cause further irreversible loss of capacity. Additionally, as the SEI growths, porosity of the anode decreases [90].

Lithium plating is detectable with ex-situ and in-situ methods [29, 91]. Concerning ex-situ methods, which require complete disassembling of the cells, among others optical microscopy with a Scanning Electron Microscope (SEM) and a Transmission Electron Microscope (TEM), neutron diffraction and Nuclear Magnetic Resonance (NMR) spectroscopy are suitable detection methods [29]. Optical in-situ characterization is applicable, too [92]. However, in situ SEM and TEM were not successful for lithium plating on graphite anodes and cells with standard organic electrolytes [29]. Electrochemical in-situ, non-destructive techniques for analysis of lithium plating are for example determining the coulombic efficiency with a coulomb-meter with sufficiently precise resolution [93]. Further, lithium stripping can be used especially for the analysis and quantification of the reversible amount of lithium plating [89]. After plating of the anode, a voltage plateau is observed at high voltages, which is caused by oxidation of plated lithium [28, 89]. Methods correlating the OCV [94] as well as the derivative of the OCV, namely DVA [21, 89], are proposed for detection of lithium plating, as well.

Generally, a battery management system would benefit from a non destructive measurement technology to detect aging effects and therefore determine the SoH. In the literature suggested diagnosis methods are the already mentioned DVA [95], ICA [31, 96], Capacity Differential Analysis (CDA) [97] as well as EIS [28, 33]. The drawbacks of DVA and ICA are that discharge curves with small currents are required for SoH diagnosis to guarantee an equilibrium state of the cells. For EIS, the LIB has to be in an equilibrium state, as well. Further, an application in the overall frequency range from mHz to kHz is time-consuming [33].

In this chapter, dynamic analysis with NFRA is used to evaluate its potential to detect lithium plating. The investigated cells were aged by cycling at -10°C to provoke deposition of lithium on the metal anode. In defined cycling steps, dynamic analysis was performed. NFRA results are compared to the impedance results as well as to the dynamic results of an aging procedure at 25°C on a comparable cell. The degradation of the electrodes was analysed with a microscope in an ex-situ analysis and correlated to the characteristic dynamic response with NFRA.

4.2. Experimental

4.2.1. Cells

Four LIBs in the pouch cell format were tested for the aging studies. As cathode material, NMC with the stochiometry 1:1:1 and as anode material graphite were used. The solvent was a mixture of EC/DEC with a ratio of 3:7 with 1 M $LiPF_6$ as conducting salt. The separator was obtained from Celgard. The electrochemical inactive components are PVDF as binder and CB as conducting additive. The electrodes were manufactured by the BLB. Characteristic cell parameters of the investigated cells are listed in Table 4.2. Cells A to C are used for the aging studies at -10°C. The performance parameters, initial capacity C_0 and initial internal resistance R_0, are listed in Table 4.1. Cell D is a reference cell with almost identical specifications which was investigated in Chapter 2.

Cell	C_0 **/ mAh**	R_0 **/ Ω**
A	33.6	0.37
B	33.4	0.21
C	33.1	0.17
D	32.9	0.16

Table 4.1.: Performance parameters of the investigated cells.

Cells A to C have a slightly lower amount of inactive compounds than cell D. Further, as the cathode of cell D is 10% calendered, volume fraction of the cathode ε_c of cells A to C is slightly higher. However, the differences of the cell parameters of cell D and the cell parameters of the cells A to C are minor. This is also visible in the capacity; C_0 recorded after formation deviates by only ± 0.5 mAh for all four cells. R_0 of the cells are in the same order of magnitude, but deviate more. As the pouch cells were build by manual assembly, the observed fluctuations in resistance are attributed to the construction of the cells.

Parameters	Cell A	Cell B	Cell C	Cell D
Anode thickness δ_a / µm	45	45	45	44
Cathode thickness δ_c / µm	58	58	58	52
Calendering degree anode Π_a / %	10	10	10	10
Calendering degree cathode Π_c / %	0	0	0	10
Mass fraction anode ζ_a / wt%	0.93	0.93	0.93	0.90
Mass fraction cathode ζ_c / wt%	0.90	0.90	0.90	0.90
Mass fraction inactive compounds anode $\zeta_{add,a}$ / wt%	0.07	0.07	0.07	0.10
Mass fraction inactive compounds cathode $\zeta_{add,c}$ / wt%	0.10	0.10	0.10	0.10
Volume fraction anode ε_a / -	0.59	0.59	0.59	0.58
Volume fraction cathode ε_c / -	0.64	0.64	0.64	0.60
Geometric surface area anode $A_{geo,a}$ / cm^2	30.25	30.25	30.25	30.25
Geometric surface area cathode $A_{geo,c}$ / cm^2	30.25	30.25	30.25	30.25

Table 4.2.: Characteristic cell parameters of the investigated cells.

4.2.2. Measurements

Dynamic electrochemical analysis was performed prior to aging, during aging after defined cycle steps, and after aging, all in galvanostatic mode with a Zahner Electrochemical Workstation (Zennium) in a climate chamber at a constant environmental temperature of 25°C and 50% SoC. For NFRA and EIS, a sinusoidal input current I_{AC} was applied to the battery. Measurement parameters of the dynamic analysis, e.g. range of measured frequency ω and measurement points per decade n_p, are listed in Table 5.8. As explained in Section 1.5.1, multiple data evaluation types of NFRA have been investigated in the course of this work. In this chapter, the sum of the amplitudes of higher harmonic responses and the amplitudes of individual higher harmonics Y_n are analysed with NFRA.

Parameters	**NFRA**	**EIS**
I_{AC}	1.5 C	0.05 C
ω-range	0.02 Hz to 10^4 Hz	0.02 Hz to 10^6 Hz
n_p for $\omega <$ 66 Hz	5	10
n_p for $\omega >$ 66 Hz	5	10
SoC	50%	50%

Table 4.3.: Measurement parameters of the dynamic analysis performed in defined cycling steps.

For NFRA, the amplitudes of individual higher harmonic responses Y_n in the output signal from the Y_2 to Y_{10} as well as measurement noise are recorded. As higher harmonic responses Y_n with n>3 were found to be in the same order of magnitude as measurement noise, only higher harmonics Y_2 and Y_3 are analysed in this study. Impedance spectra are shown in the overall frequency range from 20 mHz up to 1 MHz in the Nyquist-Plot. NFRA is analysed up to 10 kHz.

Cells A to C were aged by cycling at -10°C in the potential window 2.9 to 4.2 V, and the reference cell D was aged by cycling at 25°C in the same potential window using a MACCOR Battery Test System (Model 4200). The cycling protocol was identical for both experiments. Cells were charged with 1 C CC/CV until the current decreased below C/20 in the CV step. The discharging was performed with 1 C CC. The SoC is

set by charging the cell with 1 C CC/CV with CV until the current decreased to C/20. Afterwards, the cell is discharged with 0.5 C CC to 50% SoC. Operating parameters are provided in Table 4.4.

Parameters	Cell A	Cell B	Cell C	Cell D
$T_{cycling}$ / °C	-10	-10	-10	25
$T_{dynamic}$ / °C	25	25	25	25
C-Rate / C	1	1	1	1
Charging	CC/CV	CC/CV	CC/CV	CC/CV
Discharging	CC	CC	CC	CC
$U_{Cut-off}$	4.2/2.9	4.2/2.9	4.2/2.9	4.2/2.9

Table 4.4.: Aging parameters of the aging experiments at -10°C and 25°C.

4.2.3. Ex-Situ Analysis

After aging, the cells were opened at ambient air to analyse the degree of plating, following the method provided in [89]. Anode, cathode and separator were dissembled carefully. Opening a cell which is plated with lithium results in the formation of Li_2CO_3. Metallic lithium is oxidized by oxygen to Li_2O and reacts with air humidity and CO_2 to Li_2CO_3 via LiOH [89]. To attribute the formed Li_2CO_3 to the plated lithium, deep discharging of the cells to 2 V was applied, thereby guaranteeing that the anode is completely delithiated. Li_2CO_3 is a white salt and crystalline at ambient air. It is detected optically with a Keyence VHX-900F digital microscope. Results of the aging experiments at -10°C and 25°C are optically compared.

4.3. Results and Discussion

4.3.1. Characteristic Frequency Regions and Corresponding Processes

In the following, unaged spectra are analysed to set a sound base for the following aging discussion. In Figure 4.1A, NFRA of cell A is shown and in Figure 4.1B the cor-

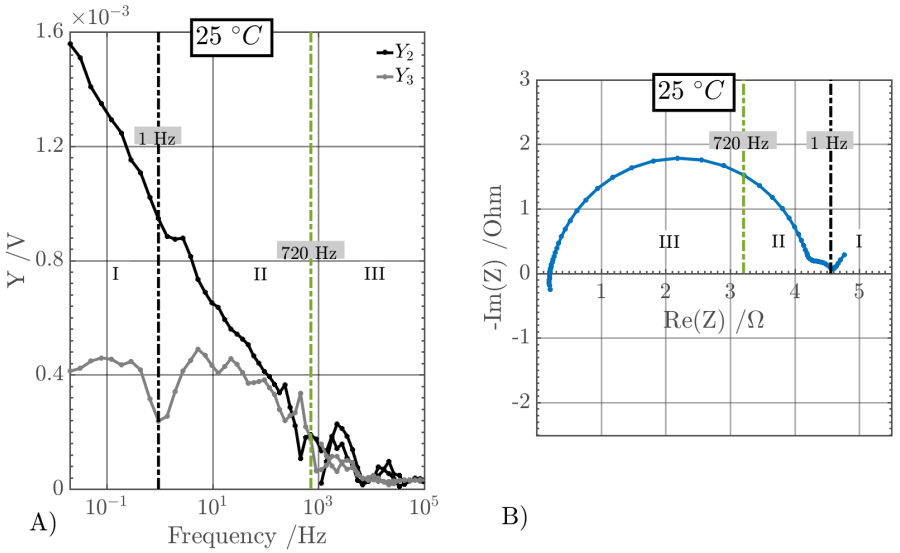

Figure 4.1.: Correlation of (A) NFR spectrum and (B) impedance spectrum of cell A, measured with $I_{AC,NFRA}$=1.5 C and $I_{AC,EIS}$=0.16 C at 25°C for the identification of characteristic frequency ranges prior to aging at -10°C.

responding impedance spectrum is presented. In the higher harmonics spectrum, the second harmonic Y_2 and the third harmonic Y_3 are plotted over frequency. Y_2 has the highest voltage responses at the lowest frequency with maximal values of approximately $1.6{\cdot}10^{-3}$ V. The nonlinear voltage response decreases monotonously with increasing frequency until approximately 720 Hz. For frequencies greater than 720 Hz, the voltage responses of Y_2 and Y_3 are almost constant and fluctuate between 0.1 and $0.2{\cdot}10^{-3}$ V. Y_3 has an almost constant voltage response of approximately $0.4{\cdot}10^{-2}$ V in the range from 20 mHz to 720 Hz, but with a distinct local minimum at 1 Hz, indicating that processes dominating the dynamic behaviour may have changed at this frequency. Therefore, three characteristic frequency ranges for processes are identified with NFRA: range I from 20 mHz to 1 Hz, range II from 1 Hz to 720 Hz and range III is identified for frequencies greater than 720 Hz. Those characteristic frequencies are additionally marked in the corresponding impedance spectrum. Correlation with EIS supports that range I can be assigned mostly to solid diffusion processes. Range II is assigned to the according to Butler-Volmer kinetics strongly nonlinear electrochemical reactions and range III to ionic transport processes, as e.g. migration in and between the SEI and electrolyte [1]. These processes typically show almost only linear behaviour; as can indeed be observed with NFRA in which the higher harmonic voltage responses are negligible. Thereby, range II and III can be distinguished with NFRA, but not with EIS. Based on this correlation of processes to frequency ranges, the impact of aging on the NFRA is analysed.

4.3.2. Dynamic Aging Analysis

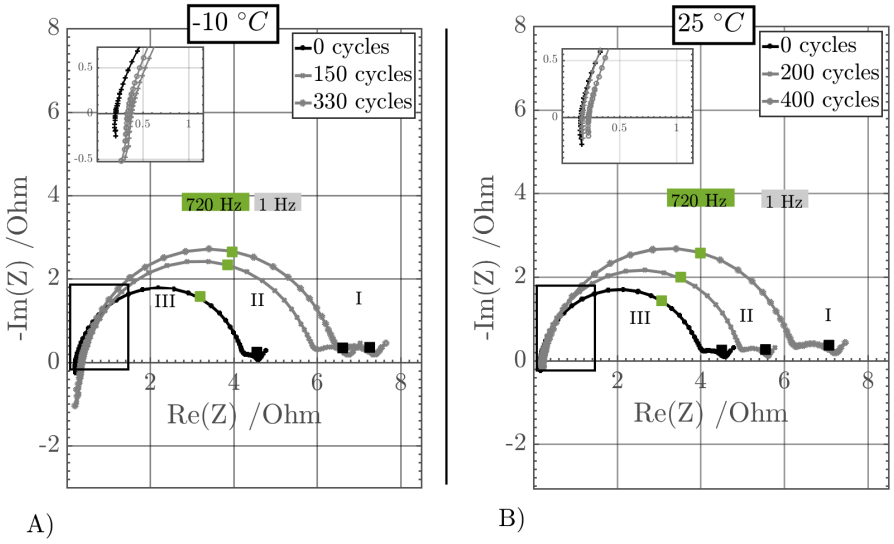

Figure 4.2.: Impedance spectra of cells (A) cycled at -10°C and (B) cycled at 25°C, EIS measured with $I_{AC,EIS}$=0.16 C at 25°C.

In a first step, impedance spectra of differently aged cells are compared. In Figure 4.2A, impedance results for aging of cell A at -10°C after 0, 150 and 330 cycles, and in Figure 4.2B the impedance results for the aging of cell D at 25°C after 0, 150 and 350 cycles are shown. The SoH decreased for aging at -10°C to 36% after 330 cycles and for aging at 25°C to 82% after 350 cycles. Both cells show characteristic and very similar typical features, such as two semi-circles and a Warburg impedance. The characteristic ranges as identified in Figure 4.1 are marked by the dashed lines.

In both cases, impedances increase with cycling in the same order of magnitude despite different aging conditions. Further, the frequency ranges seem unchanged. The increasing intersection with the x-axis at high frequencies with cycling which corresponds to the internal resistance R, magnified in the inlet in Figure 4.2. R increases for aging at -10°C from 0.21 Ω for 0 cycles to 0.3 Ω for 150 cycles up to 0.38 Ω for 330 cycles which equals an increase of 44.8%. Concerning aging at 25°C, R increases from 0.17 Ω to 0.18 Ω to 0.23 Ω which yields a significant smaller absolute and relative increase of 0.06 Ω or 26.1%, respectively.

R thus increases stronger for cycling the cells at -10°C in contrast to cycling at 25°C. Further, the low frequency semi-circle expands stronger for aging at -10°C compared to aging at 25°C. Both observations indicate that different aging effects may be trig-

gered due to the aging protocol. For example, plated lithium may lose contact with the anode and react with the electrolyte. This could result in thickening of the SEI or drying out of the electrolyte and therefore increased internal resistances [29]. However, the observed changes in the impedance spectra are in the same order of magnitude for aging at -10°C and 25°C.

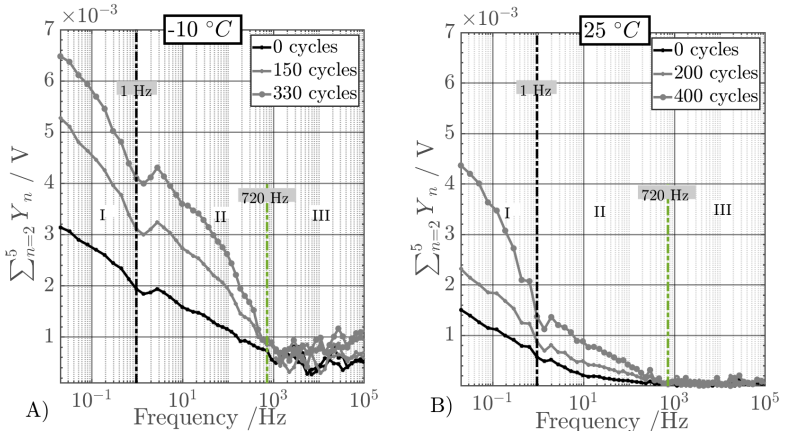

Figure 4.3.: NFR spectra for (A) cycling at -10°C and (B) cycling at 25°C (B), NFRA measured with $I_{AC,NFRA}$=1.5 C at 25°C.

In Figure 4.3A, overall NFR for aging at -10°C and in Figure 4.3B, overall NFR for aging at 25°C, are shown. Three characteristic frequency ranges for processes can be observed in the NFRA spectra, as identified in Figure 4.1. As before, the ranges are separated by a local minimum at approximately 1 Hz and at approximately 720 Hz. Both characteristic frequencies do not change with aging. In general, nonlinear voltages responses increase with the cycle number for both aging conditions. The initial values of the overall NFR in range I and II are higher for cell A used for aging at -10°C than for cell D used for aging at 25°C. This may be attributed to the smaller mass fraction of inactive compounds of the anode of cell A in comparison to cell D as well as to the non-calendered cathode. This is further in agreement to the higher initial impedances of cell A. For aging at -10°C, higher harmonic responses increase almost equally in range I and II. For aging at 25°C, the increase of the higher harmonic responses is greater in range I than in range II, as visible by the increased slope at low frequencies. Higher harmonic responses in range III are independent from the aging conditions and remain negligible.

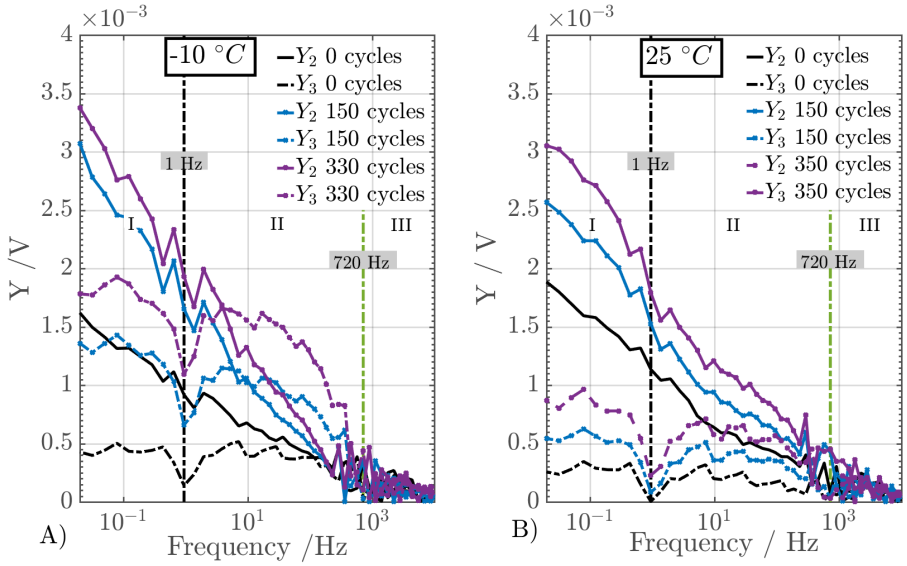

Figure 4.4.: Y_2 (black for 0 cycles, grey for 150 cycles, grey circle for 330 cycles) and Y_3 (black dashed for 0 cycles, grey dashed for 150 cycles, grey circle dashed for 330/350 cycles) for (A) cycling at -10°C and (B) cycling at 25°C, NFRA measured with $I_{AC,NFRA}$=1.5 C at 25°C.

In Figure 4.4A, the individual higher harmonics Y_2 and Y_3 for aging at -10°C are shown, and in Figure 4.4B for aging at 25°C. Prior to aging, Y_2 and Y_3 have the same progressions in both cells: Y_2 has a steep and constant slope in frequency range I and II; and Y_3 has almost constant values, a local minimum at 1 Hz and a further almost constant progression up to 720 Hz. Higher harmonic responses have comparable magnitudes for the different cells. For both cells, the amplitude of Y_2 is greater in frequency ranges I and II than the amplitude of Y_3. After aging, this characteristic behaviour changes significantly depending on the aging procedure. For the cells aged at -10°C, Y_3 increases significantly and higher harmonic responses become greater than Y_2 in range II. However, this drastic increase in nonlinear behaviour is not observed for the cell aged at 25°C: here, Y_2 still has greater higher harmonic responses than Y_3 in frequency range I and II. Range II has been assigned to electrochemical reactions. As such, changes in this region may be attributed to changes in the electrochemical reactions. Aging at -10°C thus seems to induce a different aging effect on the reaction of the electrodes than aging at 25°C. It is assumed that cycling at -10°C causes lithium plating on the anode which may react as well electrochemically. Therefore, the charge transfer kinetics between the electrolyte and the anode via the interphases, SEI as well as the plated lithium, may deteriorate, resulting in an increase of charge transfer resistances at the anode. This would lead to an increase of higher harmonic responses in frequency range II, as NFRA is measured with the same

current I_{AC}. Additionally, oxidation and reduction of plated lithium may be excited additionally to the inter- and deintercalation of lithium-ions in the anode which may affect the processes that are excited in frequency range II, too. Overall, the characteristic change of the intensity of Y_2 and Y_3, measured for aging at -10°C, and not at 25°C, seems a suitable indicator for detecting lithium plating and is thus further analysed in the following. Finally, no changes are observed in frequency range III, because no corresponding nonlinear processes are excited at such high frequencies.

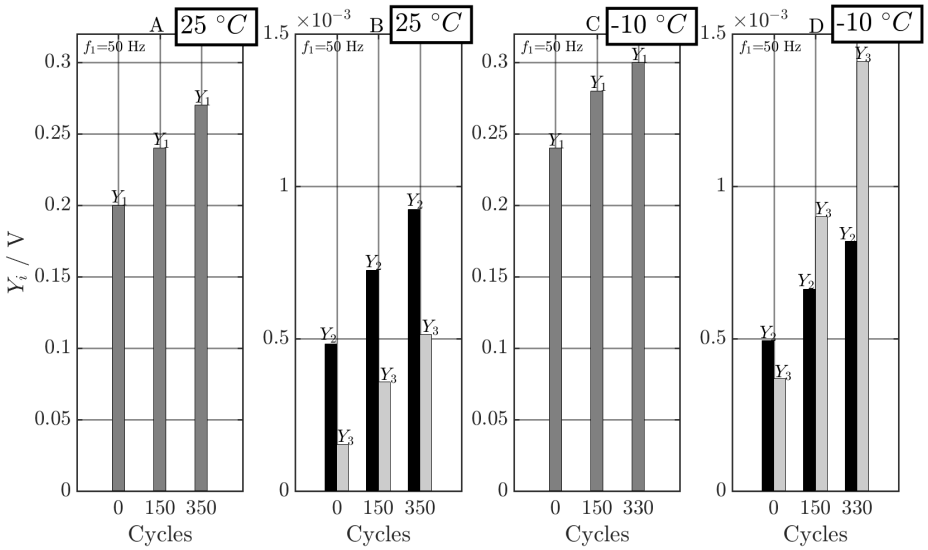

Figure 4.5.: Intensities of Y_1 (EIS), Y_2 and Y_3 (respectively NFRA) for aging at -10°C (A: Y_1; B: Y_2, Y_3) and aging at 25°C (C: Y_1; D: Y_2, Y_3).

For quantitative comparison, intensities of the linear output Y_1 and higher harmonics Y_2 and Y_3 are shown in Figure 4.5 for aging at -10°C and aging at 25°C measured with $I_{AC,NFRA}$=1.5 C at 50 Hz within frequency range II. The intensity of Y_1 increases for both aging conditions equally with cycling, whereas the characteristic change of Y_2 and Y_3 may be used to distinguish between both kinds of aging as priorly stated. Therefore, the frequency 50 Hz may be a good indicator for detecting the increase of the amplitude of Y_3 for aging at -10°C, most probably due to lithium plating.

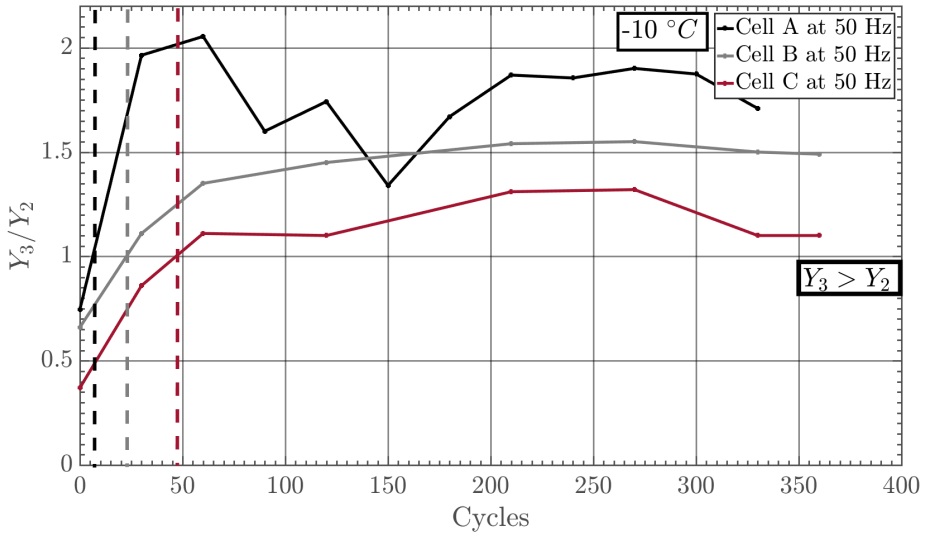

Figure 4.6.: The relation Y_3:Y_2 shown for aging at -10°C of cells A (black), B (grey) and C (red). The intensities of Y_2 and Y_3 were measured with $I_{AC,NFRA}$=1.5 C at 50 Hz.

To investigate the reproducibility of the observed characteristic nonlinear behaviour during cycle aging at -10°C, cells B and C which are geometrically identic to cell A are investigated as well. The progression of the relation of Y_3 to Y_2 is shown over cycling in Figure 4.6 for cells A to C, exemplary at the characteristic frequency 50 Hz. Values greater one indicate that the intensity of Y_3 has surpassed the intensity of Y_2. Also for cells B and C, the intensity of Y_3 increases stronger than the intensity of Y_2 in frequency range II with cycling and surpasses Y_2 after approximately 25 cycles for cell B and after approximately 47 cycles for cell C. While the ratio of Y_3:Y_2 keeps >1 for all cycle numbers, most of the increase is observed in the first 50 cycles, after which the increase significantly slows down and may even reverse [29]. Detailed physical analysis of this effect and of options to decrease fluctuations should be subject of future studies. Concluding, the observed characteristic intensity change of Y_3:Y_2 is reproducible for the examined cells and thereby most probably triggered by the cycling of the cells at a low temperature of -10°C. Further, measuring higher harmonics at 50 Hz seems to be a suitable, robust criterion for the detection of typical aging processes at -10°C, most probably lithium plating for cells B and C, as well. Additionally, the characteristic intensity change of Y_3:Y_2 may be considered as an indicator for increased resistances of the charge transfer kinetics in general and in this study for lithium plating in particular. In a next step, ex-situ analysis of the cells is performed for correlating aging of electrodes, especially lithium plating, to the characteristic dynamic responses to prove the hypothesis of detectability of plating with

NFRA.

4.3.3. Ex-Situ Analysis

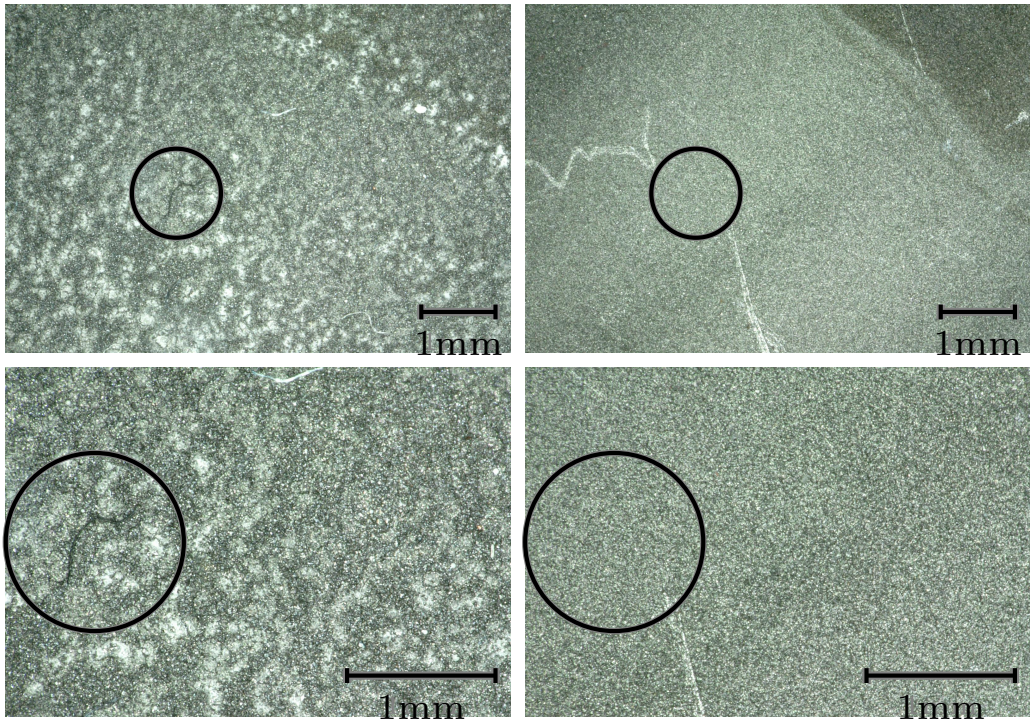

Figure 4.7.: Microscopic pictures with low (top) and high (bottom) magnifications of the anode of cell A aged at -10°C (left) as well as of the anode of cell D aged at 25°C (right).

After cycling, the aged cells were opened for ex-situ analysis. As previously stated, opening the cells under normal atmosphere results in the oxidation of plated lithium on the anode to Li_2CO_3. In Figure 4.7, microscopic pictures with two magnifications of the anode, aged at -10°C (left), and those aged at 25°C (right), are shown. For the cells aged at -10°C, white spots are visible which are assigned to white crystals of Li_2CO_3. For the cells aged at 25°C, however, no white spots are visible. This leads to the conclusion that aging of the cells at -10°C with the performed charging protocol actually results in lithium plating. Thereby, the characteristic differences in the non-linear dynamic behaviour for aging at -10°C and 25°C should be indeed related to plated lithium on the anode particles for cycling at -10°C. The increased values of Υ_3 in range II are therefore most likely related to lithium plating. As such, NFRA seems to be a suitable method for the assessment of presence of lithium plating. This holds for the presented cell type and should be confirmed for further cell designs in future studies.

4.4. Conclusions

In this study, the impact of aging on NFRA was analysed on three identical pouch cells and compared to impedance results. In particular, the impact of aging at -10°C and 25°C was compared. The aging effect lithium plating was identified by ex-situ analysis and correlated to changes in NFRA and EIS. Impedance results of the aging studies at -10°C and 25°C showed similar qualitative behaviour, with no clear characteristic distinction. By only analysing EIS, it is therefore not possible to distinguish unambiguously between different aging effects. With NFRA, however, a distinct difference in the dynamic behaviour was observed in the frequency range from 1 Hz to 720 Hz, correlated to electrochemical reactions.

It was found that only for the plated cells, Y_3 increases significantly more than Y_2, with Y_3 surpassing Y_2 after only a few cycles. The reference cell aged at 25°C, did not show this characteristic dynamic behaviour. It is assumed that the higher resistance of the charge transfer of lithium-ions between the anode and the electrolyte due to plated lithium on the surface of anode particles is responsible for the observed higher nonlinear amplitudes for frequencies in range II. Further, this indicates that Y_3 is more sensitive to such electrochemical reactions in comparison to Y_2. Reproducibility of these findings was shown by analysing the same characteristics for two further cells. As the sensitivity of lithium plating to NFRA is in the mid-frequency range and high sinusoidal excitation currents I_{AC} are applicable, electrochemical in-situ detection with a battery management system in an online measurement during operation or of a resting cell may be possible. Future work should focus on a quantitative correlation of the plated lithium and NFRA as well as the analysis of robustness of NFRA in comparison to other detection methods, such as ICA and DVA. Generally, this study shows that NFRA is a powerful new dynamic measurement method for analysing and differentiating between aging effects of LIBs. NFRA extends the possibilities of dynamic analysis of electrochemical systems significantly. In Chapter 5, different approaches for the estimation and quantification of the SoH using NFRA data-sets are investigated.

Chapter 5

Quantitative Evaluation for SoH Estimation[1]

5.1. Introduction

One focus of current research in the field of LIBs are the optimisation of aging diagnosis and lifetime prediction. Applying NFRA, the effect of aging mechanisms on the measured cell response is enhanced, and NFRA-based data might be more suitable for reliable SoH identification [1]. The application of NFRA for SoH estimation and Remaining Useful Life prediction is summarised in Figure 5.1 using a Strengths-Weakness-Opportunities-Threats (SWOT) matrix to assess the NFRA concept as well as its application in battery diagnosis and SoH identification. The strengths and opportunities of NFRA in LIB diagnosis look promising and motivate our experimental study. The weaknesses and threats seem to be manageable, in particular, as NFRA is a mature tool used in the state diagnosis in various application fields, as explained in Chapter 1.

Over the last decade, data mining approaches have become popular for diagnosing and predicting the cell state of LIBs with a battery management system. There are different approaches to unambiguously identify the complex and multi-scale aging of LIBs and to predict cell state indicators. Common data-driven diagnostic algorithms use artificial neural networks as well as Support Vector Machines. Both methods have already been implemented for state identification and for determining the Remaining Useful Life of LIBs for simple test cases [98–100]. Since the accuracy of the data-driven processes depends critically on the data basis, one also attempts to increase the information content of the raw data with the help of first-principles models. Hy-

[1] Parts of this chapter have been published in [3, 4].

	Positive	Negative
NFRA - Concept	**Strengths** - no need for steady-state analysis - specific frequency range - dependent on applied amplitudes - high currents reveal nonlinear system information	**Weaknesses** - novel concept / fewer experiences - nonintuitive - no dedicated hardware / measurement devices available - challenging noise to signal ratio
NFRA - Application	**Opportunities** - detailed LIB characterisation - reveals dedicated reaction mechanisms - credible SoH identification - precise fault detection & identification - online diagnosis under operating conditions	**Threats** - safety margin issues because of high currents - unique identification of relevant LIB characteristics fails - no market acceptance

Figure 5.1.: SWOT analysis of the NFRA for LIB characterization [2].

brid methods ideally combine the benefits of data mining with those of classical modeling principles [101, 102]. Furthermore, they serve as the basis for data mining of electrochemical manipulated variables and measurements, such as current, voltage, internal resistance, maximum usable capacity and impedances [34, 103]. To the authors' knowledge, diagnostic algorithms which also take NFR data for LIB diagnosis into account are currently not available in the literature.

In Chapter 5, two case studies for the applicability of NFRA as a diagnosis tool for LIBs and their SoH evaluation are investigated. In the first case study, an aging test of LIBs at 25°C is presented, and the impact of relevant aging mechanisms on the nonlinear dynamics of the cells is explained. Following a data mining strategy, an empirical degradation model is derived from informative NFR data sets. First, highly diagnostic features are extracted and used to calibrate the degradation model for the NFR-driven SoH identification. Finally, the performance of the degradation model is validated with additional cells and validation data, respectively.

In the second case study, a different approach is used for SoH estimation with NFRA by correlating nonlinear responses to cyclic-aging induced capacity fade of LIBs. The experimental results are validated with simulations on a surface reaction model based on Butler-Volmer kinetics.

5.2. Case Study I

First, the methods for SoH identification of LIBs used in the following are presented. The Spearman rank correlation is applied to determine the relevant frequencies related to LIB aging and NFR data, respectively. NFR data limited to meaningful frequency ranges are processed to build the degradation model which is implemented as a SVR approach.

5.2.1. SoH Degradation Model Based on Machine Learning

In the literature, various concepts for SoH degradation modeling are found which can be classified as first-principles, empirical, and hybrid models. First principles models translate electrochemical knowledge in equation systems but are generally difficult to derive. First, relevant processes have to be determined, associated model equations defined, and model parameters precisely identified. Thus, experimental data must be available to calibrate first-principles models. Alternatively, empirical models can be directly extracted from exhaustive data sets without any detailed knowledge of the underlying electrochemical processes. Please note that the quality of the empirical models depends critically on the available data and may fall short in extrapolation in the case of limited experimental data. Hybrid models, in turn, combine first-principles and data-driven concepts to use the benefits of both concepts; i.e., no perfect system understanding is necessary and missing data are compensated for with mechanistic rules. In this study, research is focused on empirical models and data mining techniques. Besides clustering and classification, regression concepts are frequently used for correlated data that are represented by governing equations for their input-output relationships. Complex neural networks and deep learning principles might be good candidates for data-driven SoH identification. The motivation for the present study, however, was to demonstrate the practical relevance of NFRA in SoH identification as an interesting concept for the next generation of battery management systems. Thus, a simple data-processing work-flow has been chosen consciously: 1) frequencies for NFRA which are highly representative for cell aging are identified via a correlation analysis, 2) informative features of the NFR data are calculated, 3) a sensitivity analysis reveals the most informative feature, and 4) based on this feature a SVR model is derived for SoH identification. The overall work flow is summarised in Figure 5.2 and described in detail below.

Correlation Analysis

Correlation measures the strength of association between two variables, and its value varies between +1 and -1 for positive and negative relationships. A value of ± 1 indicates a perfect degree of association between the two variables. As the correlation coefficient decreases towards 0, the correlation between the two variables also declines.

In this study, Spearman rank [104] is used for testing the relationship between NFR and cycle number. Spearman rank correlation is a non-parametric test that measures the degree of association between two variables. Spearman rank correlation analysis does not need assumptions about the distribution of data and is the appropriate correlation analysis when the values of one variable are monotonically related to the other variable. Spearman rank correlation coefficient ρ_S is calculated as:

$$\rho_S = 1 - \frac{6 \sum_{j=1}^{k} d_j^2}{k(k^2 - 1)}, \tag{5.1}$$

where d_j represents the difference between the ranks of two variables, and k represents the number of observations.

5.2.2. Feature Extraction and Sensitivity Analysis

To derive a data-driven SoH model, informative features are calculated from the NFR data that cover the identified relevant frequency range. Various characteristics can be determined addressing geometrical, frequency, time-frequency, and statistical measures [105, 106]. In this study, the geometrical features, y-axis intercept of the extrapolated NFR and the slope of NFR, are extracted for each aging cycle. In detail, a simple linear regression analysis of the extracted NFR data in the sensitive frequency range is executed. Please note that the linear regression analysis is a low-cost and

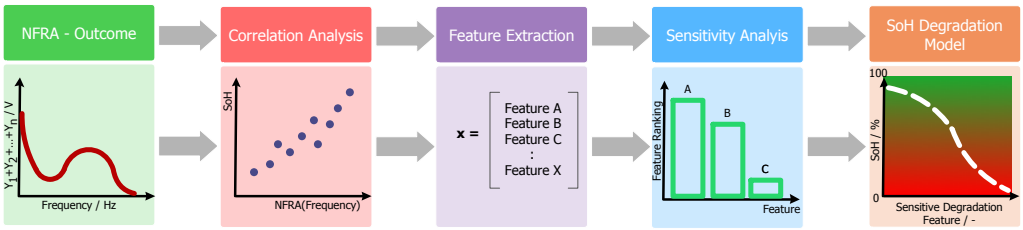

Figure 5.2.: The overall data processing scheme for SoH identification [3].

easy to implement approach and, thus, an ideal method for the extraction of the relevant aging features. In principle, additional features can be added, processed and translated to fewer but informative measures using principal component analysis and similar techniques [107, 108]. Here, the most informative feature is directly selected via a sensitivity study by determining which feature changes the most with the cycle numbers. Only for this feature, an empirical SoH model is derived based on SVR.

5.2.3. Support Vector Regression

Support Vector Machines can be used for classification and regression [109, 110]. In the case of regression, support vector machines are termed as support vector regression and is closely related to statistical learning. To build a regression model, a training data set $\mathcal{T}$ is required:

$$\mathcal{T} = \{\vec{X}, \vec{Y}\}, \tag{5.2}$$

where $\vec{X} = \{x_1, \ldots, x_K\}$ are the input and $\vec{Y} = \{y_1, \ldots, y_K\}$ the output sets. The goal of the SVR is to approximate the data set via a regression model F similar to:

$$F(x) = \sum_{l=1}^{M} a_l x_l + b, \tag{5.3}$$

where the coefficients b and $a_l, \forall l = 1, \ldots, M$ are unknown and have to be identified using the training data set $\mathcal{T}$. Please note that the SVR was originally developed for linear regression problems but can be easily extended to non-linear regression problems due to the so-called Kernel trick [111]. Moreover, empirical models based on SVR are robust to outliers, that is, data which are corrupted by large random errors or offsets. In addition, the SVR only considers those coefficients a_l that are relevant and sets non-relevant coefficients to zero which simplifies the model building and ensures well-posed identification problems in the case of limited data; that is, $K < M$. Thus, outliers and limited data have less impact on SVR models compared to ordinary regression techniques. For the technical details of SVR, the interested reader is referred to [111–113] and references therein. In the present study, frequency dependent NFR data sets during cycle aging are included in the training data sets. Technically, the following SVR setting is used within the R statistical computing environment including the e1071 library: radial basis kernel, an epsilon value in the insensitive-loss function of 0.1, and a C-constant of the regularisation term in the Lagrange formulation of 8.

Parameters	Symbol	Cell 1	Cell 2
Initial capacity	C_0 / mAh	32.8	33.6
Initial resistance	R_0 / Ω	0.21	0.29
Anode thickness	δ_a μm	44	45
Cathode thickness	δ_c μ m	52	58
Calendering degree anode	Π_a / %	10	10
Calendering degree cathode	Π_c / %	10	0
Mass fraction anode	ζ_a / wt%	0.90	0.93
Mass fraction cathode	ζ_c / wt%	0.90	0.90
Mass fraction inactive compounds anode	$\zeta_{add,a}$ / wt%	0.10	0.07
Mass fraction inactive compounds cathode	$\zeta_{add,c}$ / wt%	0.10	0.10
Volume fraction anode	ε_a / -	0.60	0.59
Volume fraction cathode	ε_c / -	0.57	0.64
Geometric surface area anode	$A_{geo,a}$ / cm^2	30.25	30.25
Geometric surface area cathode	$A_{geo,c}$ / cm^2	30.25	30.25

Table 5.1.: Performance and cell parameters of the investigated cells.

5.2.4. Experimental

Cells

LIBs in the pouch format with NMC as cathode and graphite as anode material were analysed in this aging study. Electrode manufacturing and cell assembling were done by the BLB, ensuring full control of the battery components. A solvent mixture of EC/DEC with a ratio of 3:7 with 1 M $LiPF_6$ as the conducting salt and Celgard 2320 as the separator were used. The inactive compounds included are PVDF as the binder and CB as the conducting additive. Cell specifications are summarised in Table 5.1.

Measurements

Cycle aging experiments at were conducted by charging with 1 C CC/CV and discharging with 1 C CC in a potential window between 2.9 V and 4.2 V using a MACCOR Battery Test System (Model 4200). The residual capacity C_i of the cell is extracted from the discharging step of the i-th cycles. NFRA was measured with a Zahner Electrochemical Workstation (Zennium) in the galvanostatic mode in a temperature chamber at a constant environmental temperature of 25°C and 50% SoC prior to aging

and after each 50^{th} cycle. The SoC is set by charging the cell with 1 C CC/CV with CV until the current is decreased to C/20. Afterwards, the cell is discharged with 0.5 C CC to 50% SoC. NFR data-sets that are analysed in this case study have been published in [1] in which detailed measurement settings are given in in the measurement description. As explained in Section 1.5.1, multiple data evaluation types of NFRA have been investigated in the course of this work. In case study I, the sum of amplitudes of higher harmonics are analysed with NFRA. In case study II, the root mean square of the first two harmonics (Equation 1.21) is used. The evaluation of NFRA data as root mean square is further recommended as the final evaluation type of NFRA, as described in Section 1.5.1.

Typically, the SoH of a LIB is estimated by dividing C_i of the i-th cycles by the initial capacity C_0 as in:

$$SoH_i = \frac{C_i}{C_0}. \tag{5.4}$$

In this case study, the SoH is calculated using highly informative NFR training data sets, and it is compared to the state-of-the art capacity based SoH estimation. This is motivated by the fact that a monotonic correlation of NFR with capacity loss and increased resistance has been observed [1]. Thus, this indicates that it is possible to evaluate directly the SoH via NFRA. The extrapolated NFR at the y-axis intercept are evaluated by linear regression analysis for all cycles i, $\sum_{n=2}^{5} Y_{n,min,i}$ is used for this purpose and normalized with the extrapolated NFR at the y-axis intercept $\sum_{n=2}^{5} Y_{n,min,0}$ prior to aging. The $SoH_{NFRA,i}$ measure is defined as:

$$SoH_{NFRA,i} = \frac{\sum_{n=2}^{5} Y_{n,min,i}}{\sum_{n=2}^{5} Y_{n,min,0}}. \tag{5.5}$$

Please note that with decreasing capacity and increasing internal resistance, NFR increase for a given current. Thereby, it can be deduced that an increase of NFR correlates to a decrease of the SoH. The initial overall NFR correspond to a new cell (SoH=100%), and $SoH_{NFRA,i}$ correlates to a decreased SoH after i-th cycle. Finally, the accuracy of the degradation model is calculated by comparing SoH_{SVM} to the SoH_i which is determined via standard capacity measurements during cycling.

5.2.5. Results and Discussion

Prior to NFR data analysis and the development of the degradation model, appropriate frequency ranges for the relevant processes have to be identified in NFR of the aging

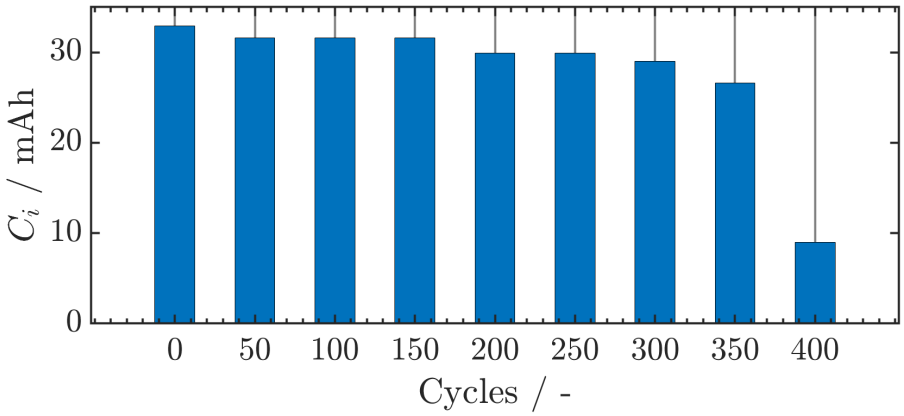

Figure 5.3.: Barplot of the progression of the residual capacity C_i over the cycle number.

training data sets [1, 40]. The training data sets haven been recorded in discrete cylce steps at each 50^{th} cycles, and therefore each cycle number is linked unambigously to one specific C_i, respectively SoH_i. In the barplot in Figure 5.3 the progression of C_i over the cycle number is shown. Until 350 cycles, C_i decreases linearly, however, a sudden drop of the cell capacity is observed towards 400 cycles. Such an aging behaviour has been studied in the literature and is discussed in detail in [114–116]. In Figure 5.4, NFR are shown over the frequency at the specific cycle steps from 0 to 400 cycles, at each 50^{th}, respectively. Processes in the low-frequency range I from 0.02 Hz to 1 Hz can be attributed to diffusion processes in active material particles and processes in the mid-frequency range II from 1 Hz to approximately 300 Hz to electrochemical reactions. Processes in frequency range III which show significantly lower NFR than the processes in ranges I and II, can most probably be attributed to ionic transport processes between and in the SEI and electrolyte. According to the literature, capacitive processes show minor or constant NFR in comparison to Faradaic processes with a Butler-Volmer kinetic. Further, the separation of range I and II at approximately 1 Hz is distinct in the training data sets and further not affected by cell aging. The identified process ranges with the corresponding time constants τ and frequencies are listed in Table 5.9. The correlation of processes to the frequency range with NFRA is supported by the corresponding impedance spectrum of the cell which is shown in the inlet of Figure 5.4 and discussed in detail in [1]. NFR in Figure 5.4 further illustrate that nonlinearities in the training data sets increase continuously with cycle aging, particularly in frequency ranges I and II. In frequency range III, NFR seem to be aging-independent. However, without using data analysis methods, it is not possible to state with sufficient certainty an explicit aging-to-NFR-correlation.

τ / s	ω-range / Hz	Process
50 to 1	0.02 to 1	Solid diffusion
1 to 0.003	1 to 300	Electrochemical reactions
0.003 to 0.0001	300 to 10000	Ionic transport processes at interfaces

Table 5.2.: Typical time constants and frequency ranges of processes identified with NFRA.

Therefore, in the next step, a correlation analysis of the NFR and cycle number as a function of the analysed frequencies is calculated using the Spearman rank correlation measure. In Figure 5.5, the correlation coefficients for Spearman ρ_S correlation is shown over frequency to identify the frequencies with relevant aging information in the training data sets. Three characteristic frequency ranges with different aging correlations are identified and can be distinctly separated at approximately 300 Hz. For frequencies higher than 300 Hz, range C, ρ_S varies strongly and therefore NFR data extracted at those frequencies have no valid information about the aging of the analysed LIB. For frequencies between 0.2 Hz and 300 Hz, range B, ρ_S is exactly 1 which

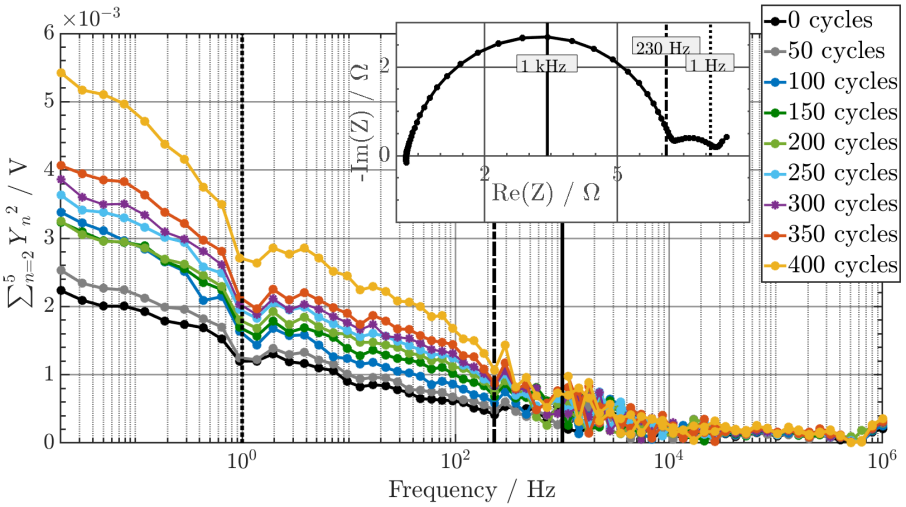

Figure 5.4.: NFR during cycle aging at each 50^{th} cycle, measured with I_{AC}=1.6 C; the impedance spectrum initial to cycle aging in the inlet, measured with C/15 C.

indicates a perfect positive degree of association between NFR and cycle number. In the low frequency range A, ρ_S differs from 1; ρ_S extends from 0.93 to 0.98, thereby indicating that NFR and the cycle number have a weaker positive relationship at these frequencies.

In the next step, the identified correlation ranges are interpreted by comparing correlation ranges A to C with the identified processes in frequency ranges I to III, as shown in Table 5.3. The most sensitive processes in the LIB are in the mid-frequency

ω / Hz	Correlation Coefficient	Process
A: $<$ 0.2 Hz	$>$0.95	Solid diffusion
B: 0.2 to 150	1	Electrochemical reactions
C: $>$ 150	Random	Ionic transport

Table 5.3.: Correlated frequency ranges, correlation coefficients and underlying LIB processes.

range from 0.2 to 300 Hz with a correlation coefficient of 1. Thus, NFR data measured at these frequencies are highly suitable for LIB aging quantification and the degradation model development. NFR data measured at frequencies lower than 0.2 Hz show a high correlation to aging as the correlation coefficient has values of $>$0.95. However, the data are not perfectly suitable in comparison with the higher frequency NFR data from 0.2 Hz to 150 Hz. For frequencies higher than 150 Hz, the NFR data have a lower and strongly varying correlation coefficient. Thus, NFR data at high frequencies have minor aging sensitivities and are therefore not applicable for SoH quantification and not considered for use as training data for the degradation model.

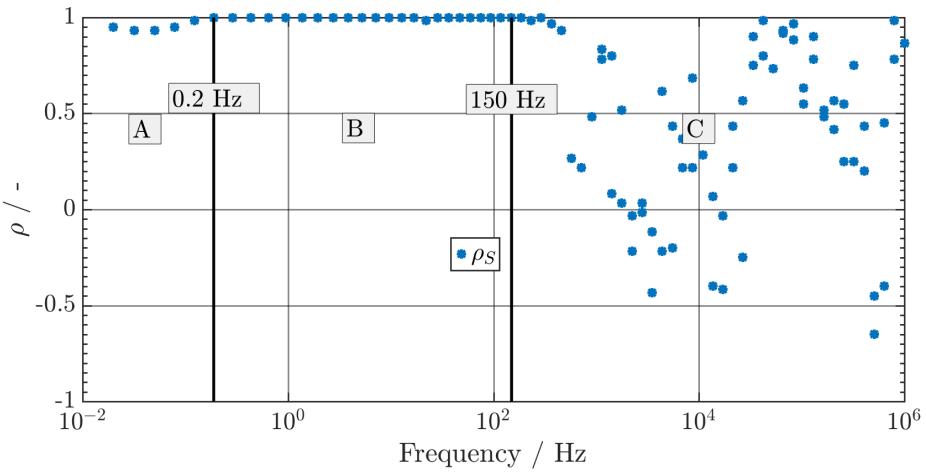

Figure 5.5.: Correlation coefficient ρ_S for estimating the correlation degree of the variables NFR and cycle number.

The aging-sensitive data identified for frequencies less than 150 Hz are extracted and shown over frequency in Figure 5.6. For calculating the degradation model using SVR, the geometrical features, y-axis intercept of the extrapolated NFR and the slope of NFR, are extracted for each aging cycle, respectively SoH_i. In Figure 5.7, the cycle specific feature values of extrapolated NFR at the y-axis intercept and the slope are plotted over the frequency of each cycle step. Apparently, extrapolated NFR at the y-axis intercept are more sensitive to aging than the slope of NFR. Extrapolated

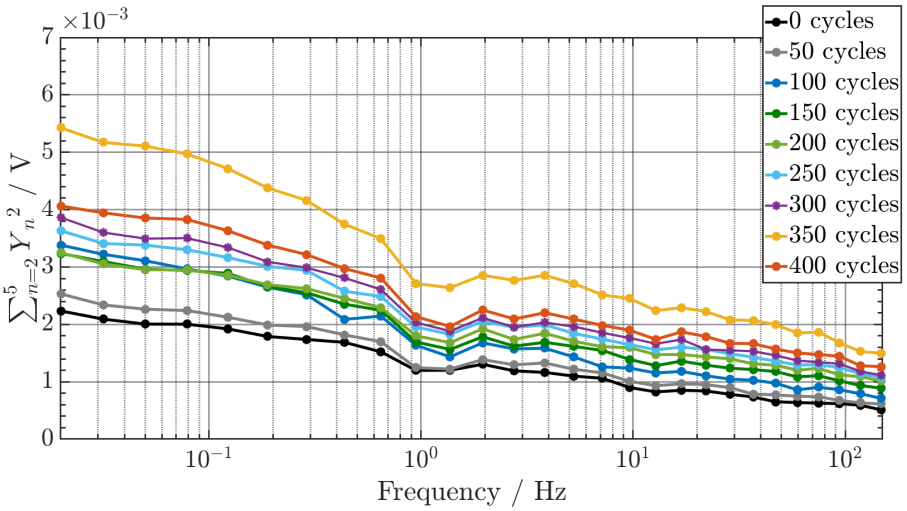

Figure 5.6.: Aging-sensitive NFR data extracted by correlation analysis.

NFR increase monotonically with the cycle number. The slope, however, deviates at cycles 100 and 150. Therefore, extrapolated NFR at the y-axis intercept are used for the parametrisation and training of the SVR degradation model. In Figure 5.8, the correlation of the SoH with the extracted degradation feature is shown. In the inlet of Figure 5.8, the values of the degradation features extracted from the data (blue) as well as the calculated values by the SVR model (red) are shown in terms of the cycle number to illustrate the high accuracy of the degradation model as the measured and calculated values match perfectly. In the next step, the performance of the

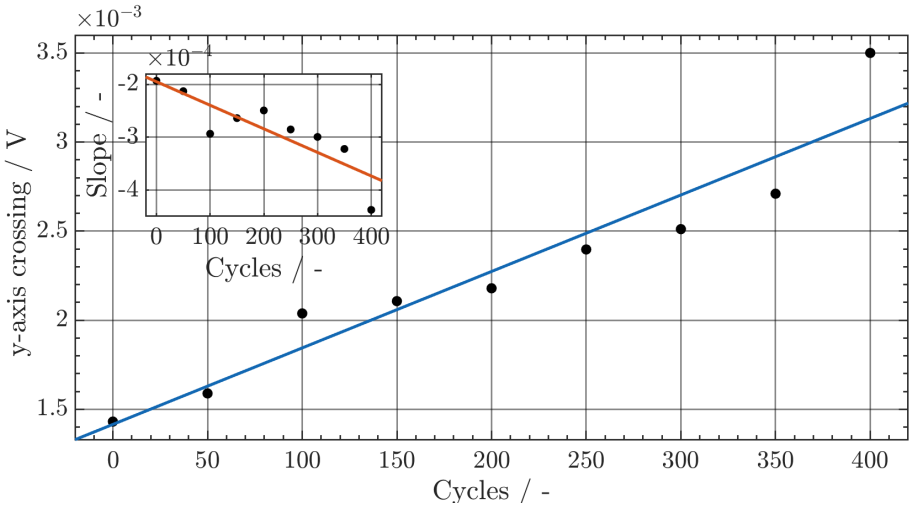

Figure 5.7.: Aging-sensitive NFR features extracted from high correlating training data sets.

degradation model is tested with validation data sets and additional cells which are non-identical to the initial test cells. NFR data sets identical and not identical to the training cells were applied to the degradation model, and the SoH was identified. The results of this validation are shown in Table 5.4. Moreover, the algorithm predicts the

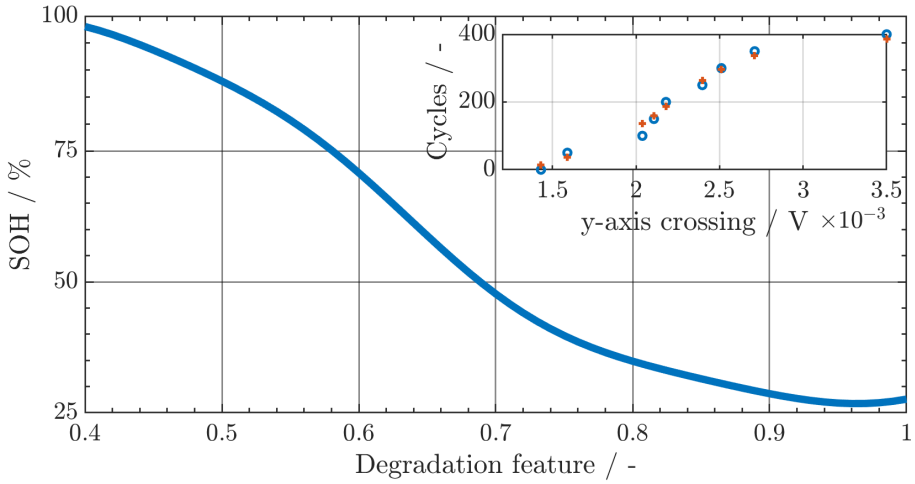

Figure 5.8.: Degradation model for SoH estimation calculated by SVR based on a highly aging-sensitive data feature and in the inlet, the degradation feature values extracted from the data (blue), as well as the calculated values by the SVR model (red).

SoH of an identical cell with a high accuracy of 3% and the SoH of a non-identical cell with a high accuracy of 4%. Thereby, it is shown that the NFR data recorded during cycle aging are highly suitable for the quantification of the SoH of the cell for both identical and for non-identical cells. Please note that the battery cells used in the case study are manufactured by the BLB and do not fulfill industrial standards, i.e., they may show substantial variations in their configurations which make a precise SoH identification difficult in general. The primary goal of this study was to provide the overall concepts and to demonstrate the proposed work-flow with first experimental results. Future work will focus on optimized and more sophisticated machine learning concepts with considerable higher accuracy, e.g., more informative features of NFRA data, empirical degradation models with memory (bayesian concepts), and rigorous uncertainty analysis in SoH identification and SoH prediction. With NFRA, the measurement time can be reduced up to 92% compared to standard EIS protocols, as the aging sensitivity of NFR data is sufficiently high in the mid-frequency range from 1 Hz to 100 Hz for the cells that are analysed in the presented study. Therefore, it is not necessary to analyse the overall frequency range from mHz to kHz which is typically done using dynamic measurement methods. Please also note that measuring the overall frequency range might be useful for SoH diagnosis of different cells and at different aging conditions.

Cell	Type	SoH_i	SoH_{SVM}	Accuracy / %
B	identical	28	29	3
C	identical	63	66	4
D	non-identical	100	96	4

Table 5.4.: Validation of the degradation model using identical and non-identical cells at different SoHs.

5.2.6. Concluding Remarks

In the first case study, the effective data-driven identification of SoH by using the novel dynamic analysis method NFRA has been demonstrated. First, an aging test of a LIB at 25°C was executed and a dynamic analysis with NFRA is performed in defined cycle steps at constant environmental and measurement conditions. The nonlinear dynamics of the cell changed regarding the aging protocol with proceeding cycle numbers. NFR increased monotonically with cycling, but the qualitative progress of NFR remained unaffected. The most likely aging effects at the applied cycling current and temperature are electrolyte degradation and the growth of the SEI, respectively. Such aging effects include capacity loss and increased cell impedance which lead to higher NFR values, as observed in this aging study.

For identifying the most sensitive frequency range for aging tests, a correlation analysis was performed. Here, the mid-frequency range from 0.2 Hz to 150 Hz shows the strongest correlation with LIB degradation. After extraction of extrapolated NFR at the y-axis intercept and the slope as informative features for LIB aging, the extrapolated NFR values at the y-axis intercept were used to parametrise the SVR model for SoH degradation, as it shows a higher correlation to NFR aging data. By using additional cells and data sets, the degradation model was validated and tested. It was shown that the degradation model can predict the SoH values with high accuracy. As the correlation coefficient indicates a perfect correlation of NFR to aging for all frequencies between 0.2 Hz and 150 Hz, a reduction of the measurement range from 1 Hz to 100 Hz for the analysed cells is suggested which leads to a dramatic reduction in measurement time of up to 92% compared to standard measurement protocols. In case study II, a further approach for the estimation of the SoH of LIBs using NFRA is discussed which takes the sensitivity of nonlinearities to the amplitudes of the excitation current I_{AC} into account.

5.3. Case Study II

In the second case study, nonlinear voltage responses are correlated to cyclic-aging induced capacity fade to estimate the SoH of LIBs, as described in Section 5.1. Thereby, the relation of the quotient of nonlinearities λ excited at two different excitation amplitudes of I_{AC} to the capacity fade of LIBs is investigated. Additionally, a surface reaction model based on Butler-Volmer kinetics is applied to consolidate the physical basis of the proposed measurement method. In the following, the theoretical and experimental basics of the case study are described.

5.3.1. Reaction Model

For an in-depth analysis of the presented capacity estimation, a reaction model is used. The focus of the model is to investigate the degradation of LIBs due to loss of

Parameter	Symbol	Value	Unit
Initial potential	$E(0)$	0	V
Exchange current density	i_0	10	$\mathrm{A\,m^{-2}}$
Double layer capacitance	C_{DL}	18	$\mathrm{F\,m^{-2}}$
Temperature	T	300	K
Particle radius	R_p	$10 \cdot 10^{-6}$	m
Volume fraction of active material	$\varepsilon_{s,0}$	0.6	-
Symmetry factor	α	0.5	-

Table 5.5.: Simulation parameters used in the reaction model.

specific surface area of the electrode at a given SoC and therefore one single electrochemical reaction is implemented and lithium accumulation is neglected in all phases. Transport processes in the electrode and electrolyte as well as the process dependency of the open circuit voltage are neglected in the model. The base case parameter set is provided in Table 5.5 and parameters are chosen to be in broad range suitable for LIBs [39]. All functions are embedded in Matlab, and time derivatives are solved with an ode-15s-solver. The reaction model contains a charge transfer reaction following

Butler-Volmer kinetics which is given in Equation 1.3. The overpotential η is calculated as following:

$$\eta = \Delta\phi - E(0), \tag{5.6}$$

with the electrical potential difference $\Delta\phi$ and the initial potential E(0) which is set to a constant value. Further, charge and discharge of the electrochemical double layer at electrode/electrolyte interfaces are implemented according to Equation 1.4. Both volumetric rates of Equations 1.3 and 1.4, j_{Li} and j_{DL}, sum up to the total current leaving/entering the electrode.

$$j_{tot} = j_{\mathrm{Li}} + j_{DL}. \tag{5.7}$$

The specific surface area of the electrode a_s is calculated as

$$a_s = 3\frac{\varepsilon_s}{R_p} \tag{5.8}$$

using the particle radius R_p and the volume fraction of active material ε_s [39]. The capacity loss is simulated based on the approach that active material loses the contact to the matrix of conducting additives and binder, for example by particle cracking [117]. Thus, the decreasing amount of active material, respectively the decreasing capacity, is implemented via decreasing the volume fraction of active material ε_s. Due the implementation of one single electrochemical reaction, ε_s is not specific to anode or cathode and therefore the initial volume fraction of active material $\varepsilon_{s,0}$ is a chosen value. $\varepsilon_{s,i}$ is calculated following the experimentally determined capacity loss, given in Equation 5.9. This correlation is defined as:

$$C = C_0\frac{\varepsilon_{s,i}}{\varepsilon_{s,0}} \tag{5.9}$$

where $\varepsilon_{s,0}$ is the initial volume fraction of active material, $\varepsilon_{s,i}$ the volume fraction of active material after i-th cycle and C_0 the initial capacity. This leads to a smaller specific surface area of the electrode a_s, according to Equation 5.8. Thereby, as shown in Equation 1.3, the current density j_0 has to increase, if the same current I_{AC} is applied to the reaction model. In Figure 5.9, the aging process of the electrode is illustrated schematically. To analyse cell dynamics, NFRA is simulated using the reaction model. For this purpose, a sinusoidal excitation current I_{AC} is applied to the model and the sinusoidal voltage output U_{AC} in the time domain is transferred to the frequency

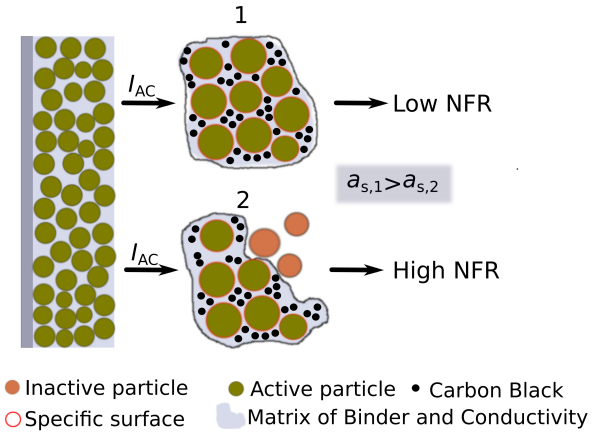

Figure 5.9.: Schematic illustration of (1) an electrode with original matrix of binder and conductivity and (2) an aged electrode after cyclic aging due to loss of active material in the matrix of binder and conductivity.

domain using a FFT. As in the experiments, the root mean square of the second and third harmonic is calculated (Equation 1.21).

5.3.2. Experimental

Cell Specifications

Single layer LIB cells with NMC as cathode, graphite as anode and a Celgard 2320 separator were used in this study. Electrodes were obtained from the BLB. As electrolyte, a solvent mixture of ethylene carbonate, dimethyl carbonate and ethyl methyl carbonate (EC/DMC/EMC) with a ratio of 1:1:1 with 2% vinyl chloride (VC) and 3% cyclohexylbenzene (CHB) as additives and 1 M $LiPF_6$ as conducting salt were used. The inactive components are PVDF as binder and CB as conducting additives. The

Parameter	Symbol	Unit	Value
Initial capacity	C_0	mAh	47
Initial resistance	R_0	Ω	0.23

Table 5.6.: Initial performance parameters.

characteristic cell parameters are listed in Table 5.7, and C_0 and R_0 as representative performance parameters in Table 5.6. The specific surface area of anode $a_{s,a}$ and cathode $a_{s,c}$ can be calculated from the given parameters with Equation 5.8.

Parameter	Symbol	Unit	Anode	Separator	Cathode
Thickness	δ	µm	55.25	20	60
Calendering degree	Π	%	40	-	25
Mass fraction of active material	ζ	wt%	0.91	-	0.90
Mass fraction of inactive compounds	ζ_{add}	wt%	0.09	-	0.10
Volume fraction	ε	-	0.35	0.50	0.40
Geometric surface area [2]	A_{geo}	cm^2	35	-	29.25

Table 5.7.: Specifications of the cells used for the aging study.

Measurements

NFRA and EIS were measured with a Zahner Electrochemical Workstation (Zennium) in galvanostatic mode. The frequency range was set between 20 mHz and 5 MHz, discretized with ten frequencies per decade above 66 Hz and five frequencies per decade for frequencies below 66 Hz. Amplitudes of higher harmonic responses from the Y_2 to Y_{10} are measured and measurement noise is recorded. Measurements were performed in a temperature chamber at a constant environmental temperature of 25°C and 50% SoC, if not further declared.

Aging of LIBs was conducted by cycling with 1 C CC/CV charging until $I_{CV} \leq$ C/20 and 1 C CC discharging in a potential window between 2.9 V and 4.2 V at 25°C using a MACCOR Battery Test System (Model 4200). Dynamic measurements were performed prior to aging and after each 50^{th} cycle at 50% SoC. The SoC was set by charging the cell with 1 C CC/CV with CV until the current decreased to C/20. Afterwards, the cell is discharged with 0.5 C CC to 50% SoC. The amplitude for EIS was set to 2 mA (C/20). NFRA was measured with three amplitudes of I_{AC} of 20 mA (0.5 C), 50 mA (1.1 C) and 100 mA (2.3 C). Details for the dynamic measurements are listed in Table 5.8.

Parameter	Symbol	NFRA	EIS
Excitation Current	I_{AC}	0.5 C/1.1 C/2.3 C	0.05 C
Frequency	ω	0.02 Hz to 10^4 Hz	0.02 Hz to 10^6 Hz
Measurement points	n_p for $\omega <$ 66 Hz	5	10
Measurement points	n_p for $\omega >$ 66 Hz	5	10
State-of-Charge	SoC	50%	50%

Table 5.8.: Measurement parameters of the dynamic analysis performed in defined cycling steps.

5.3.3. Results and Discussion

Process Identification

Prior to analysing and discussing SoH diagnosis, typical frequency ranges for processes have been identified in the higher harmonic responses of the unaged LIB in Figure 5.10, according to previous chapters. Processes in the low- to mid-frequency range Ia and Ib from 0.02 Hz to 10 Hz may be attributed to diffusion processes in active material particles and electrochemical reactions. Processes in frequency range

Range	τ / s	ω-range / Hz	ω / Hz	Process
Ia	50 to 3	0.02 to 0.3	0.2	Solid diffusion
Ib	3 to 0.1	0.3 to 10	1	Electrochemical reactions
II	0.1 to 0.0001	10 to 10000	1000	Ionic transport processes at interfaces

Table 5.9.: Characteristic time constants and frequencies identified from NFRA.

II which show significantly lower harmonic responses than the processes in range I, may be attributed to ionic transport processes, i.e. migration, between and in the SEI and electrolyte. Those processes, typically, show almost constant, minor higher harmonic amplitudes than higher harmonic amplitudes of electrochemical reactions of the electrodes in range Ia and Ib [1]. However, the separation of range Ia and Ib

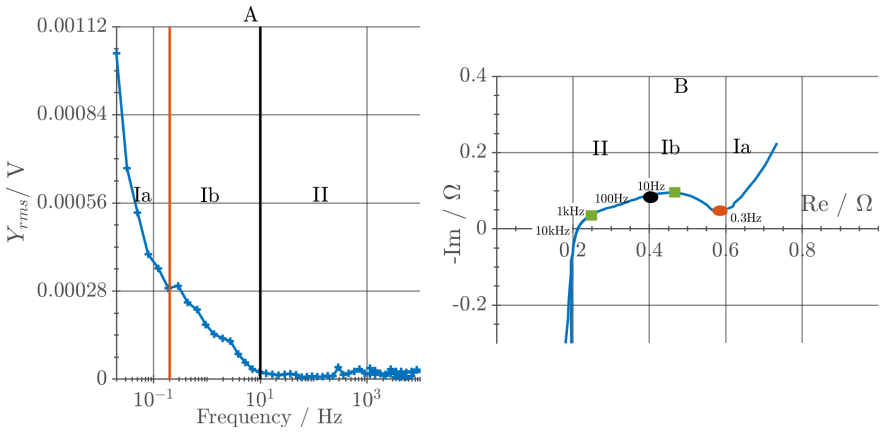

Figure 5.10.: (A) NFR spectrum and (B) impedance spectrum measured with $I_{AC,EIS}$=0.1 C and $I_{AC,NFRA}$=2.3 C prior to cycle-aging. The green rectangles mark the characteristic frequencies of the semi-circles of EIS.

at approximately 0.3 Hz is not as distinct for the cells tested in this study as for previously analysed cells [1, 2]. This demonstrates that NFRA highly depends on the cell specifications and cell type [40], as discussed in Chapter 3, as well. The correlation of processes to frequency ranges is supported by process characterization in the impedance spectrum in Figure 5.10B. Roughly, two overlaying semi-circles can be identified. One semi-circle with a characteristic frequency at approximately 1 kHz and a second semi-circle with a characteristic frequency at approximately 3 Hz. However, these semi-circles are not clearly distinguishable. According to literature, the higher frequency semi-circle corresponds to the ionic transport reactions at and in the interface of electrolyte and SEI and the lower frequency semi-circle corresponds to the electrochemical reactions [66, 118]. A further indicator supporting this correlation is that the cell shows distinct and characteristic NFR in frequency range Ib which corresponds perfectly to the lower-frequent semi-circle which ranges from 0.3 to 10 Hz and is marked between the black and orange bullet in the impedance spectrum. Region Ib is separated from lower frequency responses by a characteristic small minimum and from the high frequency part where nonlinearity is negligible. The lower frequency range for frequencies <0.3 Hz in both spectra corresponds to the diffusion process. Generally, characteristic regions of impedance features and frequency ranges in NFRA correspond perfectly for the analysed cell. Further, process characterization is in strong agreement to identification and correlation carried out in the previous chapters [1, 2, 40].

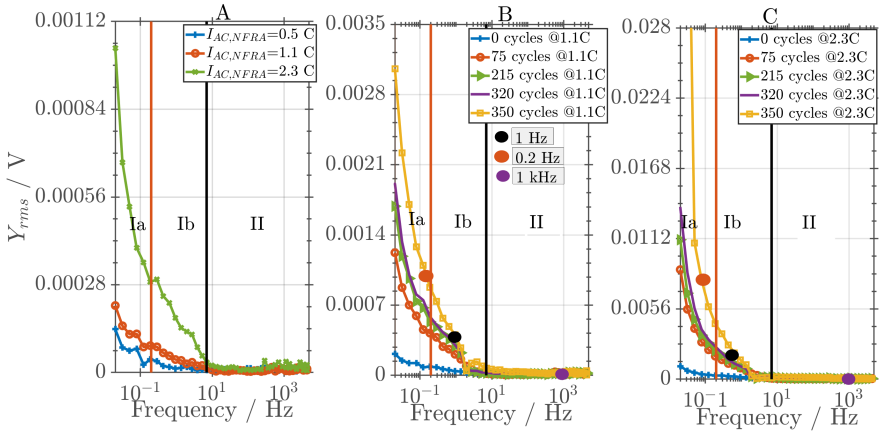

Figure 5.11.: (A) NFRA measured with three amplitudes of I_{AC}=0.5 C, 1.1 C and 2.3 C prior to cycle-aging, (B) during cycle-aging for $I_{AC,NFRA}$=1.1 C and (C) for 2.3 C.

Experimental Aging Analysis

In Figure 5.11A, Y_{rms} prior to aging at three amplitudes of I_{AC}=0.5 C, 1.1 C and 2.3 C are shown. Y_{rms} increase with increasing amplitude of I_{AC} in frequency range Ia and Ib. In range II, Y_{rms} are almost independent of the excitation amplitude. This confirms that in frequency range II only processes with a minor nonlinear current-voltage relation and most probably no processes with a Butler-Volmer kinetic are excited. In the following aging study, NFRA measured with an excitation amplitude of I_{AC} of 0.5 C is not further considered for the analysis due to small nonlinear values. In Figure 5.11 B and C, Y_{rms} for cycle aged LIB measured with I_{AC2}=1.1 C and I_{AC1}=2.3 C are shown after 0, 75, 215, 320 and 350 cycles. In general, Y_{rms} increase with number of cycles. Further, Y_{rms} are higher for a higher excitation amplitude of I_{AC}. Y_{rms} excited with I_{AC1}=2.3 C are approximately one order of magnitude higher than Y_{rms} excited with I_{AC2}=1.1 C.

In a first step of mapping NFRA and capacity loss, Y_{rms} are extracted at the characteristic frequencies and time constants τ listed in Table 5.9. In Figure 5.12, it is chosen to show the inverse of Y_{rms} over cycles instead of Y_{rms}, because the inverse decreases during aging. Thereby, a better quantitative correlation to the progression of the capacity decrease is possible. In Figure 5.12A to 5.12F, cell capacity loss and the inverse of Y_{rms} at three characteristic frequencies are shown with cycling. Starting with C_0 of 47 mAh which corresponds to a SoH of 100% at 0 cycles, the capacity decreases after 75 cycles to 34 mAh which corresponds to a SoH of 72.3%. Afterwards, it increases again slightly to 37 mAh after 275 cycles and to 38 mAh after 295 cycles. At the end of cycle-aging at 350 cycles, the capacity of the cell is 37 mAh which corresponds to a SoH of 78.8%. At 1 kHz, the progression of the inverse of Y_{rms} strongly differs from

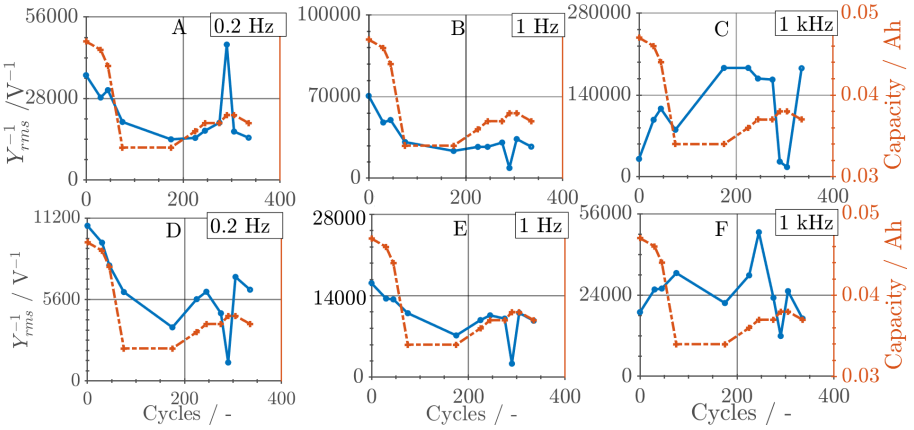

Figure 5.12.: The inversed absolute values of Y_{rms} measured with I_{AC2}=1.1 C (top) and I_{AC1}=2.3 C (bottom) and cell capacity shown for cycle-aging at three characteristic frequencies: (A and D) 0.2 Hz, (B and E) 1 Hz and (C and F) 1 kHz.

the progression of the capacity fade for both excitation amplitudes, shown in Figure 5.12C and 5.12F. As Y_{rms} partly increase with SoH and partly decrease, and trends for the two amplitudes differ strongly, Y_{rms} and SoH cannot be correlated at 1 kHz. Thus, this is in correlation to the process identification in previous chapters in which higher harmonic responses excited in range II, characteristic for ionic transport processes between the SEI and electrolyte, have been identified to be not sensitive to aging of LIBs [1, 2].

At 0.2 Hz, shown in Figure 5.12A and 5.12D, as well as at 1 Hz, shown in Figure 5.12B and 5.12E, however, a correlation between the inverse of Y_{rms} and the capacity can be identified for both excitation amplitudes. As expected, the inverse of Y_{rms} decreases for decreasing capacity for most cycles. However, there are deviations from this characteristic behaviour, e.g. at 45 and 290 cycles. At 45 cycles, the inverse of Y_{rms} increases slightly for a lower capacity compared to previous cycles for both excitation amplitudes. However, this increase is only small and corresponds to a Y_{rms} decrease in the μV range which is in the range of measurement uncertainty due to an accuracy of the device of $\pm 250 \cdot 10^{-6}$ V. At 290 cycles, however, the inverse of Y_{rms} decreases sharply for both excitation amplitudes at 1 Hz and for the higher excitation amplitude at 0.2 Hz, as well. In contrast to this, the inverse of Y_{rms} increases strongly at this cycle for the lower excitation amplitude at 0.2 Hz. These intense spikes of Y_{rms} are out of the range of measurement uncertainties and indicate either specific, yet not understood changes in the cell or external disturbances of unknown source occurring right after the 290^{th} cycle. Therefore, the correlation of the inverse of Y_{rms} to the capacity decrease is not considered to be reliable at these cycles. Further, it

is noticed that the inverse of Y_{rms} decreases even if the capacity stays constant over multiple cycles, e.g. from 35 to 75 cycles, for both excitation amplitudes at 0.2 Hz and 1 Hz. Thereby, it is shown that it may not be possible to perfectly match the residual capacity to the overall Y_{rms} values. However, a general correlation between Y_{rms} and cycling can be identified. It is assumed that Y_{rms} not only correlates to aging processes decreasing the cell capacity respectively the specific surface area, e.g.loss of active material of the matrix of binder and conductivity, but also to aging processes, such as conductivity loss which increases the overall internal cell resistances [17]. Loss of specific surface area includes a reduction of the maximal extent of lithiation of the electrodes and therefore a decreasing cell capacity. Y_{rms} may increase due to both aging types, capacity and power fade.

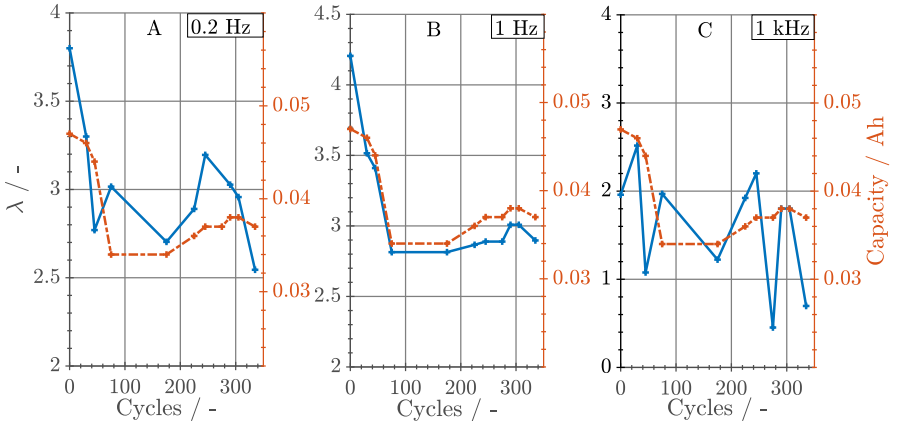

Figure 5.13.: λ and cell capacity shown for cycle-aging at three characteristic frequencies: (A) 0.2 Hz, (B) 1 Hz and (C) 1 kHz.

In a next step, the capacity decrease is correlated to λ for aging quantification of LIBs based on NFRA. The quotient λ is deduced from the performance efficiency, Θ, of LIBs which can be used to quantify and monitor the performance of LIBs at different discharging currents from typically used cycle rate tests [119, 120]. For calculating Θ, the capacity at a higher discharging current is correlated to the capacity at a lower discharging current. Ideally, the capacity of the LIB at the higher current is close to the capacity at the lower discharging current. A performance efficiency Θ close to 1 is an indicator for a high performing LIB in contrast to a LIB with a lower Θ. In the following, this approach is transferred on NFRA for quantifying aging and estimating the SoH. Therefore, it is expected that the ratio λ decreases over cycling, as nonlinearities of the LIB increase for decreasing cell capacity at the corresponding excitation amplitudes, as demonstrated in the previous section.

In Figure 5.13A to 5.13C, the ratio λ of the root mean square of the second and the

third harmonic response measured at I_{AC1}=2.3 C and I_{AC2}=1.1 C is shown over cycling at the characteristic frequencies. The progression of capacity fade over cycle-aging and the progression of λ measured at 1 Hz are in strong agreement. If the capacity decreases, λ decreases and if the capacity is constant, λ is constant, too. This characteristic correlation is not observed for the progression of capacity fade and the inverse of Y_{rms}, as already stated. Also, the progressions of λ measured at 0.2 Hz and 1 kHz fluctuate and do not match the progression of capacity fade over cycle-aging. They even show strong fluctuations, rendering these frequencies as unsuitable for monitoring SoH.

As 1 Hz is in the frequency range of the electrochemical reactions, the correlation of λ to capacity may be correlated to the loss of the specific surface area a_s of the electrode. If the capacity, respectively a_s, decreases and I_{AC} of the dynamic analysis are kept constant, the current flow per specific surface area, the volumetric current density, is higher. If the current density increases, cell overpotentials have to increase, as well. Consequently, increasing overpotentials cause an increase of Y_{rms}. This is observed for both excitation amplitudes of I_{AC} that are used for dynamic analysis at the defined cycling steps (I_{AC1}=50 mA, I_{AC2}=100 mA). However, Y_{rms} does not increase linearly with higher I_{AC}. For smaller I_{AC}, the relative increase of Y_{rms} is higher for decreasing capacity than for higher I_{AC} which will be demonstrated in the following section using simulation. Consequently, λ will decrease for decreasing capacities.

Experiments vs. Simulations

As there is presently little knowledge about how to reliably interpret changes in NFR spectra, here physicochemical models are used to aid interpretation. This has already been successfully demonstrated by Wolff et al. and Murbach et al. [40, 68] for unaged spectra. Thus, in a next step, the correlation of λ and capacity fade is analyzed in-depth by using the reaction model, as introduced in section 2.2. A base case parameter set is given in Table 5.5. As the focus is on a model-based investigation of the reaction process, the double layer capacitance C_{DL} is chosen to get the best possible correlation of measurements and simulations at the frequency characteristic for reaction, e.g. around 1 Hz in range Ib. Therefore, only the corresponding characteristic frequency range Ib between approximately 0.2 to 10 Hz is of interest in the following discussion. In a first step, amplitude dependency of NFRA is investigated prior to a simulative aging analysis via a variation of the specific surface area a_s.

In Figure 5.14A, simulated NFRA of a single reaction according to Butler-Volmer

range	ω_{sim} / Hz	ω_{exp} / Hz	Process
Ia	-	0.02 to 0.3	Solid diffusion
Ib	0.2 to 10	0.3 to 10	Electrochemical reactions
II	-	10 to 10k	Ionic transport processes between and in the SEI and electrolyte

Table 5.10.: ω_{sim} of NFRA simulations in comparison to ω_{exp} of NFRA measurements.

kinetics are shown for a variation of I_{AC}. Beginning with a frequency of approximately 10 Hz until 0.2 Hz, Y_{rms} increase in the simulations. This steep slope of Y_{rms} is observed in experiments in range Ib, as well. For frequencies smaller than 0.2 Hz and above 10 Hz, Y_{rms} are constant in the simulations due to the implementation of only one single electrochemical reaction with neglection of any transport processes, e.g. diffusion of lithium-ions in the active material particles, as priorly discussed. In contrast to this, the full model analysis, shown in Figure 5.14B, contains transport and showed similar steep increase of Y_{rms} in the low frequency range, shown in Figure 5.14B. The Figure 5.14B is taken from a study by Wolff et al. in which a standard Pseudo-2-Dimensional model with porous, structured electrodes has been used in a model-based analysis of the harmonic voltage responses of LIBs [39]. Hereby, it is important to note that Wolff et al. analysed higher harmonic responses of the initial, transient part of the battery which results in a peak-shaped progression of higher harmonics in the frequency range characteristic for the electrochemical reaction, as surface concentration gradients and potentials at the interface between electrode and electrolyte are not in equilibrium, yet [40]. In the presented study, however, the steady-state response of the battery is analysed and therefore the electrochemical reaction process is already in equilibrium. Due to this, the characteristic progression differs. Still, the frequency range characteristic for the electrochemical reaction as well as the amplitudes of harmonic voltage responses are similar in the simulations with the reaction model and the Pseudo-2-Dimensional model. The analysis of harmonic voltage responses of a LIB in a steady-state with a full model which also contains transport processes, is out of scope in the work published by Wolff et al [40]. In general, NFRA simulations confirm the findings of the experimental process correlation. It is, thus, expected that changes in the specific surface area and thus kinetics

impact nonlinear responses in range Ib. Any analysis of kinetic effects and aging or design related changes in kinetics should therefore focus on this range.

In the reaction model, the variation of ε_s and therefore the variation of the specific surface area of the electrode a_s, according Equation 5.8, is used to analyze the impact of decreasing cell capacity on NFRA. The input excitation amplitude of I_{AC} is kept constant for this variation. If ε_s and thus a_s decreases, Y_{rms} increase, as shown in Figure 5.15A and 5.15B for 3 A and 1.4 A. Thereby, it is shown that decreasing capacity due

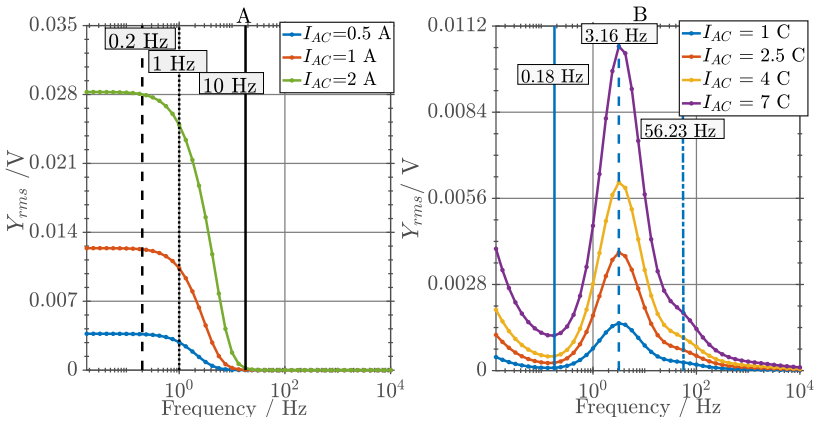

Figure 5.14.: (A) NFRA simulations on the reaction model with current amplitudes 0.5 A, 1 A and 2 A and (B) NFRA simulations on a full model with current amplitudes of 1 C, 2.5 C, 4 C and 7 C according to Wolff et al. [40].

to loss of active material results in increased Y_{rms}, but does not affect the nonlinear frequency responses in its characteristic progression. Further, in Figure 5.15C, Y_{rms} at the characteristic frequency 1 Hz are shown for a broad variation of active material fraction ε_s and two excitation amplitudes of I_{AC}. The simulations suggest that Y_{rms} extracted at specific frequencies increase exponentially with decreasing cell capacity. Y_{rms} increase over cycling in the experiments, as well. However, as discussed, experimental capacity has an unexpected non-monotonous behavior with cycling number whereas Y_{rms} increase monotonously. This feature cannot be reproduced with the modeled scenario of specific surface area loss as cause for cycling based capacity fade. It remains open for now which additional underlying aging-triggered changes in the cell cause the capacity increase. Further, a comparison of Y_{rms} in Figure 5.15C illustrates that for smaller I_{AC} the relative Y_{rms} increase is higher for decreasing capacity, respectively ε_s, than for higher I_{AC}. For an excitation amplitude of I_{AC}=1.4 A, Y_{rms} increase about 2 times for an decrease of ε_s=0.6 to 0.4, but for an excitation amplitude of 3 A only approximately 1.6 times. This was observed in the experiments, as well. These simulations predict that λ decreases with decreasing ε_s which is investigated in the following section.

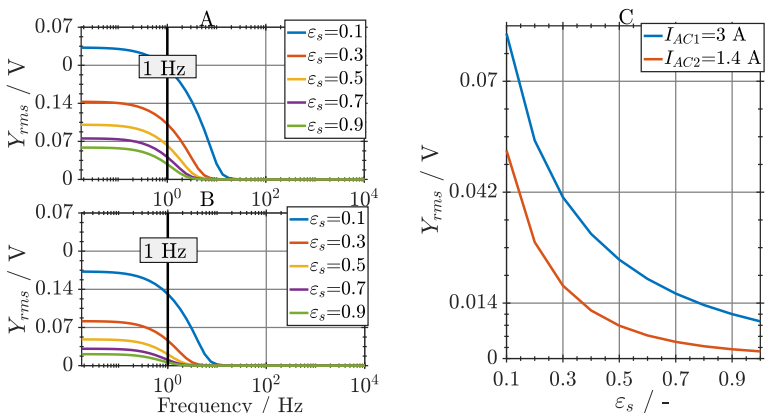

Figure 5.15.: Impact of solid fraction on NFRA simulations for (A) I_{AC1}=3 A and for (B) I_{AC2}=1.4 A as well as (C) at the specific frequency 1 Hz for a variation of ε_s.

5.3.4. Simulative Aging Analysis

In the following, the correlation of λ and decreasing cell capacity is analyzed using the reaction model. NFRA simulations are conducted for a variation of excitation currents and active material fractions ε_s, and therefore for capacity loss according Equation 5.9. As in the experiments, the characteristic frequency of 1 Hz is chosen

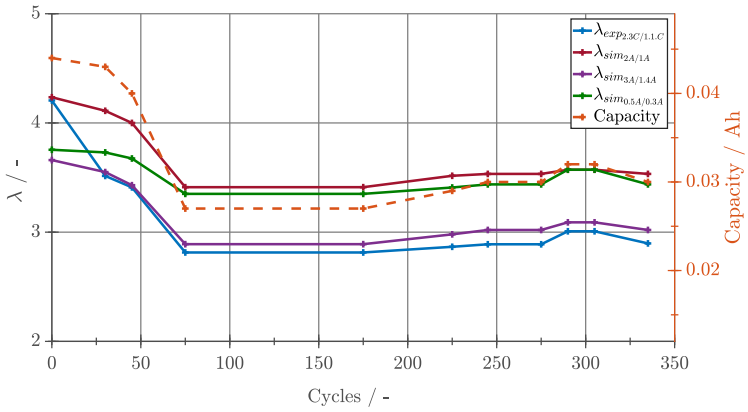

Figure 5.16.: Measured and simulated λ at 1 Hz and cell capacity shown for cycle-aging.

for the calculation of λ. As previously stated, a strongly simplified model is used where only the kinetic of one single electrochemical reaction is implemented in the reaction model. A discharge capacity cannot be determined and, thus, the adaption of the absolute excitation current in relation to a cell capacity is not possible, as it has been done in experimental studies. However, the relative excitation currents used in the reaction model have been set in correspondence to the experimental investigations. Further, to evaluate the sensitivity of λ to the excitation currents, multiple λ with different excitation amplitudes are simulated. The ratio of simulated and experimental λ (left y-axis) as well as capacity (right y-axis) are shown over cycle-aging

in Figure 5.16. All simulated λ for decreasing ε_s show the same progression as the corresponding experimental λ for decreasing cell capacity. The simulated λ differ quantitatively due to the variation of the excitation amplitudes of I_{AC}, but not qualitatively. The values for the NFR quotient λ gathered from the experimental study can be identified using sinusoidal excitation currents of 3 A and 1.4 A in the simulations. For these amplitudes, the quantitative differences between measured and simulated λ are approximately 5% which is a good approximation regarding that a strongly simplified model was used for the simulations. In general, simulations with the reaction model confirm that changes in capacity due to loss of active material, respectively specific surface area can be correlated to λ, suggesting that this measure is in principle suitable to detect capacity losses with NFRA. λ measured at the characteristic frequency of 1 Hz appears to be a reliable and accurate parameter for determining SoH decrease due to capacity loss.

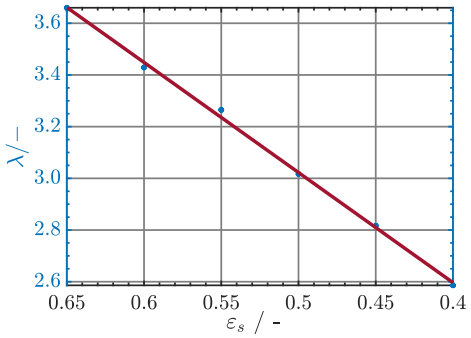

Figure 5.17.: Simulated λ at 1 Hz for decreasing capacity.

In a last step, NFRA is simulated for a capacity loss by linearly decreasing ε_s and therefore the specific surface area a_s. Capacity loss is therefore presented via decreasing of the active material fraction ε_s, as in detail explained previously. λ at the characteristic frequency 1 Hz is calculated accordingly as a function of ε_s. This allows to deduce a formula to calculate SoH from λ. In Figure 5.17A, it is shown that λ decreases almost linearly with decreasing ε_s, respectively the linear decreasing cell capacity, at the characteristic frequency of the electrochemical reaction. Thereby λ and the capacity decrease due to the reduction of the specific reaction surface of LIBs have an almost linear correlation. λ at frequencies specific for the electrochemical reaction, thus, is identified as a good parameter for SoH estimation of LIBs, as given in Equation 5.10.

$$SoH = \frac{\lambda_i}{\lambda_{initial}} 100, \tag{5.10}$$

with the initial quotient $\lambda_{initial}$ and the quotient after the i-th cycle λ_i.

5.3.5. Conclusions

A novel approach for the estimation of capacity fade due to loss of specific surface area is presented, e.g. due to loss of active material, and therefore the SoH of LIBs. A cycle-aging experiment was conducted at 25°C and NFRA was applied at two current amplitudes in defined cycle steps to study the impact of aging on NFRA. The ratio of nonlinearities at those excitation amplitudes, namely λ, shows a very good qualitative correlation to the capacity fade over cycles in the characteristic frequency range of the electrochemical reaction. Therefore, a capacity decrease leads to a decreased λ. If the capacity does not vary with cycle-aging, neither does λ. λ at 1 Hz was found to be an excellent parameter for this purpose. In contrast to this, the absolute Y_{rms} increase even if the cell capacity stays constant for multiple cycles. Therefore, the overall nonlinearities of the cell seem not to be suitable for SoH quantification. The finding from the experimental study is further analysed in-depth by using NFRA on a reaction model with Butler-Volmer kinetics and with a dynamic charge balance at the electrode surface. NFRA simulations on the model support the experimental findings. Simulated λ for decreasing active material fractions, which were adjusted in relation to the experimentally measured cell capacity, showed a similar progression as λ from cycle-aging measurements.

Concluding, determining λ at one single frequency in the characteristic excitation range of the electrochemical reactions was found to be a suitable method for the estimation of capacity fade of LIBs. Therefore, using NFRA at two excitation amplitudes on battery systems may be a powerful diagnosis technique for the estimation of the SoH. Future studies are needed to evaluate the robustness of the method and whether the method would be suitable for on-board diagnosis with a battery management system. If evaluated positive, NFRA may prove to be a low cost, fast and robust technique for estimating SoH. In general, the results of both case studies demonstrate the usefulness of NFRA regarding aging diagnosis and SoH estimation.

Chapter 6

Summary and Outlook[1]

6.1. Summary

In contrast to NFRA, state-of-the-art dynamic measurement methods for LIB diagnosis, such as the established EIS, analyse LIBs in regard to linear system behaviour. Thereby, information about the nonlinear current-voltage relation is only accessed linearly. Due to this, highly informative nonlinear dynamics have been neglected so far and the maximum potential of dynamic analysis of LIBs has not been exploited, yet. In this work, these nonlinearities of LIBs are taken into account for the first time. In Chapter 1, the subject of this thesis was brought into context by providing electrochemical theory of LIBs as well as a an overview of the most prominent aging effects. Further, a review of linear and nonlinear dynamic analysis methods regarding state diagnosis of LIBs was given. Chapter 2 and 3 focused on establishing the experimental fundamentals of NFRA measurements on LIBs. First, the amplitude dependency of I_{AC} was investigated to evaluate the necessary sinusoidal excitation and the frequencies at which significant nonlinearities are excited. Hereby, the amplitudes of higher harmonic responses were analysed in the overall frequency range. It was demonstrated that higher harmonics contain highly interesting and distinct nonlinear dynamic information. Characteristic nonlinearities are excited which can be correlated to Faradaic processes, such as electrode reactions, solid diffusion in particles and ionic transport processes between and in the SEI and electrolyte. Ionic transport processes between the SEI and the electrolyte show only minor nonlinear, respectively almost linear behaviour compared to the electrochemical reactions which follow nonlinear Butler-Volmer kinetics. Furthermore, it was demonstrated that characteristic frequency ranges of these processes are excited were distinguishable with NFRA, in

[1] Parts of this chapter have been published in [1–4].

cases where they were not distinguishable with EIS. This represents the clear advantage of NFRA in comparison to the state-of-the-art method of linear system analysis methods.

The results from Chapter 2 were extended with a sensitivity analysis of NFRA to measurement and cell parameters. SoC and temperature have a high impact on NFRA. Nonlinear responses are higher for high and low SoC in the sensitive frequency range and lower for increased measurement temperatures. Besides, parameters settings at the potentiostat have an impact on the quality of NFRA, i.e. excitation amplitude, oscillation number and data points measured per frequency decade. Concluding, measurement parameters and conditions have to be monitored and adapted precisely for quantitative and qualitative studies. With NFRA, high energy and high power cells can be differentiated, because typical Faradaic nonlinearities of the electrochemical reactions are excited at lower frequencies for high-energy cells in comparison to high-power cells. The results from Chapter 2 and 3 may be considered as a guideline in regard to reliable, reproducible dynamic analysis of LIBs using NFRA. Further, the results proof the applicability of NFRA on LIBs as an advanced dynamic analysis method.

In Chapter 4 and 5, the focus was laid on the one hand on aging diagnosis with NFRA and on the other hand on the investigation of different data evaluation approaches for SoH estimation using NFR data. Chapter 4 focused on the identification of the impact of different degradation effects on the highly sensitive nonlinearities. For this, cyclic aging at -10°C and 25°C was induced and its impact on NFRA and EIS was studied in combination with ex-situ techniques. At 25°C , higher harmonic amplitudes of Y_2 and Y_3 increased uniformly in the overall frequency range. However, a specific, quantitative increase of the third harmonic Y_3 was identified in the sensitive frequency range for electrochemical reactions and correlated to lithium plating via an ex-situ analysis. Only in the case of cyclic aging at -10°C , this distinct increase of the amplitude of Y_3 over the amplitude of Y_2 was found, indicating changes of the reactions kinetics of the electrochemical reactions at the anode due to plated lithium. These nonlinear findings were differentiated from the impact of cyclic aging at 25°C on NFRA which mainly were degradations at the SEI, as this characteristic intensity increase of Y_3 over Y_2 was not observed. Dynamic analysis with EIS, however, was not sufficient for this clear differentiation of aging effects as impedances of cells increased uniformly for cyclic aging at -10°C as well as at 25°C.

In Chapter 5, different approaches for the evaluation of NFRA aging data sets were

used to estimate and quantify the SoH of LIBs. In the first part, a case study using a data-mining approach based on SVR was derived from NFRA data sets. After performing a correlation analysis for the identification of the most aging-sensitive frequency range, informative NFRA data features were identified and used to parametrise the SVR model. The degradation algorithm was validated with NFRA test data sets of identical as well as not-identical LIBs. The degradation model predicted the SoH values with high accuracy. This prediction demonstrated the usefulness of NFRA as an effective and fast SoH identification method and as a versatile tool for aging diagnosis of LIBs.

In the second part of the chapter, a different approach for the SoH estimation based on NFRA aging data sets was evaluated. NFR measured at two excitation amplitudes of I_{AC} in the characteristic frequency range for the electrochemical reactions were correlated to the capacity fade due to loss of active material. Here, NFR data showed a good correlation to the capacity fade. Using a reaction model with an implementation of the electrode reaction due to Butler-Volmer kinetics, the experimental findings were verified. Simulations confirmed the experimentally identified correlation of the NFR data to the assumed aging mechanism. Overall, NFRA was identified as a reliable, easily measured and evaluated dynamic analysis method for process characterization and SoH estimation of LIBs.

6.2. Outlook

Within this work, the fundamentals for measurements and interpretation of NFRA studies on LIBs have been established. Future work should focus on a quantitative correlation of NFRA to characteristic aging phenomena, e.g. lithium plating, as well as the analysis of robustness of NFRA for aging diagnosis in comparison to other measurement methods, such as ICA and DVA. Concerning the data-driven quantification of the SoH of LIBs, NFRA data sets of commercial cells and the impact of changes in the measurement scenarios, such as temperature variations as well as aging conditions, on the data-based SoH identification should be taken into account.

So far, the focus was on NFRA of LIBs in the full-cell format with state-of-the-art anodes, cathodes, electrolytes and separators. An unexploited topic is the comparison of NFRA on LIBs in full- and half-cell design for various SoCs and temperatures to separate the individual impact of anode and cathode on full-cell NFR spectra. Another

interesting research topic could be the analysis of the impact of different electrolytes as well as separators on NFRA. Generally, NFRA significantly extends the possibilities of dynamic analysis of batteries and should be further investigated for more types, sizes and states of batteries. As well unexploited is the application of NFRA to next generation battery technologies, such as All-Solid-State Batteries. Nonlinear characteristics of such battery types could be investigated and compared to the results of this work as a benchmark. Besides, a great achievement would be the alignment of NFRA simulations and experiments to perform a simulation-based parameter identification of NFRA. The simulative verification of the experimental findings with a battery model regarding the dependency of NFRA on measurement conditions, such as temperature and SoC, would be of high relevance to further strengthen the methodology.

Summarizing the results, this thesis demonstrates that NFRA is a promising advanced dynamic method for in-depth process characterization, aging diagnosis and SoH estimation of LIBs. A future vision would be the establishment of NFRA as a regularly used, state-of-the-art dynamic analysis application for LIBs, comparable to the established EIS.

Appendix A

Guideline for NFRA with Zahner-elektrik Potentiostat

In this work, a Zahner-elektrik Electrochemical Workstation (Zennium model) in combination with a power potentiostat (PP241 model) was used for NFRA measurements. The main device specifications of the Zennium and the PP241 are listed in table A.1. As NFRA is measured in the galvanostatic modus, the specifications of the sinusoidal input current and the sinusoidal output voltage are given. More detailed specifications are provided on the homepage of Zahner-elektrik [74].[1]

Measurements

With Zahner-elektrik potentiostats it is possible to measure in a two-electrode, three-electrode or four-electrode set-up. In this work, the two-electrode set-up was used for all measurements. The working electrode is always the black cable, the working sense electrode is the blue cable, the counter electrode is the red cable and the reference electrode is the green cable. For the two-electrode set-up, the blue cable is plugged into the black cable and the green one is plugged into the the red cable. The black, respectively red cable is connected to the working, respectively counter electrode.
LIBs can be measured in a two or four point two-electrode set-up. A picture of a four point measurement with the Zahner device is shown in Figure A.1. Here, the black and blue, respectively red and green cables are not plugged into each other for the measurement, but are connected separately to the corresponding deflector of the battery electrode. Thereby, current and voltage are measured at different points of the deflector and the accuracy of the measurements may be increased even more.

[1] http://zahner.de/

Type	Parameter	Zennium	PP241
Input AC	Amplitude	± 100 pA to ± 2.5 A in 30 steps	0 A to ± 40 A in 30 steps
	Accuracy	0.05% @ ≥ 2 μA to 100 mA 0.5% @ <2 μ A or > 100 mA	±0.25%/±1 mA
	Resolution	16 aA	/
	Frequency range	10μ Hz to 4 MHz	10μHz to 200 kHz
Output AV	Amplitude	Main: ±1,±2,±4 V U-Buffer: ±4,±10 V	± 5 V
	Accuracy	Main: ±250 μV U-Buffer: ±1 mV	±0.1 %/± 1 mV
	Resolution	Main: ±125 μV U-Buffer: ±320μ V	/
	Frequency range	10 μHz to 4 MHz	10 μHz to 200 kHz

Table A.1.: Important specifications of the Zennium potentiostat and the PP241 [74].

This impact increases, if low impedance battery cells are measured. Measurements in this work are performed in a four point two-electrode set-up and the connectors are placed in an angle of 180° on the deflector, if possible. In general, the cable connection has to be similar for every measurement to guarantee comparability of measurement results.

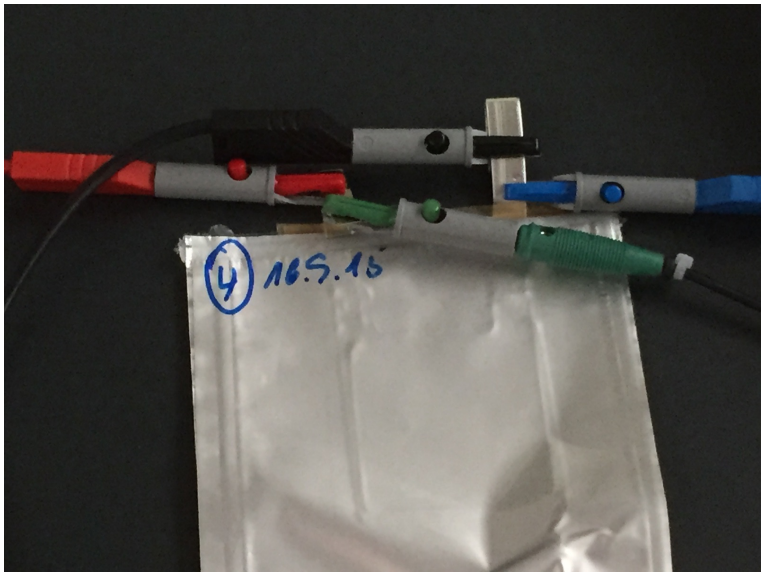

Figure A.1.: Cell cable connections for dynamic measurements with the Zennium potentiostat.

Settings

NFRA is measured in addition to a standard EIS measurement. Settings in the Zahner software Thales USB are adapted via the so called "Helping Hippo". The extended

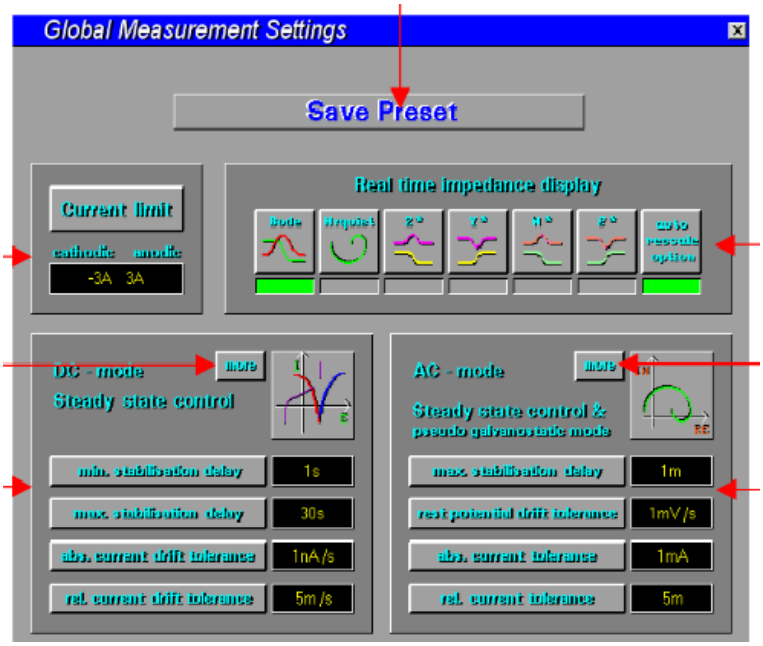

Figure A.2.: Settings in the software for measuring NFRA and EIS with the Zennium potentiostat.

settings of the AC-mode have to be set in the following way: clicking on "more" of the AC-mode, shown in Figure A.2, opens additional settings, shown in Figure A.3. In this window, the Z-outputflag has to be set to 1 to disable abortion of the impedance measurement, if noise in the measurement signal is measured. Further, the logfile entry has to be set to 2 to measure the amplitudes of higher harmonics. Amplitudes of the higher harmonics Y_n are weighted on the amplitudes of the fundamental harmonic Y_1 by the device. The normalized amplitudes Y_n/Y_1 for n $\geq$2 to 10 are provided in the output file.[2]

Excursus: Setting of Oscillation Number

Zahner-elektrik provided information exclusively to the InES about settings for analysis of a variation of the number of input oscillations n_ν. This workaround has been given as temporary solution via telephone and cannot be found in the manual. Generally, devices for AC measurements discard the first oscillation. Due to the continuous modulation of frequencies, the first oscillation at each frequency may contain

[2] A detailed description of the evaluation of NFRA data is given at the end of the Appendix.

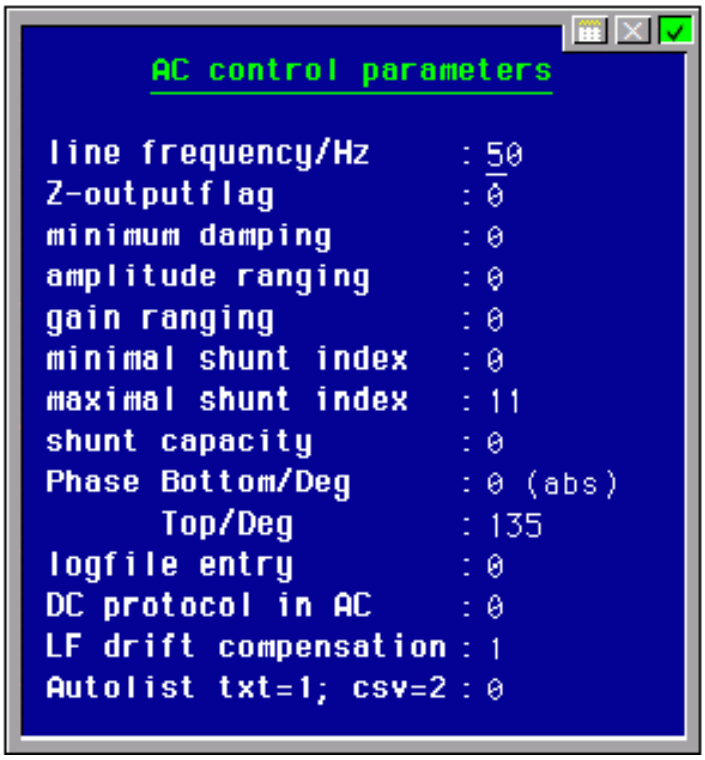

Figure A.3.: Extended AC settings of the Zahner software Thales USB for enabling measurement of NFRA.

distortions of the previously modulated frequency. Thus, the first oscillation is discarded per default. Dynamic analysis starts with the first "clean" oscillation at each frequency which is modulated secondly. The following steps have to be taken to set the oscillation number: First, the EIS set-up menu is interrupted with F12. Then, the number of the oscillations which should be discarded prior to measuring EIS/NFRA is set. Default setting is 1. The oscillation is entitled in the software as N_v. If two oscillations should be discarded prior to dynamic measurements, "N_v=2" is entered in the blank line. Any integer number can be set. However, it is not possible to set 0. If 0 is set, the software is aborted and the device turns down. After setting of N_v, Shift and F6 have to be pressed simultaneously to return to the standard EIS set-up menu. For verification of the changed value of N_v, the EIS program is interrupted, again, via F12. Now, "?" is entered in the blank line and ENTER is pressed. The new value of N_v appears. One can return to the standard EIS set-up menu via pressing Shift and F6 simultaneously. Now, EIS/NFRA measurements with changed input oscillation number can be performed. If the device is turned off, settings return to the default values.

Evaluation

Potentiostats of Zahner-elektrik are built for the generation of a clean sinusoidal signal. To achieve this, the signal of the frequency generator is filtered before it is transmitted to the test object. However, the sinusoidal input signal may contain slight amplitudes of higher harmonic distortions. Overall, the output signal thus can contain the following information:

a) Amplitudes of higher harmonics of the test object excited by the fundamental harmonic of the excitation signal

b) Amplitudes of higher harmonics of the test object excited by higher harmonics already present in the excitation signal

c) Amplitudes of higher harmonics in the excitation signal

Raw data of the output signal are corrected by the device. Amplitudes of higher harmonics in the excitation signal are subtracted from the raw data. Physically this correction is not valid, as there can be a phase shift between the complex excitation signal and the complex output signal. If the test object shows only Ohmic behavior, no phase shift will be between the input and the output signal. The phase shift of batteries and fuel cells is typically smaller than 15°. As well, the amplitude of the higher harmonics in the excitation signal are several magnitudes lower than the fundamental amplitude. Consequently, the proportion of higher harmonics in the output signal, excited by the distortions of the input signal, will be even smaller. Therefore, the compensation method used by Zahner-elektrik is a good approximation and an improvement compared to evaluating the raw data without any correction.

Three data sets are provided by the device in the data output file (Figure A.4):

a) Higher harmonic amplitudes in the excitation signal (“excit”)

b) Raw data of the output signal (“response”)

c) Higher harmonics responses of the test object which are corrected by higher harmonics of the excitation signal (“normalized”)

Noise values are provided for frequencies <66 Hz. All higher harmonic values are weighted to the fundamental harmonic, as previously described. In Equation A.1, the calculation formula for the data correction is given. As the device provides higher harmonic intensities normalized to the fundamental harmonic Y_1, the output values have to be multiplied by Y_1 to get the pure and not normalized intensities of higher harmonics Y_n.

$$Y_n / Y_1 = Y_{n,response} / Y_1 - Y_{n,excit} / Y_1 \tag{A.1}$$

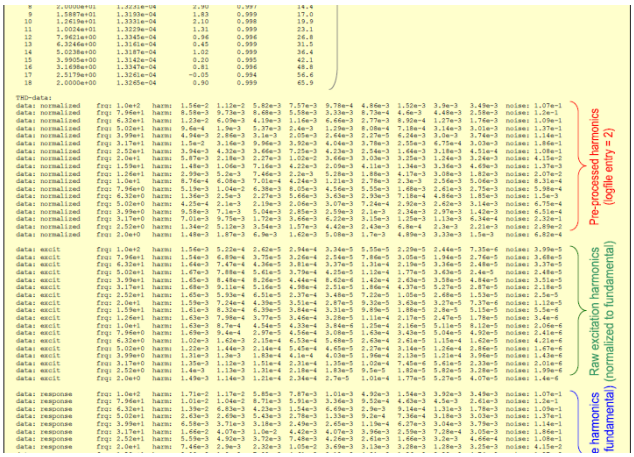

Figure A.4.: Exemplary data output file of the Zahner potentiostat [74].

Y_1 is calculated from the impedance data measured at $I_{AC,NFRA}$:

$$Y_1 = \sqrt{Re(Z)^2 + Im(Z)^2} \cdot I_{AC,NFRA} \tag{A.2}$$

Bibliography

[1] N. Harting, N. Wolff, F. Röder, and U. Krewer, "Nonlinear Frequency Response Analysis (NFRA) of Lithium-Ion Batteries," *Electrochimica Acta*, vol. 248, pp. 133–139, 2017.

[2] N. Harting, N. Wolff, and U. Krewer, "Identification of Lithium Plating in Lithium-Ion Batteries using Nonlinear Frequency Response Analysis (NFRA)," *Electrochimica Acta*, vol. 281, pp. 378–385, 2018.

[3] N. Harting, R. Schenkendorf, N. Wolff, and U. Krewer, "State-of-Health Identification of Lithium-Ion Batteries Based on Nonlinear Frequency Response Analysis: First Steps with Machine Learning," *Applied Sciences*, vol. 8, no. 5, p. 821, 2018.

[4] N. Harting, N. Wolff, F. Röder, and U. Krewer, "State-of-Health Diagnosis of Lithium-Ion Batteries Using Nonlinear Frequency Response Analysis," *Journal of The Electrochemical Society*, vol. 166, no. 2, pp. A277–A285, 2019.

[5] J.-M. Tarascon, "From Li–Ion to Na–Ion: What to Expect," *9th International Advanced Automotive Batteries Europe*, January 2019.

[6] Q. Mao, U. Krewer, and R. Hanke-Rauschenbach, "Total Harmonic Distortion Analysis for Direct Methanol Fuel Cell Anode," *Electrochemistry Communications*, vol. 12, no. 11, pp. 1517–1519, 2010.

[7] Q. Mao and U. Krewer, "Sensing Methanol Concentration in Direct Methanol Fuel Cell with Total Harmonic Distortion: Theory and Application," *Electrochimica Acta*, vol. 68, pp. 60–68, 2012.

[8] M. Nie and B. L. Lucht, "Role of Lithium Salt on Solid Electrolyte Interface (SEI) Formation and Structure in Lithium Ion Batteries," *Journal of the Electrochemical Society*, vol. 161, no. 6, pp. A1001–A1006, 2014.

[9] M. D. Levi and D. Aurbach, "The Mechanism of Lithium Intercalation in Graphite Film Electrodes in Aprotic Media. Part 1. High Resolution Slow Scan Rate Cyclic Voltammetric Studies and Modeling," *Journal of Electroanalytical Chemistry*, vol. 421, no. 1-2, pp. 79–88, 1997.

[10] N. A. Wolff, "Implementierung und Erweiterung eines elektrochemischen Modells zur Charakterisierung von Lithium-Ionen-Zellen," *Technische Universität Braunschweig*, 2014. Studienarbeit.

[11] G. Berckmans, M. Messagie, J. Smekens, N. Omar, L. Vanhaverbeke, and J. V. Mierlo, "Cost Projection of State of the Art Lithium-Ion Batteries for Electric Vehicles up to 2030," *Energies*, vol. 10, no. 9, p. 1314, 2017.

[12] N. Nitta, F. Wu, J. T. Lee, and G. Yushin, "Li-Ion Battery Materials: Present and Future," *Materials Today*, vol. 18, no. 5, pp. 252–264, 2015.

[13] M. Winter, J. O. Besenhard, M. E. Spahr, and P. Novak, "Insertion Electrode Materials for Rechargeable Lithium Batteries," *Advanced materials*, vol. 10, no. 10, pp. 725–763, 1998.

[14] V. A. Agubra and J. W. Fergus, "Lithium Ion Battery Anode Aging Mechanisms," *Materials*, vol. 6, pp. 1310–1325, 2013.

[15] K. Zaghib, M. Dontigny, A. Guerfi, P. Charest, I. Rodrigues, A. Mauger, and C. M. Julien, "Safe and Fast-Charging Li-Ion Battery with Long Shelf Life for Power Applications," *Journal of Power Sources*, vol. 196, no. 8, pp. 3949–3954, 2011.

[16] D. Anseán, M. Dubarry, A. Devie, B. Y. Liaw, V. M. García, J. C. Viera, and M. González, "Fast Charging Technique for High Power $LiFePO_4$ Batteries: A Mechanistic Analysis of Aging," *Journal of Power Sources*, vol. 321, pp. 201–209, 2016.

[17] J. Vetter, P. Novak, M. Wagner, and C. Veit, "Ageing Mechanisms in Lithium-Ion Batteries," *Journal of Power Sources*, vol. 147, no. 1-2, pp. 269–281, 2005.

[18] A. Barré, B. Deguilhem, S. Grolleau, M. Gérard, F. Suard, and D. Riu, "A Review on Lithium-Ion Battery Ageing Mechanisms and Estimations for Automotive Applications," *Journal of Power Sources*, vol. 241, pp. 680–689, 2013.

[19] M. Fleischhammer, T. Waldmann, G. Bisle, B.-I. Hogg, and M. Wohlfahrt-Mehrens, "Interaction of Cyclic Ageing at High-Rate and Low Temperatures and Safety in Lithium-Ion Batteries," *Journal of Power Sources*, vol. 274, pp. 432–439, 2015.

[20] C. Wu, C. Zhu, Y. Ge, and Y. Zhao, "A Review on Fault Mechanism and Diagnosis Approach for Li-Ion Batteries," *Journal of Nanomaterials*, vol. 2015, pp. 1–9, 2015.

[21] M. Lewerenz, A. Marongiu, A. Warnecke, and D. U. Sauer, "Differential Voltage Analysis as a Tool for Analyzing Inhomogeneous Aging: A Case Study for $LiFePO_4$| Graphite Cylindrical Cells," *Journal of Power Sources*, vol. 368, pp. 57–67, 2017.

[22] D. Aurbach, B. Markovsky, I. Weissman, E. Levi, and Y. Ein-Eli, "On the Correlation between Surface Chemistry and Performance of Graphite Negative Electrodes for Li Ion Batteries," *Electrochimica Acta*, vol. 45, no. 1, pp. 67–86, 1999.

[23] P. Verma, P. Maire, and P. Novák, "A Review of the Features and Analyses of the Solid Electrolyte Interphase in Li-Ion Batteries," *Electrochimica Acta*, vol. 55, no. 22, pp. 6332–6341, 2010.

[24] V. A. Agubra, J. W. Fergus, R. Fu, and S.-Y. Choe, "Analysis of Effects of the State of Charge on the Formation and Growth of the Deposit Layer on Graphite Electrode of Pouch Type Lithium Ion Polymer Batteries," *Journal of Power Sources*, vol. 270, no. 4, pp. 213–220, 2014.

[25] M. Petzl, M. Kasper, and M. a. Danzer, "Lithium Plating in a Commercial Lithium-Ion Battery – A Low-Temperature Aging Study," *Journal of Power Sources*, vol. 275, pp. 799–807, 2014.

[26] T. Waldmann, B.-I. Hogg, and M. Wohlfahrt-Mehrens, "Li Plating as Unwanted Side Reaction in Commercial Li-Ion Cells–A Review," *Journal of Power Sources*, vol. 384, pp. 107–124, 2018.

[27] C. Lin, A. Tang, H. Mu, W. Wang, and C. Wang, "Aging Mechanisms of Electrode Materials in Lithium-Ion Batteries for Electric Vehicles," vol. 2015, pp. 1–18, 2015.

[28] S. Schindler, M. Bauer, M. Petzl, and M. A. Danzer, "Voltage Relaxation and Impedance Spectroscopy as In-Operando Methods for the Detection of Lithium Plating on Graphitic Anodes in Commercial Lithium-Ion Cells," *Journal of Power Sources*, vol. 304, pp. 170–180, 2016.

[29] Q. Liu, C. Du, B. Shen, P. Zuo, X. Cheng, Y. Ma, G. Yin, and Y. Gao, "Understanding Undesirable Anode Lithium Plating Issues in Lithium-Ion Batteries," *RSC Adv.*, vol. 6, no. 91, pp. 88683–88700, 2016.

[30] Y. Wang, R. Pan, D. Yang, X. Tang, and Z. Chen, "Remaining Useful Life Prediction of Lithium-ion Battery Based on Discrete Wavelet Transform," *Energy Procedia*, vol. 105, pp. 2053–2058, 2017.

[31] M. Dubarry, V. Svoboda, R. Hwu, and B. Yann Liaw, "Incremental Capacity Analysis and Close-to-Equilibrium OCV Measurements to Quantify Capacity Fade in Commercial Rechargeable Lithium Batteries," *Electrochemical and Solid-State Letters*, vol. 9, no. 10, pp. A454–A457, 2006.

[32] T. Waldmann, A. Iturrondobeitia, M. Kasper, N. Ghanbari, F. Aguesse, E. Bekaert, L. Daniel, S. Genies, I. J. Gordon, M. W. Löble, E. De Vito, and M. Wohlfahrt-Mehrens, "Review—Post-Mortem Analysis of Aged Lithium-Ion Batteries: Disassembly Methodology and Physico-Chemical Analysis Techniques," *Journal of The Electrochemical Society*, vol. 163, no. 10, pp. A2149–A2164, 2016.

[33] C. Pastor-Fernández, K. Uddin, G. H. Chouchelamane, W. D. Widanage, and J. Marco, "A Comparison between Electrochemical Impedance Spectroscopy and Incremental Capacity-Differential Voltage as Li-ion Diagnostic Techniques to Identify and Quantify the Effects of Degradation Modes within Battery Management Systems," *Journal of Power Sources*, vol. 360, pp. 301–318, 2017.

[34] M. H. Hung, C. H. Lin, L. C. Lee, and C. M. Wang, "State-of-Charge and State-of-Health Estimation for Lithium-Ion Batteries based on Dynamic Impedance Technique," *Journal of Power Sources*, vol. 268, pp. 861–873, 2014.

[35] D. André, M. Meiler, K. Steiner, C. Wimmer, T. Soczka-Guth, and D. U. Sauer, "Characterization of High-Power Lithium-ion Batteries by Electrochemical Impedance Spectroscopy. I. Experimental Investigation," *Journal of Power Sources*, vol. 196, no. 12, pp. 5334–5341, 2011.

[36] T. Osaka, D. Mukoyama, and H. Nara, "Review—Development of Diagnostic Process for Commercially Available Batteries, Especially Lithium Ion Battery, by Electrochemical Impedance Spectroscopy," *Journal of The Electrochemical Society*, vol. 162, no. 14, pp. A2529–A2537, 2015.

[37] N. Xu and D. J. Riley, "Nonlinear Analysis of a Classical System: The Faradaic Process," *Electrochimica Acta*, vol. 94, pp. 206–213, 2013.

[38] A. M. Bond, N. W. Duffy, D. M. Elton, and B. D. Fleming, "Characterization of Nonlinear Background Components in Voltammetry by use of Large Amplitude Periodic Perturbations and Fourier Transform Analysis," *Analytical Chemistry*, vol. 81, no. 21, pp. 8801–8808, 2009.

[39] N. Legrand, S. Raël, B. Knosp, M. Hinaje, P. Desprez, and F. Lapicque, "Including Double-Layer Capacitance in Lithium-Ion Battery Mathematical Models," *Journal of Power Sources*, vol. 251, pp. 370–378, 2014.

[40] N. Wolff, N. Harting, M. Heinrich, F. Röder, and U. Krewer, "Nonlinear Frequency Response Analysis on Lithium-Ion Batteries: A Model-Based Assessment," *Electrochimica Acta*, vol. 260, pp. 614–622, 2017.

[41] F. Gao and Z. Tang, "Kinetic Behavior of LiFePO4/C Cathode Material for Lithium-Ion Batteries," *Electrochimica Acta*, vol. 53, no. 15, pp. 5071–5075, 2008.

[42] J. R. Macdonald and E. Barsoukov, *Impedance Spectroscopy: Theory, Experiment, and Applications*. John Wiley & Sons, 2005.

[43] A. Lasia, "Electrochemical Impedance Spectroscopy and its Applications," in *Modern Aspects of Electrochemistry*, pp. 143–248, Springer, 2002.

[44] D. K. Kampouris, X. Ji, E. P. Randviir, and C. E. Banks, "A New Approach for the Improved Interpretation of Capacitance Measurements for Materials Utilised in Energy Storage," *RSC Advances*, vol. 5, no. 17, pp. 12782–12791, 2015.

[45] D. Le and X. Tang, "Lithium-Ion Battery State of Health Estimation Using Ah-V Characterization," *Annual Conference of the Prognostics and Health Management Society*, 2011.

[46] J. Jiang, Z. Lin, Q. Ju, Z. Ma, C. Zheng, and Z. Wang, "Electrochemical Impedance Spectra for Lithium-ion Battery Ageing considering the Rate of Discharge Ability," *Energy Procedia*, vol. 105, pp. 844–849, 2017.

[47] J. Schmitt, A. Maheshwari, M. Heck, S. Lux, and M. Vetter, "Impedance Change and Capacity Fade of Lithium Nickel Manganese Cobalt Oxide-Based Batteries during Calendar Aging," *Journal of Power Sources*, vol. 353, pp. 183–194, 2017.

[48] U. Tröltzsch, O. Kanoun, and H.-R. Tränkler, "Characterizing Aging Effects of Lithium Ion Batteries by Impedance Spectroscopy," *Electrochimica Acta*, vol. 51, no. 8-9, pp. 1664–1672, 2006.

[49] E. Ivers-Tiffée and A. Weber, "Evaluation of Electrochemical Impedance Spectra by the Distribution of Relaxation Times," *Journal of the Ceramic Society of Japan*, vol. 125, no. 4, pp. 193–201, 2017.

[50] P. S. Sabet, G. Stahl, and D. U. Sauer, "Non-Invasive Investigation of Predominant Processes in the Impedance Spectra of High Energy Lithium-Ion Batteries with Nickel-Cobalt-Aluminum Cathodes," *Journal of Power Sources*, vol. 406, pp. 185–193, 2018.

[51] H. Schichlein, A. C. Müller, M. Voigts, A. Krügel, and E. Ivers-Tiffée, "Deconvolution of Electrochemical Impedance Spectra for the Identification of Electrode Reaction Mechanisms in Solid Oxide Fuel Cells," *Journal of Applied Electrochemistry*, vol. 32, no. 8, pp. 875–882, 2002.

[52] T. P. Heins, N. Schlüter, and U. Schröder, "Electrode-Resolved Monitoring of the Ageing of Large-Scale Lithium-Ion Cells by using Electrochemical Impedance Spectroscopy," *ChemElectroChem*, vol. 4, no. 11, pp. 2921–2927, 2017.

[53] B. Manikandan, V. Ramar, C. Yap, and P. Balaya, "Investigation of Physico-Chemical Processes in Lithium-Ion Batteries by Deconvolution of Electrochemical Impedance Spectra," *Journal of Power Sources*, vol. 361, pp. 300–309, 2017.

[54] M. Steinhauer, S. Risse, N. Wagner, and K. A. Friedrich, "Investigation of the Solid Electrolyte Interphase Formation at Graphite Anodes in Lithium-Ion Batteries with Electrochemical Impedance Spectroscopy," *Electrochimica Acta*, vol. 228, pp. 652–658, 2017.

[55] G. E. Mog and E. P. Ribeiro, "Total Harmonic Distortion Calculation by Filtering for Power Quality Monitoring," in *Transmission and Distribution Conference and Exposition*, IEEE, 2004.

[56] S. Okazaki, "Second-Order Harmonic in the Current Response to Sinusoidal Perturbation Voltage for Lead-Acid Battery," *Journal of The Electrochemical Society*, vol. 132, no. 7, pp. 1516–1520, 1985.

[57] Q. Mao and U. Krewer, "Total Harmonic Distortion Analysis of Oxygen Reduction Reaction in Proton Exchange Membrane Fuel Cells," *Electrochimica Acta*, vol. 103, pp. 188–198, 2013.

[58] E. Ramschak, V. Peinecke, P. Prenninger, T. Schaffer, W. Baumgartner, and V. Hacker, "Online Stack Monitoring Tool for Dynamically and Stationary Operated Fuel Cell Systems," *Fuel Cells Bulletin*, no. 10, pp. 12–15, 2006.

[59] T. Kadyk, R. Hanke-Rauschenbach, and K. Sundmacher, "Nonlinear Frequency Response Analysis of PEM Fuel Cells for Diagnosis of Dehydration, Flooding and CO-Poisoning," *Journal of Electroanalytical Chemistry*, vol. 630, no. 1-2, pp. 19–27, 2009.

[60] J. J. Giner-Sanz, E. M. Ortega, and V. Pérez-Herranz, "Total Harmonic Distortion Based Method for Linearity Assessment in Electrochemical Systems in the context of EIS," *Electrochimica Acta*, vol. 186, pp. 598–612, 2015.

[61] M. Kiel, O. Bohlen, and D. U. Sauer, "Harmonic Analysis for Identification of Nonlinearities in Impedance Spectroscopy," *Electrochimica Acta*, vol. 53, no. 25, pp. 7367–7374, 2008.

[62] D. K. Y. Wong and D. R. Macfarlane, "Harmonic Impedance Spectroscopy. Theory and Experimental Results for Reversible and Quasi-Reversible Redox Systems," vol. 99, no. 7, pp. 2134–2142, 1995.

[63] J. R. Wilson, D. T. Schwartz, and S. B. Adler, "Nonlinear Electrochemical Impedance Spectroscopy for Solid Oxide Fuel Cell Cathode Materials," *Electrochimica Acta*, vol. 51, no. 8-9, pp. 1389–1402, 2006.

[64] K. Darowicki and J. Majewska, "Harmonic Analysis of Electrochemical and Corrosion Systems - A Review," *Corrosion Reviews*, vol. 17, no. 5, pp. 383–399, 1999.

[65] L. Meszaros, "Application of Harmonic Analysis in the Measuring Technique of Corrosion," *Journal of The Electrochemical Society*, vol. 141, no. 8, pp. 2068–2071, 1994.

[66] W. M. Grady and S. Santoso, "Understanding Power System Harmonics," *IEEE Power Engineering Review*, vol. 21, no. 11, pp. 8–11, 2001.

[67] N. Xu and J. Riley, "Nonlinear analysis of a classical system: The double-layer capacitor," *Electrochemistry Communications*, vol. 13, no. 10, pp. 1077–1081, 2011.

[68] M. D. Murbach and D. T. Schwartz, "Extending Newman's Pseudo-Two-Dimensional Lithium-Ion Battery Impedance Simulation Approach to Include the Nonlinear Harmonic Response," *Journal of The Electrochemical Society*, vol. 164, no. 11, pp. E3311–E3320, 2017.

[69] M. D. Murbach, V. W. Hu, and D. T. Schwartz, "Nonlinear Electrochemical Impedance Spectroscopy of Lithium-Ion Batteries: Experimental Approach, Analysis, and Initial Findings," *Journal of The Electrochemical Society*, vol. 165, no. 11, pp. A2758–A2765, 2018.

[70] N. Wolff, N. Harting, M. Heinrich, and U. Krewer, "Nonlinear Frequency Response Analysis on Lithium-Ion Batteries: Process Identification and Differences Between Transient and Steady-State Behavior," *Electrochimica Acta*, vol. 298, pp. 788–798, 2019.

[71] N. Wolff, N. Harting, M. Heinrich, F. Röder, and U. Krewer, "Understanding Nonlinearity in Electrochemical Systems," *European Physical Journal.* accepted.

[72] V. V. Panić and T. R. Vidaković, "Nonlinear Frequency Response Analysis of the Ferrocyanide Oxidation Kinetics . Part II . Measurement Routine and Experimental Validation," vol. 115, no. 35, pp. 17352–17358, 2011.

[73] G. Sikha, B. N. Popov, and R. E. White, "Effect of Porosity on the Capacity Fade of a Lithium-Ion Battery," *Journal of The Electrochemical Society*, vol. 151, no. 7, pp. A1104–A1114, 2004.

[74] Zahner-elektrik, "Electrochemical Impedance Sepctroscopy," October 2018. http://zahner.de/pdf/EIS, retrieved on 5*th* February 2019.

[75] K. Onda, H. Kameyama, T. Hanamoto, and K. Ito, "Experimental Study on Heat Generation Behavior of Small Lithium-Ion Secondary Batteries," *Journal of The Electrochemical Society*, vol. 150, pp. A285–A291, 2003.

[76] K. Uddin, A. D. Moore, A. Barai, and J. Marco, "The Effects of High Frequency Current Ripple on Electric Vehicle Battery Performance," *Applied Energy*, vol. 178, pp. 142–154, 2016.

[77] K. Uddin, L. Somerville, A. Barai, M. Lain, T. R. Ashwin, P. Jennings, and J. Marco, "The Impact of High-Frequency-High-Current Perturbations on Film Formation at the Negative Electrode-Electrolyte Interface," *Electrochimica Acta*, vol. 233, pp. 1–12, 2017.

[78] T. Waldmann, M. Wilka, M. Kasper, M. Fleischhammer, and M. Wohlfahrt-Mehrens, "Temperature Dependent Ageing Mechanisms in Lithium-Ion Batteries - A Post-Mortem Study," *Journal of Power Sources*, vol. 262, pp. 129–135, 2014.

[79] T. Momma, M. Matsunaga, D. Mukoyama, and T. Osaka, "AC Impedance Analysis of Lithium Ion Battery under Temperature Control," *Journal of Power Sources*, vol. 216, pp. 304–307, 2012.

[80] H. Budde-Meiwes, J. Kowal, D. U. Sauer, and E. Karden, "Influence of Measurement Procedure on Quality of Impedance Spectra on Lead-Acid Batteries," *Journal of Power Sources*, vol. 196, no. 23, pp. 10415–10423, 2011.

[81] Q. Zhong, B. Huang, J. Ma, and H. Li, "Experimental Study on Relationship Between SOC and OCV of Lithium-Ion Batteries," *International Journal of Smart Grid and Clean Energy*, vol. 3, no. 2, pp. 149–153, 2014.

[82] J. Zhang, H. Ge, Z. Li, and Z. Ding, "Internal Heating of Lithium-Ion Batteries Using Alternating Current Based on the Heat Generation Model in Frequency Domain," *Journal of Power Sources*, vol. 273, pp. 1030–1037, 2015.

[83] F. Jiang, P. Peng, and Y. Sun, "Thermal Analyses of $LiFePO_4$/Graphite Battery Discharge Processes," *Journal of Power Sources*, vol. 243, pp. 181–194, 2013.

[84] A. Farmann and D. U. Sauer, "A Study on the Dependency of the Open-Circuit Voltage on Temperature and Actual Aging State of Lithium-Ion Batteries," *Journal of Power Sources*, vol. 347, pp. 1–13, 2017.

[85] J. B. Gerschler and D. U. Sauer, "Investigation of Open-Circuit-Voltage Behaviour of Lithium-ion Batteries with various Cathode Materials under spe-

cial Consideration of Voltage Equalisation Phenomena," in *EVS24 International Battery, Hybrid and Fuel Cell Electric Vehicle Symposium*, 2009.

[86] Z. Li, J. Huang, B. Yann Liaw, V. Metzler, and J. Zhang, "A Review of Lithium Deposition in Lithium-Ion and Lithium Metal Secondary Batteries," *Journal of Power Sources*, vol. 254, pp. 168–182, 2014.

[87] S. F. Schuster, T. Bach, E. Fleder, J. Müller, M. Brand, G. Sextl, and A. Jossen, "Nonlinear Aging Characteristics of Lithium-Ion Cells Under Different Operational Conditions," *Journal of Energy Storage*, vol. 1, pp. 44–53, 2015.

[88] L. Somerville, J. Bareño, S. Trask, P. Jennings, A. McGordon, C. Lyness, and I. Bloom, "The Effect of Charging Rate on the Graphite Electrode of Commercial Lithium-Ion Cells: A Post-Mortem Study," *Journal of Power Sources*, vol. 335, pp. 189–196, 2016.

[89] M. Petzl and M. A. Danzer, "Nondestructive Detection, Characterization, and Quantification of Lithium Plating in Commercial Lithium-In Batteries," *Journal of Power Sources*, vol. 254, pp. 80–87, 2014.

[90] B. Bitzer and A. Gruhle, "A New Method for Detecting Lithium Plating by Measuring the Cell Thickness," *Journal of Power Sources*, vol. 262, pp. 297–302, 2014.

[91] C. Uhlmann, J. Illig, M. Ender, R. Schuster, and E. Ivers-Tiffée, "In Situ Detection of Lithium Metal Plating on Graphite in Experimental Cells," *Journal of Power Sources*, vol. 279, pp. 428–438, 2015.

[92] F. Sagane, R. Shimokawa, H. Sano, H. Sakaebe, and Y. Iriyama, "In-Situ Scanning Electron Microscopy Observations of Li Plating and Stripping Reactions at the Lithium Phosphorus Oxynitride Glass Electrolyte/Cu Interface," *Journal of Power Sources*, vol. 225, pp. 245–250, 2013.

[93] J. C. Burns, D. a. Stevens, and J. R. Dahn, "In-Situ Detection of Lithium Plating Using High Precision Coulometry," *Journal of the Electrochemical Society*, vol. 162, no. 6, pp. A959–A964, 2015.

[94] C. R. Birkl, M. R. Roberts, E. McTurk, P. G. Bruce, and D. A. Howey, "Degradation Diagnostics for Lithium Ion Cells," *Journal of Power Sources*, vol. 341, pp. 373–386, 2017.

[95] W. Waag, C. Fleischer, and D. U. Sauer, "Critical Review of the Methods for Monitoring of Lithium-Ion Batteries in Electric and Hybrid Vehicles," *Journal of Power Sources*, vol. 258, pp. 321–339, 2014.

[96] A. Devie, M. Dubarry, and B. Y. Liaw, "Overcharge Study in $Li_4Ti_5O_{12}$ Based Lithium-Ion Pouch Cell I. Quantitative Diagnosis of Degradation Modes," *Journal of The Electrochemical Society*, vol. 162, no. 6, pp. A1033–A1040, 2015.

[97] M. Lewerenz, A. Warnecke, and D. U. Sauer, "Introduction of Capacity Difference Analysis (CDA) for Analyzing Lateral Lithium-Ion Flow to determine the State of Covering Layer Evolution," *Journal of Power Sources*, vol. 354, pp. 157–166, 2017.

[98] C. Sbarufatti, M. Corbetta, M. Giglio, and F. Cadini, "Adaptive Prognosis of Lithium-Ion Batteries Based on the Combination of Particle Filters and Radial Basis Function Neural Networks," *Journal of Power Sources*, vol. 344, pp. 128–140, 2017.

[99] D. Yang, Y. Wang, R. Pan, R. Chen, and Z. Chen, "A neural Network Based State-of-Health Estimation of Lithium-Ion Battery in Electric Vehicles," *Energy Procedia*, vol. 105, pp. 2059–2064, 2016.

[100] H. Dong, X. Jin, Y. Lou, and C. Wang, "Lithium-Ion Battery State of Health Monitoring and Remaining Useful Life Prediction based on Support Vector Regression-Particle Filter," *Journal of Power Sources*, vol. 271, pp. 114–123, 2014.

[101] S. Panchal, J. Mcgrory, J. Kong, R. Fraser, M. Fowler, I. Dincer, and M. Agelin-Chaab, "Cycling Degradation Testing and Analysis of a $LiFePO_4$ Battery at actual conditions," *International Journal of Energy Research*, vol. 41, no. 15, pp. 2565–2575, 2017.

[102] M. Ye, H. Guo, R. Xiong, and R. Yang, "Model-based State-of-charge Estimation Approach of the Lithium-Ion Battery Using an Improved Adaptive Particle Filter," *Energy Procedia*, vol. 103, pp. 394–399, 2016.

[103] Y. Wang, D. Yang, X. Zhang, and Z. Chen, "Probability Based Remaining Capacity Estimation Using Data-Driven and Neural Network Model," *Journal of Power Sources*, vol. 315, pp. 199–208, 2016.

[104] J. D. Gibbons and S. Chakraborti, "Nonparametric Statistical Inference," in *International encyclopedia of statistical science*, pp. 977–979, Springer, 2011.

[105] A. Jovic, K. Brkic, and N. Bogunovic, "A Review of Feature Selection Methods with Applications," in *38th International Convention on Information and Communication Technology, Electronics and Microelectronics (MIPRO)*, 2015.

[106] J. G. Dy and C. E. Brodley, "Feature Selection for Unsupervised Learning," *Journal of Machine Learning Research*, vol. 5, pp. 845–889, 2004.

[107] T.-C. Fu, "A Review on Time Series Data Mining," *Engineering Applications of Artificial Intelligence*, vol. 24, no. 1, pp. 164–181, 2011.

[108] K. Severson, P. Chaiwatanodom, and R. D. Braatz, "Perspectives on Process Monitoring of Industrial Systems," *IFAC-PapersOnLine*, vol. 48, no. 21, pp. 931–939, 2015.

[109] R. Gholami and N. Fakhari, "Support Vector Machine: Principles, Parameters, and Applications," in *Handbook of Neural Computation*, pp. 515–535, Elsevier, 2017.

[110] J. Zhou, D. Liu, Y. Peng, and X. Peng, "Dynamic Battery Remaining Useful Life Estimation: An On-line Data-Driven Approach," *I2MTC - International Instrumentation and Measurement Technology Conference, Proceedings*, pp. 2196–2199, 2012.

[111] B. Schölkopf and A. J. Smola, *Learning with Kernels: Support Vector Machines, Regularization, Optimization, and beyond.* MIT Press, 2002.

[112] C. Cortes and V. Vapnik, "Support-Vector Networks," *Machine Learning*, vol. 20, no. 3, pp. 273–297, 1995.

[113] L. Liao and F. Köttig, "Review of Hybrid Prognostics Approaches for Remaining Useful Life Prediction of Engineered Systems, and an Application to Battery Life Prediction," *IEEE Transactions on Reliability*, vol. 63, no. 1, pp. 191–207, 2014.

[114] J. Burns, A. Kassam, N. Sinha, L. Downie, L. Solnickova, B. Way, and J. Dahn, "Predicting and Extending the Lifetime of Li-Ion Batteries," *Journal of The Electrochemical Society*, vol. 160, no. 9, pp. A1451–A1456, 2013.

[115] E. Sarasketa-Zabala, F. Aguesse, I. Villarreal, L. Rodriguez-Martinez, C. M. López, and P. Kubiak, "Understanding Lithium Inventory Loss and Sudden Performance Fade in Cylindrical Cells during Cycling with Deep-Discharge Steps," *The Journal of Physical Chemistry C*, vol. 119, no. 2, pp. 896–906, 2014.

[116] M. Dubarry, C. Truchot, M. Cugnet, B. Y. Liaw, K. Gering, S. Sazhin, D. Jamison, and C. Michelbacher, "Evaluation of Commercial Lithium-Ion Cells based on Composite Positive Electrode for Plug-In Hybrid Electric Vehicle Applications. Part I: Initial Characterizations," *Journal of Power Sources*, vol. 196, no. 23, pp. 10328–10335, 2011.

[117] F. Röder, S. Sonntag, D. Schröder, and U. Krewer, "Simulating the Impact of Particle Size Distribution on the Performance of Graphite Electrodes in Lithium-Ion Batteries," *Energy Technology*, vol. 4, no. 12, pp. 1588–1597, 2016.

[118] T. P. Heins, N. Harms, L.-S. Schramm, and U. Schröder, "Development of a new Electrochemical Impedance Spectroscopy Approach for Monitoring the Solid Electrolyte Interphase Formation," *Energy Technology*, vol. 4, pp. 1509–1513, 2016.

[119] D. Abraham, J. Knuth, D. Dees, I. Bloom, and J. Christophersen, "Performance Degradation of High-Power Lithium-Ion Cells—Electrochemistry of Harvested Electrodes," *Journal of Power Sources*, vol. 170, no. 2, pp. 465–475, 2007.

[120] F. Yang, D. Wang, Y. Zhao, K. Tsui, and S. Joo, "A Study of the Relationship between Coulombic Efficiency and Capacity Degradation of Commercial Lithium-Ion Batteries," *Energy*, vol. 145, pp. 486–495, 2018.